AD-A035 057 TEXAS UNIV AT AUSTIN ELECTRONICS RESEARCH CENTER F/G 6/18
THE MEASUREMENT OF THRESHOLD TEMPERATURES IN THE OCULAR FUNDUS --ETC(U)
FEB 76 L A PRIEBE, A J WELCH F44620-71-C-0091
UNCLASSIFIED TR-180 AFOSR-TR-77-0005 NL

1 OF 3
AD
A035057

AFOSR - TR - 77 - 0008

ADA035057

The Measurement of Threshold Temperatures in the Ocular Fundus for Laser Induced Visible Lesions

by

L. A. Priebe and A. J. Welch

Department of Electrical Engineering

Technical Report No. 180

February 1, 1976

DDC
JAN 31 1977

BIO-MEDICAL ENGINEERING RESEARCH LABORATORY

ELECTRONICS RESEARCH CENTER
THE UNIVERSITY OF TEXAS AT AUSTIN
Austin, Texas 78712

DISTRIBUTION STATEMENT A
Approved for public release;
Distribution Unlimited

The Electronics Research Center of The University of Texas at Austin constitutes interdisciplinary laboratories in which graduate faculty members and graduate candidates from numerous academic disciplines conduct research.

Research conducted for this technical report was supported in part by the Department of Defense's JOINT SERVICES ELECTRONICS PROGRAM (U.S. Army, U.S. Navy, and the U.S. Air Force) through the Research Grant AFOSR F44620-72-C-0001. This program is monitored by the Department of Defense's JSEP Technical Advisory Committee consisting of representatives from the U.S. Army Electronics Command, U.S. Army Research Office, Office of Naval Research, and the U.S. Air Force Office of Scientific Research.

Additional support of specific projects by other Federal Agencies, Foundations, and The University of Texas at Austin is acknowledged in Sponsorship in the appropriate sections.

Reproduction, translation, publication, use and disposal in whole or in part by or for the United States Government is permitted.

Qualified requestors may obtain additional copies from the Defense Documentation Center, all others should apply to the Clearinghouse for Federal Scientific and Technical Information.

AIR FORCE OFFICE OF SCIENTIFIC RESEARCH (AFSC)
NOTICE OF TRANSMITTAL TO DDC
This technical report has been reviewed and is
approved for public release IAW AFR 190-12 (7b).
Distribution is unlimited.
A. D. BLOSE
Technical Information Officer

(18) AFOSR

UNCLASSIFIED
SECURITY CLASSIFICATION OF THIS PAGE (When Data Entered)

(19) **REPORT DOCUMENTATION PAGE**

READ INSTRUCTIONS BEFORE COMPLETING FORM

1. REPORT NUMBER: AFOSR - TR - 77 - 00054
2. GOVT ACCESSION NO.
3. RECIPIENT'S CATALOG NUMBER

4. TITLE (and Subtitle): (6) THE MEASUREMENT OF THRESHOLD TEMPERATURES IN THE OCULAR FUNDUS FOR LASER-INDUCED VISIBLE LESIONS,

5. TYPE OF REPORT & PERIOD COVERED: (9) INTERIM rept.,
6. PERFORMING ORG. REPORT NUMBER

7. AUTHOR(s): (10) L. A. Priebe, A. J. Welch (11) 1 Feb 76

8. CONTRACT OR GRANT NUMBER(s): Contract F44620-71-C-0091 (15)

9. PERFORMING ORGANIZATION NAME AND ADDRESS: Electronics Research Center, The University of Texas at Austin, Austin, Texas 78712 (12) 216p.

10. PROGRAM ELEMENT, PROJECT, TASK AREA & WORK UNIT NUMBERS: 4751-01 61102F 681306

11. CONTROLLING OFFICE NAME AND ADDRESS: AF Office of Scientific Research /NE, Bolling AFB DC 20332

12. REPORT DATE: February 1, 1976
13. NUMBER OF PAGES: 195

14. MONITORING AGENCY NAME & ADDRESS (if different from Controlling Office): (14) TR-180

15. SECURITY CLASS. (of this report): UNCLASSIFIED
15a. DECLASSIFICATION/DOWNGRADING SCHEDULE

16. DISTRIBUTION STATEMENT (of this Report)

Approved for public release; distribution unlimited.

17. DISTRIBUTION STATEMENT (of the abstract entered in Block 20, if different from Report): (16) 4751 (17) 01

18. SUPPLEMENTARY NOTES

19. KEY WORDS (Continue on reverse side if necessary and identify by block number)

Ocular Fundus
Laser-Induced Lesions
Temperature Variance Measurements

20. ABSTRACT (Continue on reverse side if necessary and identify by block number)

Measurements of temperature increases resulting from exposures to argon laser irradiations were made in the eyes of living rhesus monkeys with 10-20 μm diameter thermocouples. Using the appearance of an ophthalmoscopically visible lesion as the criterion for damage, the temperature associated with the appearance of a threshold lesion 5 minutes post exposure was determined. Temperature increases at the center of the lesion and at the (continued)

DD FORM 1 JAN 73 1473 EDITION OF 1 NOV 65 IS OBSOLETE

403789

UNCLASSIFIED
SECURITY CLASSIFICATION OF THIS PAGE (When Data Entered)

scans of the thermocouple through the laser image and from ophthalmoscopic measurements of the lesion radius.

Temperatures associated with threshold lesions were measured for a number of exposure durations and for image sizes from 100-200 μm (half-power diameter). Thresholds were acquired for both macular and paramacular (temporal) exposure sites. The average macular threshold temperature increases at beam center were 66.1°C, 29.4°C, 24.1°C, and 19.9°C for exposure durations of .01 second, .1 second, 1 second, and 10 seconds exposure durations.

The empirically determined threshold temperatures were compared to a finite differences model solution of the heat conduction equation. The threshold corneal power, measured retinal image profile and exposure duration were input to the model for threshold temperature prediction. The parameters of the model were adjusted to provide agreement between measured and calculated results.

THE MEASUREMENT OF THRESHOLD TEMPERATURES IN THE OCULAR FUNDUS FOR LASER INDUCED VISIBLE LESIONS*

by

L. A. Priebe and A. J. Welch
Department of Electrical Engineering

Technical Report No. 180
February 1, 1976

BIO-MEDICAL ENGINEERING RESEARCH LABORATORY

ELECTRONICS RESEARCH CENTER
THE UNIVERSITY OF TEXAS AT AUSTIN
Austin, Texas 78712

D D C
JAN 31 1977
RECEIVED

403769

*Research Sponsored by the Joint Services Electronics Program under Research Contract F44620-71-C-0091

Approved for public release; distribution unlimited

ABSTRACT

Measurements of temperature increases resulting from exposures to argon laser irradiations were made in the eyes of living rhesus monkeys with 10-20μm diameter thermocouples. Using the appearance of an ophthalmoscopically visible lesion as the criterion for damage, the temperature associated with the appearance of a threshold lesion 5 minutes post exposure was determined. Temperature increases at the center of the lesion and at the radial extent of the lesion were determined from radial scans of the thermocouple through the laser image and from ophthalmoscopic measurements of the lesion radius.

Temperatures associated with threshold lesions were measured for a number of exposure durations and for image sizes from 100-200μm (half-power diameter). Thresholds were acquired for both macular and paramacular (temporal) exposure sites. The average macular threshold temperature increases at beam center were 66.1°C, 29.4°C, 24.1°C and 19.9°C for exposure durations of .01 second, .1 second, 1 second, and 10 seconds, respectively. Average paramacular threshold temperature rises at the center of the lesion were 55.9°C, 39.9°C, 28.7°C and 24.8°C for .01 second, .1 second, 1 second, and 10 seconds exposure durations.

The empirically determined threshold temperatures were compared to a finite differences model solution of the heat

conduction equation. The threshold corneal power, measured retinal image profile and exposure duration were input to the model for threshold temperature prediction. The parameters of the model were adjusted to provide agreement between measured and calculated results.

ACCESSION for
NTIS White Section
DDC Buff Section
UNANNOUNCED
JUSTIFICATION
BY
DISTRIBUTION/AVAILABILITY CODES
Dist. AVAIL. and/or SPECIAL
A

TABLE OF CONTENTS

	Page
INTRODUCTION	1
BACKGROUND	3
Threshold Studies	3
Temperature Measurements	3
Temperature Models	14
Parameters in the Thermal Model	20
Measurement and Estimation of Absorption Parameters	22
Probe Measurement of Retinal Temperature	29
Rate Process Models	35
Significance	39
EXPERIMENTAL PROCEDURE	40
Surgical Procedure	40
Thermocouple Probe Fabrication	41
Instrumentation	42
Temperature Measurements	46
RESULTS	54
Temperature Rise Versus Corneal Power	55
Threshold Temperature Measurements	57
Thermal Model Parameters	63

	Page
Comparison of Experimental and Model Threshold Temperatures	77
Temperature-Time Histories	88
Horizontal Temperature Scans	105
Axial Temperature Scans	119
Comparison with Published Thresholds	127
Rate Process Model	133
Probe Response Measurements	139
DISCUSSION	144
Temperature Measurement	144
Threshold Determination	153
Lesion Size and Lesion Temperature Measurements	157
Model and Experimental Threshold Comparisons	160
Model and Experimental Scans	169
Model Parameters	173
Rate Process Model	178
CONCLUSIONS	180
REFERENCES	185

LIST OF FIGURES

Figure No.	Title	Page No.
1	Retinal Injury Threshold Energy Density versus Exposure Duration	5
2	Irradiance and Source Strengths for Lambert-Beers Absorption	18
3	Percent Absorption in an Absorbing Layer for Lambert-Beers Model	24
4	Model and Experimental Rise Times for Probes in Water, Air and Biomedium	33
5	Block Diagram of Recording System	43
6	Horizontal Scan of Probe Through Retinal Image	49
7	Laboratory Arrangement of Instruments	53
8	Experimental Temperature Rise versus Corneal Power	56
9	Experimental Average Temperature Increases for Macular and Paramacular Exposures	61
10	Model Calculated Temperature for Two Values of TOM	64
11	Calculated Temperature as a Function of Corneal Power	65
12	Absorption Profiles for Three Parameter Sets	68
13	Model Calculated Temperature Rise for Three Parameter Sets	70
14	Model Calculated Temperature Decoy for Three Parameter Sets	71

Figure No.	Title	Page No.
15	Model Calculated Temperature versus Radial Positions for Three Parameter Sets	72
16	Model Calculated Temperature as a Function of Axial Position for Three Parameter Sets	74
17	Calculate Temperature-time Histories for Various Image Radii and Absorption Parameters	76
18	Comparisons of Model and Experimental Threshold Temperatures in the Macula	86
19	Comparison of Model and Experimental Threshold Temperatures in the Paramacula	87
20	Average 10 second Temperature-Time Histories	89
21	Experimental and Model Temperature-Time Histories for Monkey 11-73	91
22	Experimental Temperature-Time History for Monkey 11-73 at the Center of the Retinal Image	92
23	Experimental Temperature-Time History for Monkey 11-73 at a Position 160μm Off-Center	93
24	Experimental and Model Temperature-Time Histories for Monkey 8-74	95
25	Experimental 0.1 second Temperature-Time History at 200μm for Monkey 8-74	96
26	Experimental 0.1 second Temperature-Time History at the Image Center for Monkey 8-74	97
27	Experimental 0.1 second Temperature-Time History at +200μm from Image Center for Monkey 8-74	98

Figure No.	Title	Page No.
28	Experimental Temperature-Time History for Monkey 4-74	100
29	Temperature versus Time for a .01 second Exposure 280μm in Front of the P.E.	102
30	Temperature versus Time at a Position 80μm in Front of the P.E. from Monkey 8-74	103
31	Temperature versus Time at a Position 10μm in Front of the P.E. from Monkey 8-74	104
32	Temperature versus Time in the P.E. from Monkey 8-74	106
33	Temperature versus Time 20μm Behind the P.E. from Monkey 8-74	107
34	Temperature versus Time 60μm Behind the P.E. from Monkey 8-74	108
35	Horizontal Model and Experimental Scan from Monkey 11-74	109
36	Experimental 0.1 second Horizontal Scan from Monkey 8-74	111
37	Experimental 0.01 second Horizontal Scan from Monkey 8-74	113
38	Experimental 0.01 second Scan from Monkey 8-74	114
39	Model and Experimental Horizontal Scan from Monkey 6-74	115
40	Experimental and Model Horizontal Scan from Monkey 4-74	117
41	Experimental and Model Scan for a 0.1 second Exposure from Monkey 10-74	118

Figure No.	Title	Page No.
42	Experimental Axial 0.01 second Scan from Monkey 8-74	120
43	Model and Experimental Axial Scan from Monkey 8-74	122
44	Direct Absorption of Light Eenrgy in the Thermocouple versus Axial Position for Three Experiments	123
45	Experimental Axial Scan for a .091 second Exposure from Monkey 6-74	125
46	Model and Experimental Axial Scan for Monkey 6-74	126
47	Comparison of Threshold Corneal Power Levels for Various Image Sizes for Macular Insertions	128
48	Comparison of Threshold Corneal Power Levels for Various Image Sizes for Paramacular Insertions	129
49	Comparison of Model Calculated Threshold Temperatures for the Data of Several Investigators	131
50	Retinal Power Density versus Time of Exposure	132
51	Paramacular Lesion Centers and Lesion Radius Threshold Temperatures Compared with Henriques Model Values	134
52	Macular Lesion Center and Lesion Radius Threshold Temperatures Compared with Henriques Model Values	136
53	Plot of ℓn (Exposure Duration) versus the Reciprocal of Temperature at the Lesion Center for Experimental and Model Values	138

Figure No.	Title	Page No.
54	Plot of ℓn (Exposure Duration) versus the Reciprocal of Temperature at the Lesion Radius for Experimental and Model Values	140
55	Resistance and Capacitance Analog for Thermocouple Probe	148

LIST OF TABLES

Number	Title	Page No.
I	Summary of Temperature Measurements in the Eye for Threshold Exposures	13
II	Values of Absorption Coefficients Calculated by Past Investigators	23
III	Power Reflection at Various Ocular Interfaces	26
IV	Relative Volumetric Specific Heats, Rise Times and Diffusivities for Several Media	32
V	Summary of Threshold Temperature Measurements	59
VI	Lesion Radius Measurement Normalized to One-Half Power Radius and Lesion Temperature Normalized to Center Temperature for Macular Exposures	62
VII	Absorption Parameters for Figure 12	67
VIII	Ten Second Threshold Data	78
IX	One Second Threshold Data	80
X	Threshold Data for .1 Second Exposures	81
XI	Threshold Data for .01 Second Exposures	83
XII	Threshold Data for Miscellaneous Exposures	84
XIII	Values Used to Derive Rate Process Coefficients	139
XIV	Frequency Response and Computed Rise Time for Three Probe Diameters in Air and Water Media	143
XV	Average Error due to Axial Averaging of Temperature for Two Probe Diameters	146
XVI	Comparison of Macular Experimental and Model Threshold Temperatures	175
XVII	Comparison of Paramacular Experimental and Model Threshold Temperatures	176

CHAPTER I

INTRODUCTION

Intense light sources such as Xenon lamps and lasers are used in a variety of applications. Industrial and medical applications include welding, cutting, ranging and photocoagulation of tissues. In any application of intense light sources, a major consideration is the safe use of the source in the particular application. The accidental overexposure of personnel must be prevented. The characteristics of the source and the mechanisms of interaction of intense light with biologic tissues are, therefore, very important.

The skin and the eye are most vulnerable to visible, ultraviolet and infrared sources. The ability of the eye to focus visible light to extremely small spot sizes makes the eye the most vulnerable biologic tissue. The unique structure of the retina and the fundus of the eye make these structures extremely sensitive to intense light energy since the pigmentation in the pigment epithelium (P.E.) and choroid absorbs a large amount of the light reaching these layers. Heat conduction from these layers damages the neural retina which has less ability for repair than skin.

Past studies of damage to the fundus of the eye from Xenon and laser radiation indicate that the major damage mechanism

is due to temperature increase in the tissue (1, 2, 3), especially for exposure durations longer than a few microseconds. For shorter duration exposures, different physical mechanisms such as acoustic transients and steam production may be important (1, 2, 3). For purposes of determination of safety standards for laser radiation and the extent damage in clinical uses of the intense light sources, the determination of temperature increase in the tissue for a given source and power level must be known.

In this research, the primary objective was to obtain measurements of the temperature field for various exposure durations with thin film copper-nickle thermocouples in the fundus of the eye. Threshold temperature increases and corneal powers for the appearance of ophthalmoscopically visible lesions just visible 5 minutes post exposure were determined for exposure durations shorter than 10 seconds and longer than a few milliseconds.

Additional objectives of this study were to compare the empirical threshold temperature to a heat conduction model solution and to compare the experimentally determined temperature required to produce damage with a simple rate process model.

In the following sections, the background pertaining to this research, methods, the results of threshold temperature measurements, a discussion of the results and conclusions resulting from this study are presented.

CHAPTER II

BACKGROUND

Threshold Studies

Several excellent reviews on threshold burn studies have appeared in the literature (1, 2, 3). This section will explain the factors in the study of threshold burns which are pertinent to this research.

Early investigations of damage to the eye as a result of exposure to laser sources were carried out by Zaret (4) and Ham et al. (5). Ham's experiments with ruby lasers and white light sources have been the basis for defining most of the "safe" levels currently in use. The criterion for damage was the appearance of an ophthalmoscopically visible lesion at times of 5 minutes and one hour post exposure. Vassiliadis et al. (6) at Stanford Research Institute found thresholds four times those reported by Ham et al. (5). Other investigators have found thresholds for various wavelengths and exposure durations which vary by more than an order of magnitude from the threshold values published by Ham and Vassiliadis (5, 6).

Most thresholds have been characterized by the power entering the pupil or by the retinal irradiance in W/cm^2 or J/cm^2, respectively. The data of Ham et al. (5) indicate that a higher power density is required to produce a threshold lesion for a 10μm image than for a 800μm image at long times of exposure.

For times of exposure below one millisecond the data indicate the same power density is required to produce a lesion for all image sizes for a given exposure duration.

In Figure 1 (3), a constant energy "density" ratio between thresholds determined by different investigators for image sizes of 100μm to 800μm is indicated. The data indicate a higher retinal dose (J/cm^2) for a smaller image than for a larger image for all times of exposure. If injury is a function of retinal temperature, one would expect a smaller image to cause a lower temperature increase for the same value of retinal irradiance than a larger image because of conduction effects.

Variations in thresholds determined by different investigators are due to several factors. The threshold values depend most upon the spectral and temporal characteristics of the source. In the visible to near infrared spectra, most of the light incident upon the cornea is transmitted to the retina (7, 8, 9, 10). In the far infrared spectrum, most of the energy is absorbed in the cornea. For example, Vassiliadis et al. (6) report a ratio of Neodymium (Nd) to ruby laser threshold energy of approximately five to one. The Neodymium wavelength (1.06μm) falls in a water absorption band in the near infrared. For this reason, more energy is absorbed in the preretinal ocular media than for wavelengths in the visible region.

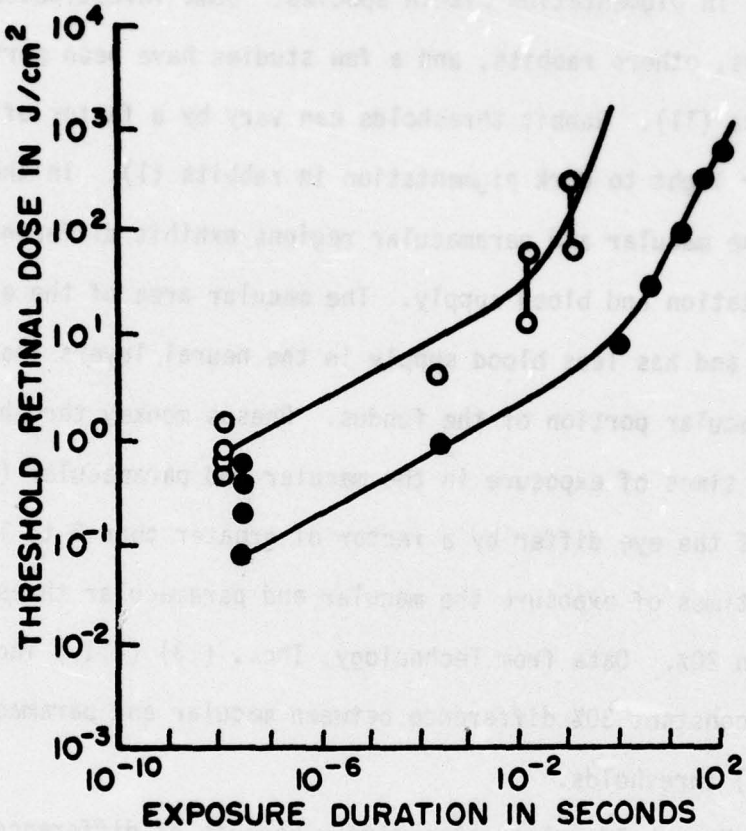

FIGURE 1: Retinal injury threshold energy density versus exposure duration. Upper curve is from Vassiliadis et al. (6) for 100μm images. Lower curve is from data of Ham et al. (5) for 800μm images.

Another factor which affects the threshold value is the variation in thresholds between experimental species and variations in pigmentation within species. Some investigators use monkeys, others rabbits, and a few studies have been performed with humans (11). Rabbit thresholds can vary by a factor of 4 to 1 for light to dark pigmentation in rabbits (1). In the monkey, the macular and paramacular regions exhibit differences in pigmentation and blood supply. The macular area of the eye is darker and has less blood supply in the neural layers than the paramacular portion of the fundus. Rhesus monkey thresholds for short times of exposure in the macular and paramacular (nasal) regions of the eye differ by a factor of greater than 2 to 1 (12). For long times of exposure the macular and paramacular thresholds are within 20%. Data from Technology, Inc., (13) (T.I.) indicate a nearly constant 30% difference between macular and paramacular (temporal) thresholds.

Threshold values also differ because of differences in lesion grading criteria between investigators. For times of observation of one hour or longer, the threshold for an ophthalmoscopically visible lesion decreases relative to the 5 minute observation. Davis and Mautner (14) report a value of 80% of the threshold determined for an immediately observable criterion for an observation time of 24 hours; the 10 minute observable lesion threshold was 90% of the value obtained for an immediately

observable lesion. At T.I. (13) a time of 5 to 7 hours post exposure has been found to be the minimum observation time required to define a minimal lesion. Gibbons (15) finds that the one hour and 24 hour thresholds are approximately equal for exposure durations shorter than 5 seconds. For a 5 second exposure, his experiments indicate a 5% decrease in the threshold corneal power required to produce a visible lesion. For 120 seconds exposure duration, the 24 hour threshold is 88% below the one hour threshold.

In addition to the experimental differences mentioned above, which give threshold variations of more than an order of magnitude, several physiologic factors may enter into the threshold determination. These factors include pupil diameter, body temperature, accommodation of the eye, blood pressure and level of anesthesia. The pupil diameter is important in the evaluation of hazards from diffuse reflections or large beams for which all the energy in the beam may not enter the eye. The level of accommodation of the eye determines the total focusing power of the ocular system and affects the minimal image size for both "near" and "far" field hazards. In the "far field" case the eye is relaxed (focused at infinity) and not accommodated at the laser as in the near field case. The far field case yields the minimal image size for laser exposure to the eye. The theoretical relation between retinal irradiance and source

radiance for an extended source is obtained using the Airy formula (16). The retinal irradiance I_r is given by the relationship:

$$I_r = \frac{\pi d_e^{\,2} RT}{4\ f^2}$$

where d_e is the pupil diameter in cm, R is the source radiance (W/cm^2 steradian), T is the transmission of the ocular media, and f is the focal length of the eye. The formula above is for viewing a diffuse specular reflection. The theoretical lower limit of the retinal image diameter for the Airy disc is given by:

$$d_r = \frac{2.44\lambda\ f}{d_e}$$

where d_e and f are defined as above and λ is the radiation wavelength in cm. From these considerations, the dark adapted (dialated pupil) viewing situation with the eye focused at infinity presents the "worst" case for viewing a laser source.

Most experiments have been performed under the worst case situations mentioned above. This undoubtedly results in a much lower threshold than in more realistic exposure situations which would occur in cases of accidental exposure. The subject may or may not be dark adapted as in the majority of laboratory

experiments. Also, in most experiments, the subject is anesthesized and the eyelid is held open. This reduces eye movements and eliminates the blink reflex. Long exposure durations could hardly, therefore, be expected to present a significant hazard to human subjects when the exposure is near the threshold value determined under the idealized situations mentioned above.

The role of body temperature in the determination of the ophthalmoscopically visible threshold has been reported by Ward and Bruce (17), and Polhamus and Welch (18). Ward and Bruce found an increase in retinal irradiance for a threshold lesion at a lower core temperature and a decrease in threshold irradiance for higher core temperatures. Ward and Bruce extrapolated their data to the rectal temperature axis on a plot of threshold irradiance versus rectal temperature and concluded that a fundus temperature increase of 6 to 7°C would be sufficient to cause damage.

Polhamus and Welch (18) measured the temperature rise required to produce a retinal lesion in the rabbit fundus directly with thermocouples. Their measurements of lesion temperature for a 10 second exposure in the rabbit fundus indicated that a temperature increase of 15.4^{o}C above the baseline temperature of 37°C was required to produce a minimum visible lesion.

They found that the rise in fundus temperature required to produce a visible lesion was approximately linear with pre-exposure fundus temperature over a range from 7°C below to 7.5°C above the normal 37°C baseline value.

The general physiological state of the animal and level of anesthesia can also affect the retinal irradiation threshold to indeterminate degrees. The condition of the retinal vasculature and blood pressure affect the flow of blood in the choriocapillaris. Geeraets and Ridgeway (19) found a lower threshold value for freshly killed rabbits than for live animals. Anesthetics such as sodium pentobarbitol which are commonly used in threshold experiments cause a partial decoupling of the animal's normal thermoregulatory mechanism and require external maintenance of the core temperature by heating pads or heat lamps.

Subthreshold changes have been observed histologically, histochemically, and in optic tract electrical activity. McNeer et al. (20) found that the ERG b-wave was reduced in amplitude for exposures at 50% of threshold if sufficient areas (approximately 44mm^2) of the retina were involved. Other investigators have noted an increase in the ERG for near threshold exposures and a change in the c-wave at 70% of the threshold exposure (21, 22). Hempel (22) noted changes in the LGN and cortical responses for near threshold values. Mautner (23) observed a decrease in

the visually evoked cortical potential at 25% of the ophthalmoscopically visible lesion threshold. Farrar (24) noted no decrease in visual acuity for subthreshold injury to trained monkeys but showed a transient decrease in acuity for superthreshold lesions.

In histological and histochemical studies, changes in the histology, enzyme inactivation and protein denaturation have been observed for subthreshold exposures to intense light sources. Using tissue electrophoresis, Geeraets et al. (25) demonstrated coagulation of retinal proteins at subthreshold energies. They also demonstrated a reduction in enzyme activity (DPN diaphorase) of enzymes which are important in the regeneration of retinal photopigments. DPN diaphorase, found mostly in the ellipsoids of the visual receptor cells, was inactivated as evidenced by loss of staining ability for exposure energies 10 to 15 percent below threshold.

Threshold powers for He-Ne and Ar sources for various image sizes and exposure times have been determined by various investigators. The data define several important variables which influence the response including experimental animal, image size, source wavelength and time of exposure. The monkey thresholds determined by Davis and Mautner (14) are higher than thresholds determined for the rabbit. The exposure power required to produce a threshold lesion increases with decreasing time of exposure.

The total power to produce a lesion increases with increasing image size but not in direct proportion to the area of the retinal image. As an example, He-Ne threshold power (1) for a monkey at 500 milliseconds exposure time increases by a factor of 1.67 for an increase in the ratio of the radii of 1.55. Since the exposure area increase is proportional to the square of the increase in the radius, the energy per unit area in the retinal image is less for a threshold lesion with a large retinal image than for a small image.

Temperature Measurements

Several investigators have attempted intraocular and retinal temperature measurements with thermocouples and thermistors (26-31). The data from these investigations are tabulated in Table I. Several experimental factors have caused the measurements to be questioned. The measurements were made with bulk wire thermocouples of relatively large size compared to the retinal image diameter. Some of the measurements were made during ruby laser and other short duration exposure sources. The thermocouples in at least one case (30) had a rise time of 40 milliseconds and were used to measure temperature rise for a 500μsecond exposure. No analytical models were employed to lend validity to the accuracy of experimental measurements.

TABLE I: Summary of Temperature Measurements in the Eye for Threshold Exposures

Group (Reference)	Placement of Sensor	Threshold Temperature Rise	Size of Thermocouple of Thermistor (Rise Time)	Image Diameter	Exposure Energy or Power	Source Characteristics
Najac, et al (26)	Lesion center behind P.E.	12.5-20.6°C	.1mm(*)	1.2mm	*	Zeiss 380-750mμ 380-1350mμ
Mellerio (27)	Near P.E.	23°C	.1mm(*)	.1 to .2mm	5mJ	400μsec. Ruby
Kohtiao et al. (28)	Anterior to P.E.	7.8°C σ = .7°C	.05mm(*)	.25mm	25mW @ 2.5 sec.	He-Ne, CW
Campbell, et al. (29)	Near P.E.	12-37°C	.25mm (40 m sec.)	1mm	65mJ	Ruby
Noryori, et al. (30)	Near P.E.	≈100°C in center of image	.25mm (40 m sec.)	1mm	65mJ	Ruby, 500μsec.
Crowder (31)	Mid-Vitreous	.82°C to 2.4°C	Thermistor bead (*)	*	*	*

* - Not Reported

Cain and Welch (32) developed a technique for temperature measurement in the rabbit fundus which enabled accurate measurements of temperature transients in the eye. They did not measure the temperature associated with lesion thresholds but they demonstrated the validity of this technique. The temperature probe consisted of a thin-film copper-nickel thermocouple on the tip of a quartz probe-type substrate. The thermal properties of the quartz substrate approximately matched the properties of the biomedium. The small volume of the metal films ($\approx$ .14% of mass of a 20μm probe with .2μm films of copper and nickel) with respect to the volume of the quartz substrate provided a sensor with the approximate thermal characteristics of quartz.

The conductivity of fused quartz is .0033 Cal/cm sec. ^{o}C versus .0015 for water. The densities of quartz and water are 2.29 and 1.0 gm/cm^3, respectively, and the volumetric specific heats are 0.4 and 1.0 Cal/gm^{o}C. The kρc product for quartz and water are .00131 Cal^2/cm^4 sec.$^{o}C^2$ and .0015 respectively (45). The approximate match of the properties of the sensor and the biomedium allows accurate transient temperature measurements for exposure durations longer than a few milliseconds.

Temperature Models

An evaluation of hazards to the eye presented by a variety of intense light sources requires an accurate thermal model

which accounts for spectral, temporal and spatial distributions of the source. The development of the model depends upon an accurate knowledge of the spectral dependence of the transmission and absorption of light in the various layers of the eye and the spatial distribution of the image in the eye. The transmission parameters will be discussed in a later section.

Several models have been developed which predict the transient and steady state temperatures in the eye (33-41). The models are based on solutions of the heat conduction equation:

$$\nabla^2 T + \frac{1}{k} A = \frac{1}{\alpha}\frac{\partial T}{\partial t}$$

where k = thermal conductivity (Cal/cm. sec.^{o}C)

$\alpha = \frac{k}{\rho c}$ = thermal diffusivity (cm^2/sec.)

ρc = volumetric specific heat (Cal/cm^3.^{o}C)

T = temperature rise (^{o}C)

A = heat source term (Cal/cm^3 sec.)

ρ = density (gm/cm^3)

c = specific heat (Cal/gm^{o}C)

The major differences among previously developed models are the assumptions of boundary conditions and absorption phenomena in the eye. Vos (33, 38) uses a square, uniformly irradiated image with uniform absorption in the depth and width of the irradiated volume. Clarke et al. (35) have developed a steady-

state model assuming exponential absorption. The heat generation function is:

$$A = A_o e^{-ax} \text{ for } 0 \leq x \leq C$$
$$0 \leq \theta \leq 2\pi$$
$$0 \leq r \leq b$$
$$= 0 \quad \text{elsewhere}$$

where A_o is the magnitude of the source term at $x = 0$, where C is the depth of the absorbing layer and b is the radius of the disk image. He assumes values of 314 cm^{-1} and 45 cm^{-1} for the P.E. and choroid absorption coefficients (a) in his cylindrically symmetric two layer model. Calculations performed with this model indicate a temperature rise of 10°C for a threshold lesion using data of Ham et al. (5) and about 23°C for a threshold lesion from the data of Allen et al. (42) for a white light source.

Other steady-state models proposed by Hansen et al. (34) and Peacock (43) are of questionable value because they do not account for the structure of the retina. They assume 100% absorption of the input light in a small thickness of the retina.

Presently the most comprehensive model available is a finite difference solution to the heat conduction equation developed by Mainster, White and Tips (39, 40, 41). The model includes the effects of temporally, spectrally, and spatially varying source terms, assumes two layer absorption in the P.E.

and choroid, and allows different conductivities and volumetric specific heats to be assigned to the various media of the eye. The model calculates temperature as a function of position and time throughout the fundus for a circularly symmetric retinal image.

The irradiance (H) in the P.E. and choroid for a uniform image is illustrated in Figure 2. The source strength (A) is also shown in the figure. Lambert-Beers (34) absorption is assumed and the retinal irradiance has the form,

$$H_1 = h(r)\, H_0 \exp[-a_1 z] \qquad \text{(P.E.)}$$

$$H_2 = h(r)\, H_0 \exp(d_1\, a_2 - d_1\, a_1 - d_2\, z) \qquad \text{(Choroid)}$$

$$d_1 < Z \leq d_1 + d_2 \quad \text{where}$$

h(r) is the normalized irradiance profile at the retina and d_1 and d_2 are the depths of the P.E. and choroid respectively.

The source strength in each layer is related to the irradiance by the relationship:

$$A_i = \frac{-\partial H_i}{\partial z} \qquad i = 1, 2.$$

The various layers are assumed to be homogeneous and isotropic with constant absorption parameters and thermal parameters k, ρ, and c. The retinal image distribution may be entered directly into the program or calculated using the point spread function.

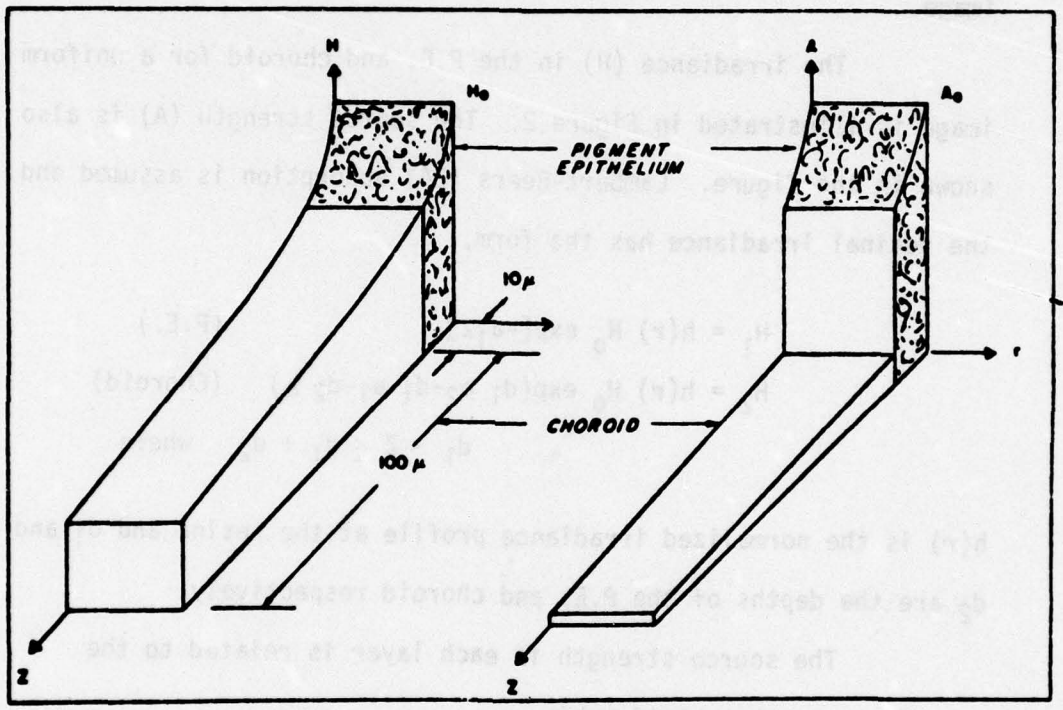

FIGURE 2: Irradiance and heating source strengths for exponential absorption with a constant radial energy distribution.

Cain and Welch (32) used this model to compare calculated and measured temperatures. Measured retinal distributions were used in the model rather than calculated source characteristics and the point spread function of the eye. Measurements indicated that the model predicted temperatures were generally 30% low for images greater than 10 times the size of the thermocouple at exposure times greater than one second.

The possible reasons for the differences between calculated and measured temperatures were:

1) assumed values of thermal parameters k, ρ, and c.
2) assumed values for the transmittance of the pre-retinal ocular media and the absorption parameters for the P.E. and choroid.
3) measurement error due to direct absorption in the thermocouple.
4) errors in the measurement of the beam profile at the retina.
5) errors in measurement of incident corneal power.
6) size of the probe relative to the size of the image.
7) measurement of retinal image diameter.

Of the probable sources of error, Cain and Welch (32) demonstrated that the above points 3 through 6 had little effect upon the measurements. The substitution of k = .0013 (brain tissue) versus k = .0015 Cal/cm-sec^{o}C (water) increased the calculated

temperature for exposure times which resulted in near steady state temperature increases.

Parameters in the Thermal Model

The model for retinal temperature rise which results from exposure of the ocular fundus to intense light sources requires the determination of thermal conductivities, volumetric specific heats and light absorption in the various layers of the eye. Generally, the values for conductivity (k) and volumetric specific heat (ρc) are taken to be the same as for water in each layer in the model. Only the absorption of light in the different layers of the eye is variable. However, a major source of error in the calculation of temperature for long exposures is the value assumed for conductivity and the volume of tissue heated which is related to the absorption coefficients of the layers within the retina. For short duration exposures and for tissue rise time calculations, the volumetric specific heat, the absorption coefficients and the measurement of retinal irradiance affect the model solutions.

The conductivity value for water is 1.5×10^{-3} cal cm^{-1} sec^{-1} $^{o}C^{-1}$ for human blood 1.21×10^{-3} cal $cm^{-1}sec^{-1}$ $^{o}C^{-1}$ and for rat blood 1.26×10^{-3} cal cm^{-1} sec^{-1} $^{o}C^{-1}$ (44). From the conduction equation at steady state:

$$\nabla^2 T = -\frac{1}{k} A$$

which indicates that the steady state temperature is inversely proportional to the conductivity and directly proportional to the volume of tissue heated by the source term A. From the values of conductivity given above, the values for blood would imply a higher steady state temperature than the value for water.

The source term (A) includes an absorption coefficient a and is given by:

$$A_{PE} = h(r)\, H_0 a_1 \exp[-a_1 z] \quad 0 < z < d_1$$

in the P.E. where d_1 equals the depth of the P.E. and $_1$ equals the absorption coefficient of the P.E.

For the choroid, the source term is given by:

$$A_{ch} = h(r)\, H_0 a_2 \exp[d_1 a_2 - d_1 a_1 - a_2 z]$$
$$d_1 < z < d_2 + d_1$$

where a_1 and d_2 are the absorption coefficient and depth of the choroid respectively. The volume of tissue heated enters into the effective rise time of the temperature-time history at a point in the tissue and into the final temperature at that point.

For very short times for which no significant conduction has taken place, the conduction equation is given by:

$$\frac{\partial T}{\partial t} = \frac{1}{\rho c} A$$

and the temperature is approximately:

$$T \approx \frac{a_1 H_0}{\rho c} t, \qquad \text{at } z = 0 \text{ and } r = 0.$$

So, at short times, the slope of the temperature versus time is proportional to aH_0 and inversely proportional to ρc. These simplifying assumptions show the importance of the absorption coefficients in the calculation of the temperature versus time profiles in the tissue.

Measurement and Estimation of Absorption Parameters

The absorption and transmission of the various media within the eye have been measured by several different investigators. The measurements of Geeraets et al. (7, 8) and Boettner and Wolter (9) are the most frequently referenced values in the literature. The measurements of absorption and transmission have been accomplished in vitro on excised human, primate and rabbit eyes. Calculations of absorption parameters for the assumption of Lambert-Beers absorption have been made by several different investigators. A summary of past calculations is presented in Table II. Since few separate measurements for the pigment epitheluim and choroid exist in the literature, the general assumption has been made that 50% of the light reaching

the P.E. is absorbed in that layer. Generally, the absorption coefficients of Table II do not follow this assumption as illustrated in Figure 3.

In Figure 3 is illustrated a plot of the percent absorption versus az for the assumption of Lambert-Beers absorption in the tissue. For a 50% absorption of light in the 10μm thickness of the P.E., az is .69 this implies that a, the absorption coefficient for the P.E., is 690 cm^{-1} or less. In Table II, three of the four tabulated values exceed this value. In fact, for the value of 2080 cm^{-1} for a in the P.E., 88% of the light incident on this layer is absorbed.

TABLE II: Values of Absorption Coefficients Calculated by Past Investigators.

Reference	Animal	TOM	APE	ACH	Sclera
White (45)	Monkey	.79	2080	208	.044
MCV (by White) (45)	Rabbit	.82	832	83.2	.770
Boettner (Brooks AFB) (44)	Monkey	.51	1622	189	
Tom White (45)	Rabbit	.636	637.6	76.28	

TOM = The transmission of the preretinal ocular media.

APE = The absorption coefficient of the P.E.

ACH = The absorption coefficient of the choroid.

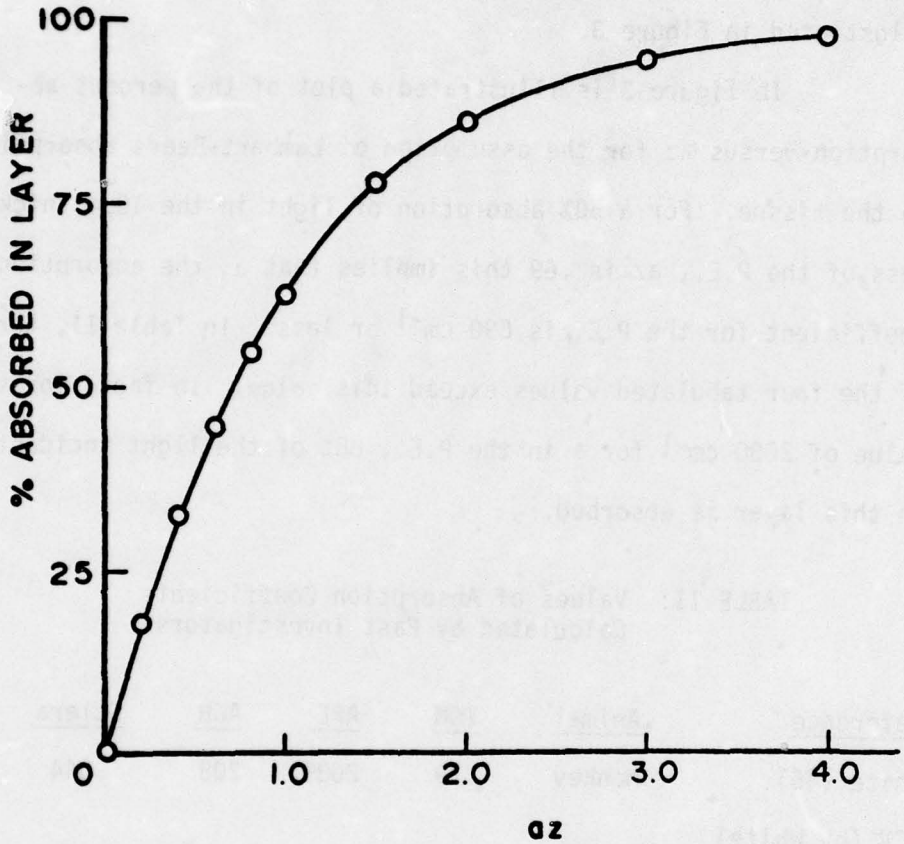

FIGURE 3: Percent absorption in an absorbing layer for Lambert-Beers model. The percent of light reaching the front of the layer which is absorbed in that layer is plotted versus the absorption coefficient (a) times the tissue depth (z).

It is also apparent that large discrepancies in the transmission of the preretinal ocular media exist in the literature from the values of TOM given in the table. The transmission of the preretinal ocular media includes absorption in the tissues and fluids anterior to the P.E. and reflection from boundaries of different refractive index. Major differences in the values determined for TOM exist between the measurements of Geeraets and Berry (7, 8) and Boettner (9). Geeraets and Berry measured both directly transmitted light and scattered light while Boettner attempted to separate the direct and scattered components of light. Boettner's assumption was that light within a 1° cone at the exit from the tissue being measured was directly transmitted and the light outside this cone was scattered light. The difference in the two sets of measurements is approximately 30%.

As light impinges upon the eye, it encounters first an air-water interface. A portion of the light is reflected due to the different indices of refraction according to the relationship:

$$R = \frac{(n_1 - n_2)^2}{(n_1 + n_2)^2}$$

where n_1 and n_2 are the refractive indices of the two media and R is the fraction of incident power reflected (47). This relation holds only for multiple surfaces between media which are separated by distances greater than a wavelength. For very thin films such

as water on the cornea, the actual reflection may differ markedly from this value due to interference effects. Also, the use of a contact lens presents a higher index than water to the incoming light. Contact lenses are frequently used in experiments to prevent corneal drying. From the formula above, the reflection of light from the various surfaces of the eye may be calculated. A summary of these effects is presented in Table III.

TABLE III: Power Reflection at Various Ocular Interfaces for $\lambda = 5000\text{Å}$

Material or Ocular Medium	Index of Refraction of Medium (48)	Index Anterior to Medium	% Reflection
Glass (contact lens)	1.5	1.00 (air)	4.0
Cornea (contact lens)	1.37	1.5 (contact)	.2
Cornea (air)	1.37	1.00 (air)	2.44
Aqueous humor	1.336	1.37	.02
Crystaline lens	1.4	1.336	.06
Vitreous humor	1.336	1.4	.06
Neural retina	--	1.336	3.0
TOTAL REFLECTIONS (with contact)			7.34
(no contact lens)			5.58

The reflection of the neural retina is from Boettner (9) at 5000Å wavelength. For a contact lens on the cornea, approximately 7.3% of the incident light is reflected at the various surfaces of the eye. With no contact lens, approximately 5.6% is reflected. Assuming an absorption coefficient of an equal length of water for the preretinal ocular media ($a \approx .05\ cm^{-1}$ (35)), the fraction of corneal light reaching the pigment epithelium is given by,

$$TOM = 1 - \%\ Reflected - e^{-az}$$

where z is approximately 1.8 cm for the monkey eye. Therefore, TOM is approximately 83-85%.

As shown in Table II, all measured values are lower than the calculated values. One reason is that the eye is not a homogeneous medium and cannot be approximated accurately by an equivalent length of water. Some light is scattered out of the image due to inhomogeneities in the ocular media and nonlinear optical distortions in the optical system.

A comparison of the results presented in Table II, however, show striking differences in transmission values for the monkey determined by two groups of investigators. The value obtained by Boettner for direct transmission is much lower than the value from Geeraets and Berry. Boettner also obtained a total transmission figure of 65-70% for the monkey (9). From the above comparisons, it can be seen that

even one of the seemingly simpler measurements yields large differences between investigators. The measurement of TOM is a critical parameter in the model for retinal temperature rise since the magnitude of the source term vaires directly with changes in TOM. Since the model is a linear equation, the temperature varies linearly with changes in the value for preretinal ocular media transmission.

The absorption parameters in Table II also appear to be essentially unknown. There are few measurements of the P.E. and choroid separately, but those measurements indicate a nearly 50-50 split for rabbits and humans in the absorption of light in the P.E. and choroid (7, 8). From Figure 3, it is apparent that the absorption coefficients listed in the table are too high for the P.E. since a 10μm thickness even for a = 1622 cm^{-1} results in 80% of the light being absorbed in the P.E. From Geeraets and Berry's (7, 8) measurements, approximately 11% of the light at 4880Å is transmitted through the P.E. and choroid. With a 50% absorption of this light in each layer, 44.5% of the light reaching the P.E. is absorbed in the P.E. and 80.2% of the light reaching the choroid is absorbed in the choroid. From Figure 3, az is approximately .60 for the P.E. and which results in absorption coefficients of 600 cm^{-1} and 162 cm^{-1} for the P.E. and choroid, respectively. The 50% split of absorbed radiation is somewhat arbitrary and the choice of TOM is also open to question. The total transmission values may be

too high and the direct transmission values are almost certainly too low. The choice of TOM is therefore in the range from 51 to 80 percent for the monkey eye. A choice of 65 percent transmission should therefore be within ± 23% of the correct answer for the transmission of the preretinal ocular media and is in close agreement with the total transmission value of Boettner (9). The change in TOM directly affects the calculations of retinal temperature; a 20% change in TOM causes a 20% change in the calculated temperature increase.

Probe Measurement of Retinal Temperature

The invasive measurement of tissue temperature with a probe-type thermocouple requires a reasonable model for the perturbation of the measurement by the sensor. The probe presents several problems in temperature measurement some of which may be accounted for in analysis, others which can only be estimated. In order to make accurate temperature versus time measurements, the rise time of the probe-tissue system must be tissue limited. This implies that the probe step response in the medium must be faster than the rise time of the medium for the measurement conditions. A common method used to characterize the ability of a thermocouple sensor to measure dynamic temperature changes is the idealized step response. This response is not only a probe characteristic

but it also depends upon the medium in which the probe is imbedded as will be demonstrated later.

The thermal resistance of the probe to axial conduction down its leads and the thermal resistance from the probe to the tissue are also very important properties of the probe-tissue system. If the axial conduction resistance is lower than or low enough with respect to the probe to tissue interface resistance, the probe may measure temperatures which are significantly lower than the temperature of the medium. For small cross-sectional lead areas this conduction resistance can be maximized in a real system.

In the case of the measurements for this research, the direct absorption by the probe of incident radiation must be small compared to the absorption in tissue. The differential absorption of radiant energy by the probe and tissue gives rise to a direct absorption component of temperature rise which tends to make the probe indicate a temperature which is higher than the temperature of the surrounding tissue. Since the rise time of the direct absorption component is much faster than convection from tissue, the measured rise time may be separated into two components.

The rise time or time to nearly steady-state temperature depends upon the volume of tissue heated. A smaller volume will reach steady-state faster than a larger volume. For the reasons stated above, the volume of tissue heated should be much larger than the volume occupied by the probe. Since the tissue in this

research is heated by a radiant light source, the shadowing by the probe will remove less than one percent of the source term if the radius of the image is 10 times that radius of the probe. Axial conduction down the probe will also be minimized for larger images.

The characteristics of the probe to a step increase in temperature have been discussed by Reed (49) and Cain and Welch (32). Reed calculated the rise time of a cylinder in an infinite medium for various simplifying assumptions. First, the probe was entirely embedded in the medium with no axial flow. Second, the heat transfer between the probe and medium was by conduction. The problem which Reed solved was for a probe initially at unit temperature and at time t = 0 it was placed in an infinite medium at zero temperature. This solution can also be found in Carslaw and Jaeger (50). The calculated fall time (cooling time) is equivalent to heating a probe in a medium at elevated temperature.

Reed numerically evaluated the solution from Carslaw and Jaeger (50) and obtained plots of non-dimensional rise time τ versus relative volumetric specific heats. The results of his analysis are tabulated for a few materials of interest to this research in Table IV. The dimensionless rise time is given by:

$$\tau = \frac{\alpha t}{\ell_c^{\,2}}$$

where;

$\alpha = k/\rho c$ = thermal diffusivity,

ℓ_c = radius of the thermocouple probe,

and, t = real time.

For the case of a probe in an infinite medium, the diffusivity is the diffusivity of the medium. The relative volumetric specific heat used in the determination of rise time is:

$$\overset{*}{\nu} = \frac{\rho c \text{ medium}}{\rho c \text{ probe}}$$

where ρc of the probe is assumed to be the value for quartz.

TABLE IV: Relative Volumetric Specific Heats, Rise Times and Diffusivities for Several Media, from Reed (49)

Medium	$\overset{*}{\nu}$	$\tau_{10-90\%}$	α (cm^2/sec)
Water	2.43	.47	1.44×10^{-3}
Air	8.8×10^{-4}	6×10^{2}	.187
Biomedium (skin)(45)	2.22	.64	7.4×10^{-4}

In Figure 4 is illustrated the rise time (10-90%) response of quartz cylinders embedded in the media listed in Table IV. Experimental points from Cain and Welch (32) are also illustrated in the Figure. The measurements were made by Cain by driving thermocouples into a

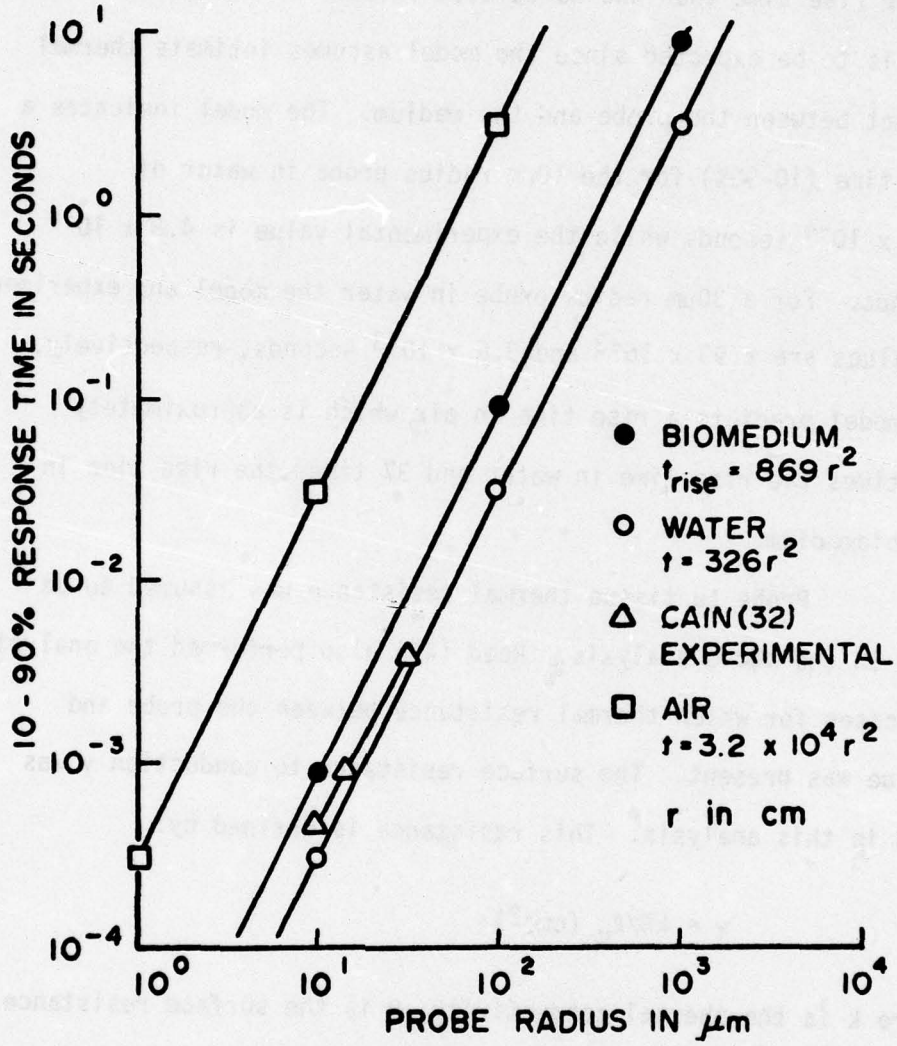

FIGURE 4: Model and experimental rise times for probes in water, air and biomedium. The calculated values are from the model by Reed (49). The experimental values are from Cain (62).

heated water bath. The measured values indicate a slightly longer rise time than the calculated values for all probe sizes. This is to be expected since the model assumes intimate thermal contact between the probe and the medium. The model indicates a rise time (10-90%) for the 10μm radius probe in water of 3.26×10^{-4} seconds while the experimental value is 4.8×10^{-4} seconds. For a 30μm radius probe in water the model and experimental values are 2.93×10^{-3} and 3.6×10^{-3} seconds, respectively. The model predicts a rise time in air which is approximately 100 times the rise time in water and 37 times the rise time in the biomedium.

Probe to tissue thermal resistance was assumed to be zero in the above analysis. Reed (49) also performed the analysis for cases for which thermal resistance between the probe and tissue was present. The surface resistance to conduction γ was used in this analysis. This resistance is defined by:

$$\gamma = kR/\ell_c \ (cm^{-2})$$

where k is the thermal conductivity, R is the surface resistance per unit of surface area of the sensor and ℓ_c is a characteristic dimension of the sensor (diameter or length). For a "typical" value of a less than ideal thermal interface ($\gamma = 4$), the response time increases by a factor of 4.4 for quartz in a biomedium and 1.8 for quartz in air. Thus, for a realistic situation, the

response time of the model for quartz in a biomedium for a 10μm radius probe is 3.8 milliseconds. One would expect from Reed's analysis and Cain's measurements that for times greater than 10 milliseconds, the probe response is essentially complete and the perturbation of temperature measurement due to probe transient response is negligible.

Rate Process Models

The biological damage which results from elevated temperature in tissue has been modeled by several investigators. Henriques (51) was the first to apply a rate process model to thermal damage to a biological tissue, porcine epidermis. Fugitt (52) and Stoll (53, 54, 55) modified the model with empirically derived rate constants. Hu and Barnes (56), Kach (57), and Vassiliadis (58) calculated a damage integral as a function of temperature profile in tissue.

All of the models developed have been based on the Arrhenius equation:

$$\frac{d}{dT}(\ln k') = \frac{Eo}{RT2} \quad , \text{ or}$$

$$k' = A\, e^{-E_o/RT}$$

which states that the reaction rate increases exponentially with temperature. In the equation, k' is the reaction rate constant,

A is a pre-exponential or frequency factor, E_0 is the experimentally derived activation energy, T is the absolute temperature (^oK) and R is the gas constant. The reaction velocity constant may be written as a function of a change in free energy, ΔF where:

$$\Delta F = \Delta H - T \Delta S$$

in which ΔH is the barrier heat energy and ΔS is the barrier entropy. In the equation for ΔF, the temperature change ΔT is assumed to be zero. The reaction rate constant thus becomes:

$$k' = \frac{kT}{h} e^{-\Delta F/RT} = \frac{kT}{h} e^{\Delta S/R} e^{-\Delta H/RT}$$

where k = Boltzmann's constant, and h = Planck's constant. The derivative of ln k' with respect to T is:

$$\frac{d}{dT} (\ln k') = \frac{\Delta H + RT}{RT^2}$$

which is identical to the Arrhenius equation with $E_0 = \Delta H + RT$.

The reaction kinetics for a first-order reaction give for the change in concentration with respect to time:

$$\frac{dc}{dt} = k'c$$

where c is the concentration. The fraction of remaining molecules at time t, is given by,

$$\frac{c}{c_o} = e^{-\int_o^t k' \, dt}$$

The surviving fraction is therefore dependent upon the barrier heat energy of the reaction, the temperature and the length of time at an elevated temperature.

The term:

$$\frac{kT}{h} e^{+\Delta S/R}$$

is assumed to be constant with temperature, even though it does vary slightly. This assumption is not too bad since ΔS is relatively insensitive to temperature and for typical proteins $\Delta S/R$ is $\approx$ 30 to 250 (55).

If k' is relatively independent of temperature, a plot of $\ln S$ versus time yields a line with slope -k', since

$$\ln (c/c_o) = -k' t$$

is of the form y = mx + b. Plotting ΔF versus T allows determination of ΔH and ΔS since:

$$\Delta F = -RT \ln \left(\frac{k'}{kT/h}\right)$$

and,

$$\Delta F = \Delta H - T \Delta S$$

if the variation of k' with temperature is known. Thus, the various constants can be determined from a plot of experimentally determined data.

The applications of a rate process models to biological tissues have been based on rather arbitrary criteria. No quantitative assays of protein or enzyme deactivation associated with threshold burns have been made. Generally, two criteria are assumed, the first is complete cellular necrosis associated with a "damage" integral (51, 52):

$$\Omega = \int_0^t A e^{-E/RT} dt$$

where $\Omega = 1$ at threshold.

The second commonly used criterion is for S, the surviving fraction equal to e^{-1} which corresponds to:

$$c = c_{o/e} = .368\ c_o.$$

Typical values of the rate constants temperatures and activation energies and barrier entropies for denaturation of proteins and enzyme inactivation have been documented by Wood (59). The value for ΔH is between 35,600 and 198,000 for the enzymes and proteins. The temperatures of denaturation and inactivation vary from 25°C to 120°C.

Significance

Many questions must be answered if a comprehensive theory of retinal injury is to be developed. Ideally, a single model could be used to predict injury to ocular tissues for a variety of exposure conditions including wavelength, pulse width, pulse repetition frequency and image geometry. This may not be a practical goal with respect to a simple thermal model, but may need to include the short and long-term effects mentioned earlier. The thermal model may be of some practical use, however, when coupled with a rate process model over a limited range of exposure conditions (say 100μm seconds to 10 seconds). It may be of use in clinical applications for the prediction of the extent of damage in retinal diathermy. Also, the development of safety standards could be aided by the thermal model coupled with actual temperature measurements in the retina or other ocular tissues.

CHAPTER III

EXPERIMENTAL PROCEDURE

Surgical Procedure

A surgical procedure has been developed which exposes the backside of the eye of anesthesized monkeys (60). Nembutal is injected through a catheter inserted in a large saphenous vein to keep the animal sedated throughout the surgery and the experiment. Earbars mounted on a platform secure the animal's head.

A midline incision in the scalp is made from the supra-orbital margin of the frontal bone extending to approximately 3 cm beyond the junction of the frontal and parietal bones. Two incisions in the skin are made approximately perpendicular to the midline incision. One along the supra-orbital margin from the midline to the zygomatico-temporal foramen. The other incision extends from the midline incision to the back of the ear. The fascia of the temporal muscle is cut along the superior temporal line and the temporal muscle is elevated and reflected away from the skull to expose the posterior portion of the bony orbit. A dental drill is used to remove bone to expose the back of the eye in an area between the anterior and posterior ethmoidal foramena. The peri-orbital fat and a portion of the lacrimal gland are then removed and the sclera is cleared of all fascia for probe insertion. The insertion area for the probe is generally within 1-2 millimeters of the macula or in the macula.

Three sutures are placed in the conjuctiva to bind the eye to an eyeholder (a ring connected to an adjustable arm mounted on the animal platform) which prevents eye movement during temperature measurements. The eyeholder is adjusted to the correct height and position, and a contact lens is mounted on the cornea to prevent drying of the cornea.

The animal platform is positioned with a five degree of freedom animal holder to provide a clear view of the retina through a fundus camera. A point as near as possible to the macula is chosen as the site of probe insertion. This point is positioned in the crosshairs of the fundus camera, and a low intensity Argon C.W. laser beam (4880Å) is directed to it. The size and intensity of the laser image at the retina is controlled with lenses and neutral density filters. The resulting laser image can be observed through the sclera and serves as a marker for insertion of the probe. Low laser energies are used during probe insertion to prevent thermal damage to the fundus.

Thermocouple Probe Fabrication

The thermocouple probes used in this study were developed in the Engineering Mechanics Laboratory at the University of Texas by Professor E.A. Ripperger and Mr. W.D. Martins. The probes were manufactured for this study by W.D. Martins. The probe fabrication procedure and characteristics of the probe have been described

elsewhere (61, 62). Only a brief description of the probe geometry and characteristics will be presented in this section.

The thermocouple probe is a copper nickel junction vacuum deposited on a quartz substrate. The quartz substrate is drawn to a tip diameter of 10-20μm from a millimeter quartz rod. After the substrate is cleaned, the nickel lead is attached to the deposited film. The tip of the probe is masked and an insulating material is deposited on the probe and lead with the exception of the probe tip. A copper film is then deposited over the probe and tip, forming a junction only at the tip of the probe. A copper lead is attached to the film and a final coat of insulator is deposited over the entire probe, including the tip, to prevent interaction of the metal junction with body fluids.

The copper nickel thermocouple junction provides an EMF (electromotive force) of 18-21μV per degree celsius. The probes are linear in response to water bath temperatures over the range from $0^{o}C$ to $100^{o}C$. Typical rise times (10-90%) of a 10μm probe in a water bath are less than 1 millisecond. The probe on the quartz substrate is mechanically strong enough to allow insertion into soft tissue media without breaking.

Instrumentation

A block diagram of the experimental equipment is illustrated in Figure 5. The thermocouple probe is attached to a

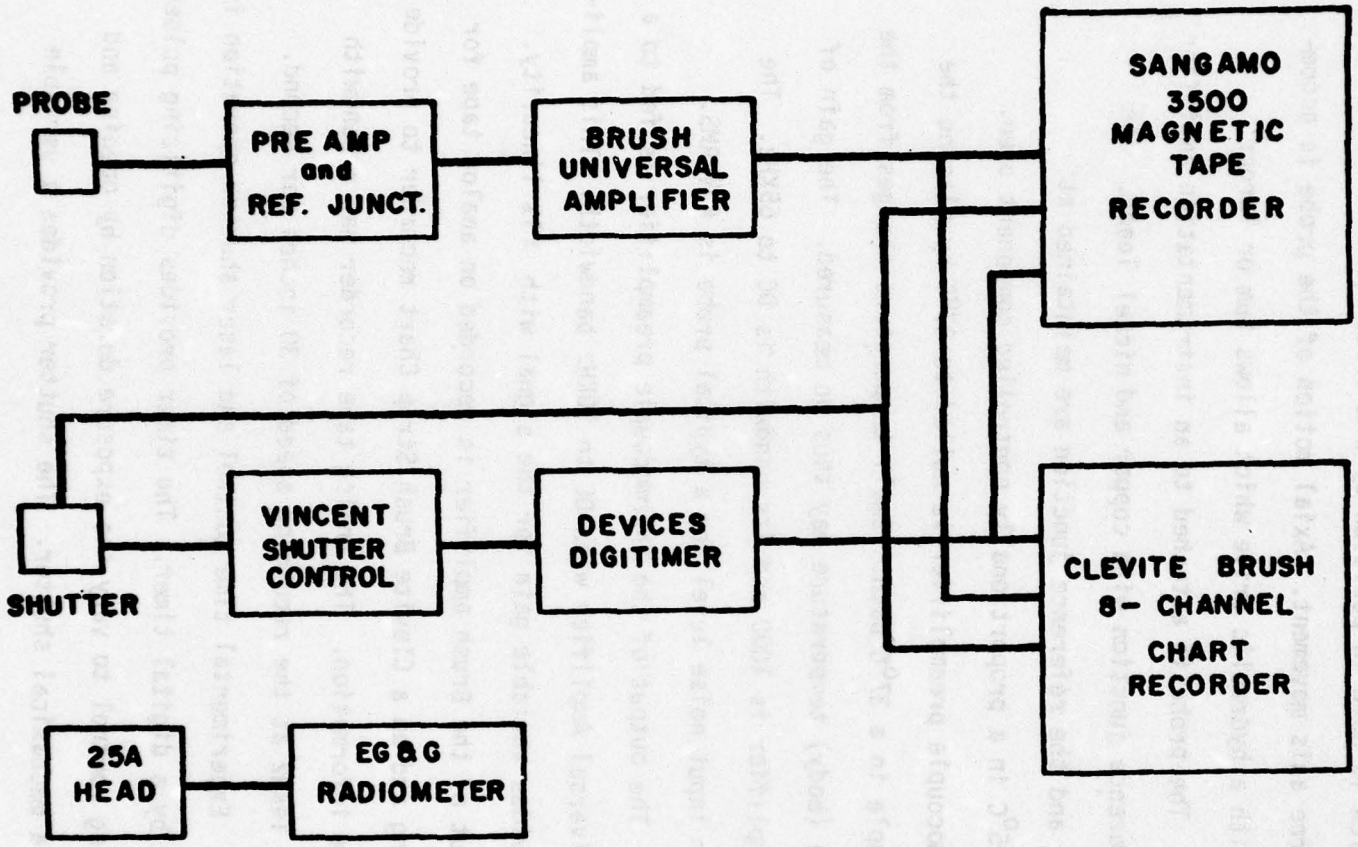

FIGURE 5: Block diagram of recording system.

holder which is held in position by a micromanipulator which allows three axis movement. Axial motion of the probe is accomplished with a hydraulic drive which allows 2μm or larger movement. The probe is attached to an instrumentation amplifier and a reference junction with copper and nickel leads. The amplifier and the reference junction are maintained at $37^{o}C \pm .05^{o}C$ in a proportionally controlled component oven. The thermocouple preamplifier is nulled to $37^{o}C$ by placing the thermocouple in a $37^{o}C$ bath. Small temperature changes from the reference (body) temperature may thus be measured. The gain of the preamplifier is 1000 and its bandwith is DC to 65KHz. The amplifier input noise level for a typical probe is 4μV RMS.

The output of the thermocouple preamplifier is fed to a Brush Universal Amplifier with DC to 10KHz bandwidth. This amplifier provides variable gain for the signal with ±1% linearity. The output of the Brush amplifier is recorded on analog tape for digitizing and on a Clevite Brush Strip Chart recorder to provide real time information. The analog tape recorder has a bandwith of DC to 14KHz at the recording speed of 30 inches per second.

Experimental time control and laser shutter operation is provided by a digital timer. The timer provides digitizing pulses and timing control to vary the exposure duration by opening and closing a mechanical shutter. The shutter provides a variable

duration exposure with approximately .2 millisecond opening time. Digitizing pulses and shutter pulses are recorded on the analog tape with the temperature information for later data reduction.

An EG&G Radiometer is used to monitor the laser power for each exposure. The radiometer is calibrated by an NBS traceable thermopile with an accuracy of ±5%. A light pulse signal from the radiometer is recorded for timing reference on the analog tape.

A parallel real time monitor of the temperature rise is provided with a 1 MHz bandwith oscilloscope. Since the chart recorder bandwidth is limited to 90Hz, accurate real time determination of the direct absorption of the thermocouple may be accomplished by the scope monitor and polaroid photographs. The scope provides a real time feedback for positioning the probe in the peak of the temperature profile.

Visual observation of lesion formation is accomplished with a fundus camera mounted on the experimental table. A reticle in the fundus camera eyepiece is calibrated to allow visual measurement of the lesion size. The appearance of a lesion five minutes post exposure is the criterion for threshold. Fundus photographs of lesions and probe insertion sites may also be taken with the aid of the fundus camera.

Temperature Measurements

A micro-thermocouple probe (32) is inserted into the sclera by the use of an ultrasonic dentral drill. A hole is first drilled in the sclera with a sharply pointed tungsten probe (1-3μm tip diameter). Then a long focal length microscope mounted above the animal is used to locate the hole for the insertion of the 10 to 20μm temperature probes. After insertion of the probe, its depth is adjusted by observing the position of the probe tip in the vitreous humor with the fundus camera. When the probe is just visible, it is approximately 10-100μm in front of the pigment epithelium. With the probe visible, the animal holder is adjusted until the probe tip is in the approximate center of the retinal image. The direct absorption characteristic of the thermocouple during 1.6 millisecond shuttered laser pulses is used to position the probe in the center of the beam (point of maximum temperature increase due to direct absorption) (60). By rotating the animal about the vertical axis of the eye (a horizontal scan), the relative retinal image irradiance profile and image radius are measured by the direct absorption of laser energy by the thermocouple. This measurement is readily quantified because the temperature response time due to direct absorption is much faster than that due to conducted heat (32). Temperature changes in the probe resulting from direct absorption of incident

radiation appear as a step increase with the onset of the light pulse and a step decrease at the end of the light pulse.

The probe is withdrawn to the center of the pigment epithelium from the vitreous in 2-10μm steps. The position of maximum temperature rise due to conduction for irradiations of ten milliseconds is theoretically in or near the pigment epithelium. From this reference point in the center of the laser beam and the axial position of highest temperature rise measurements can be made radially and axially in the fundus. The position of the temperature probe with respect to the retinal image may be varied in the horizontal plane of the eye in 4μm to 100μm steps to provide radial measurements (horizontal scan). Measurement may be made along the path of the probe of insertion in 2μm or larger steps to provide temperature measurement in the axial direction. Generally, the probe track is at an angle of 10° to 30° for macular insertions. Fundus temperatures are measured for variations in light duration from .0016 second to 10 seconds. All measurements represent temperature variation from a reference value of $37^{o}C$.

Retinal temperature is monitored and maintained at $37^{o}C$ $\pm$ $1^{o}C$ for all threshold measurements. The $37^{o}C$ baseline is set prior to probe insertion by inserting the probe in a water bath maintained at $37^{o}C$. The baseline is set on a Brush stripchart recorder and the null adjustment on the thermocouple amplifier is set to give 0 volts output for the probe in the $37^{o}C$ bath.

An infrared lamp is used to maintain the fundus at 37°C throughout the experiment. The sclera is kept moist with cotton soaked in saline which is positioned around the thermocouple probe.

Generally, the following measurements were taken in an experimental run:

1. Relative irradiance profile across the laser image on the retina.
2. Horizontal temperature profile in the axial hot spot, using 10 second or shorter laser pulses.
3. Temperature-time history for a 10 second or shorter laser pulse, measured at the center of the image and in the axial position of highest temperature rise.
4. Axial temperature profile through the pigment epithelium and choroid following 1.6 millisecond to 10 second laser pulses.
5. Temperature rise at the center of the image versus corneal power.

A horizontal scan in the vitreous humor was taken for each run in the following manner. The probe was inserted into the vitreous where it was clearly visible and in the center of the retinal image. The animal positioning device was rotated, which rotated the monkey eye and, hence, the probe tip through the retinal image. The retinal image did not rotate with the eye, but remained fixed in space as shown schematically in Figure 6.

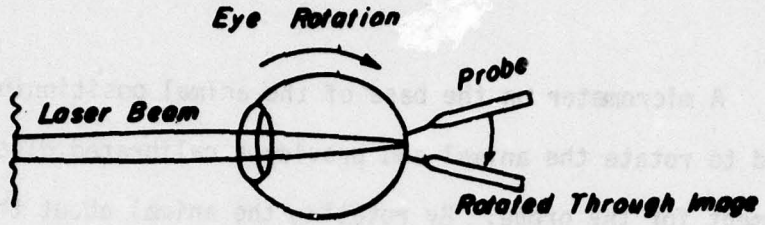

FIGURE 6. Horizontal Scan of Probe Through Retinal Image

The probe and eye were rotated in steps through the retinal image. At each step, a 1.6 millisecond pulse of light was gated into the eye with a shutter. The temperature increase at each step due to direct light absorption in the thermocouple provided a relative measure of the irradiance at that point in the plane of the retina.

As described previously, a temperature rise due to direct light absorption was readily quantified because its response time was much faster than that of conducted heat. In the vitreous, the separation of components was even greater. The medium surrounding the probe had a very low absorption itself, and conduction of heat from the P.E. required roughly a millisecond. The temperature changes due to direct absorption appeared first as an increase with the same rise time as the corneal power pulse, and then a step decrease of the same magnitude when the laser was cut off. A calibration relating the temperature increase to irradiance

magnitude was not performed; the values obtained were relative ones.

A micrometer on the base of the animal positioning device was used to rotate the animal and provide a calibrated distance measurement for the probe. By rotating the animal about the vertical axis of the eye, the laser image remained fixed in space. Movement of the probe 480μm in the plane of the retina corresponded to approximately a two-degree rotation of the eye. The image viewed at the sclera with a fixed microscope did not appear to move in space when the animal was rotated.

If the axis of rotation were in front of the cornea, the laser image would follow the probe and artificially broaden the retinal image. Likewise, if the axis were behind the lens, the image would be artificially narrowed. It should be pointed out that the stability of the laser image could not be determined by observing it through the fundus camera. Of significance was the fact that the probe tip had to move horizontally only a millimeter or less to scan the complete image. Thus, small angular rotations were adequate.

The irradiance profile and retinal image radii for a run were determined from a graph of probe potential versus horizontal distance, the potential being measured at the completion of the shutter opening. Profiles were normalized to a value of 1.0 at the center of the image, and image radii were read from the graph.

Subthreshold temperature measurements are made with the probe centered on the laser image and in the axial hot spot. Several experimental runs for subthreshold laser exposures are made for exposure durations from .002 second to 10 seconds and retinal images of 100 to 200μm. Thresholds are then determined at positions 1/2 to 2 millimeters on either side of the probe insertion site for various times of exposure. The threshold temperature is then extrapolated from the subthreshold measurements to the threshold laser power value. Laser power is measured for each run. The relative temperature rise in the eye is measured with respect to a 37°C reference junction which is maintained within ±.05°C by a proportionally controlled oven. The system bandwidth for the thermocouple measurement is D.C. to 10KHz. Measurement error of the system is estimated to be ±.2°C.

An ophthalmoscopically visible threshold lesion when viewed through the fundus camera is a circular gray or white region with radius of 25 to 200μm, depending on the duration of exposure, image size, and time elapsed between irradiation and observation. The threshold temperature actually occurs, not at the center of the image, but some distance from the center probably near the radial boundary of the lesion. Consequently, once the lesion radius is measured, the threshold temperature is the maximum temperature in the experimental temperature-time profile at the distance equal to the lesion radius. For a

comparison of experimental results with the damage model, the radius is measured with the fundus camera reticle.

In Figure 7, the laboratory arrangement of the experimental instruments is illustrated. The Argon laser provides a maximum power of one watt at the 4880Å wavelength used in this research. The shutter in front of the laser is used to select the exposure duration. For subthreshold exposures and for threshold determinations, the laser power is controlled to within 4% by neutral density filter placed either between the laser and the shutter or in front of the shutter. Optics in the laser path are used to modify the laser beam by providing one or two lens focus of the beam near the cornea of the animal's eye. A beam splitter allows the simultaneous viewing, measurement and exposure of the fundus. The fundus camera is used to observe and photograph the retina before and after lesion production. The power for each exposure is measured by the radiometer through the beam splitter. Calibrations of the amount of light transmitted to the radiometer and reflected into the animal's eye are performed with the radiometer.

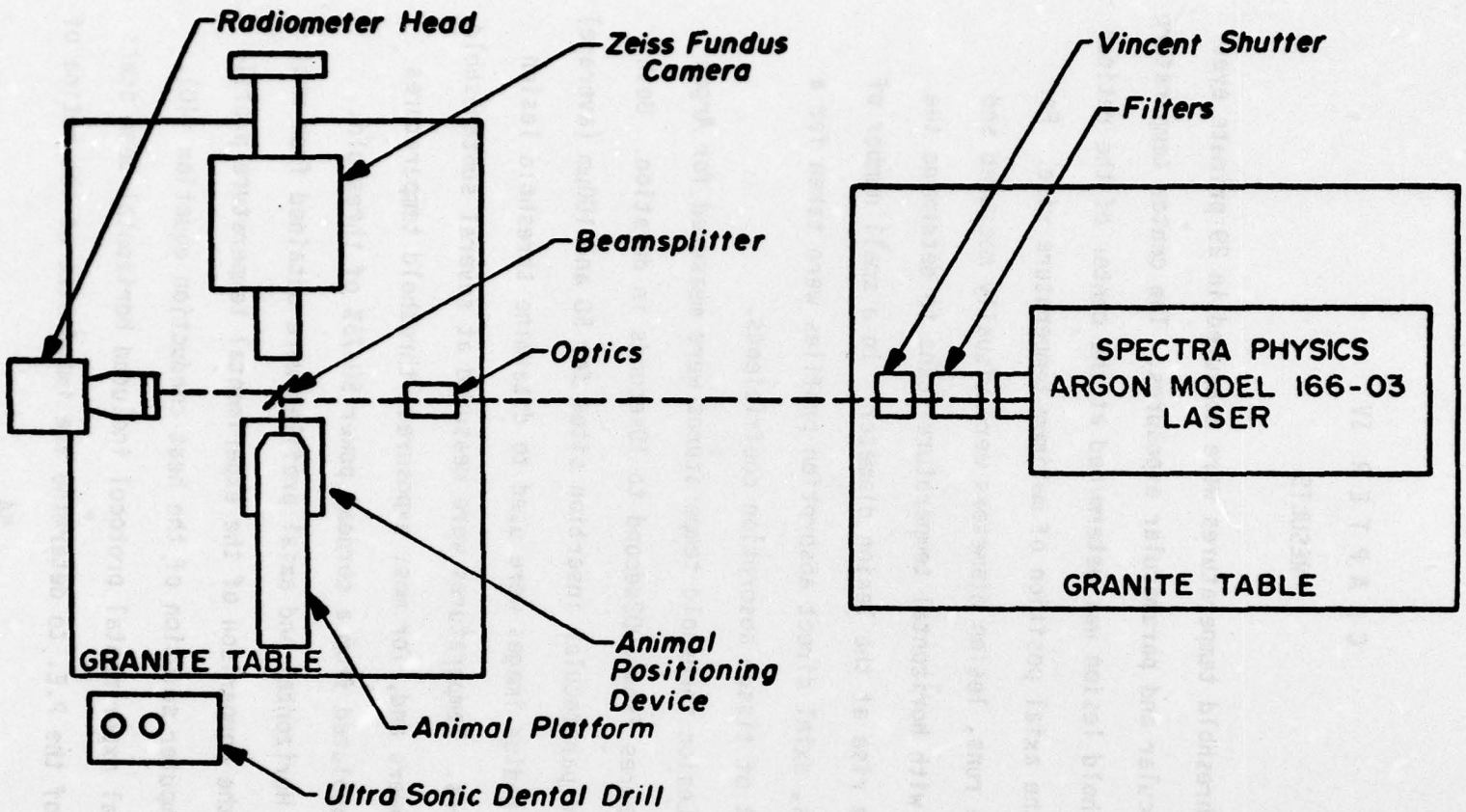

FIGURE 7: Laboratory arrangement of instruments.

CHAPTER IV

RESULTS

Threshold temperatures were measured in 29 primate eyes for both macular and paramacular exposures. The center temperature for a threshold lesion was determined at the center of the retinal image and the axial position of maximum temperature rise. For some of the runs, lesion diameters were visually measured and correlated with horizontal temperature scans to determine the temperature rise at the lesion diameter. In a small number of experiments, axial direct absorption profiles were taken for a measurement of tissue absorption coefficients.

Lesion threshold temperatures were measured for Argon laser exposures from .002second to 10seconds in duration. Both macular and paramacular insertion sites for 50 and 100μm (average) 1/2-power radius images were used to determine threshold lesion temperatures. Temperatures were measured at several subthreshold corneal powers and, for most exposures, threshold temperatures were extrapolated from a corneal power 50-75% of threshold.

Horizontal and axial profiles were obtained from most eyes for the comparison of the experimental temperature profile with a computer solution of the heat conduction equation (40). The general experimental protocol included horizontal beam scans in front of the P.E. to determine the image size at the retina of

the monkey eye. Horizontal temperature scans were accomplished at several times and corneal powers with the thermocouple placed in the hottest position in the beam profile and tissue. Axial scans from the neural layers back to the sclera were done at the conclusion of the experiment for a particular insertion.

The "threshold" temperature rise in this report is the temperature rise of the P.E. in the center of the beam that is associated with the appearance of an ophthalmoscopically visible lesion 5 minutes post exposure. The lesion radius "threshold" temperature rise is the estimated temperature at the lesion radius obtained from measurements of lesion size, lesion center temperature, and horizontal temperature scans. All exposures presented were obtained with an Argon (4880Å or all lines) laser. Irradiation duration was controlled by a mechanical shutter with an opening time (for the laser beam) of approximately .0002 second.

In this section, the threshold measurements, the prediction of temperature in the retinal tissues, and a comparison of lesion measurements with a simple rate process model will be discussed.

Temperature Rise Versus Corneal Power

For each experiment, several subthreshold corneal powers are used to construct a temperature versus corneal power graph for extrapolation to the threshold corneal power. In Figure 8 is shown

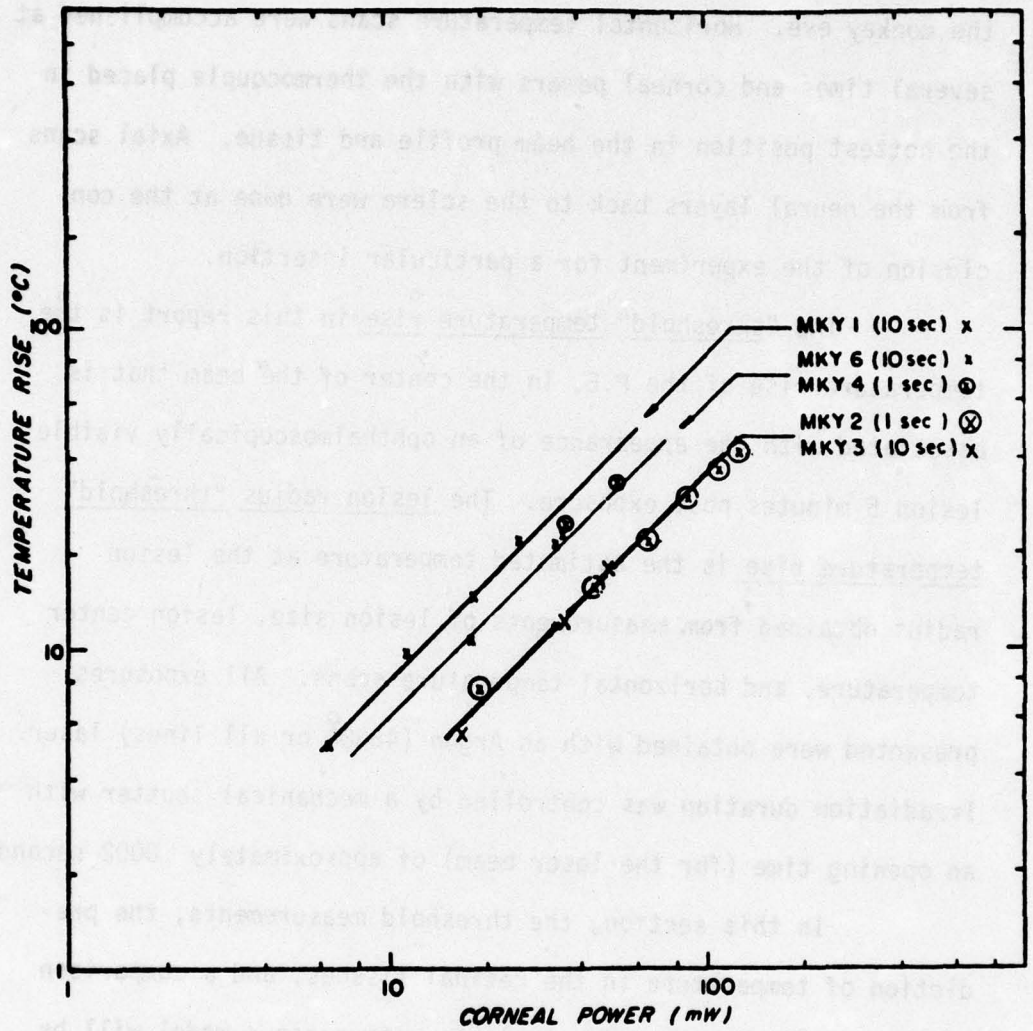

FIGURE 8: Temperature rise versus corneal power for five experiments.

a plot of temperature rise versus corneal power for five experiments. The straight lines through the data are drawn with a slope of one to illustrate the linearity of temperature with corneal power. The profiles for these measurements are all approximately truncated gaussian profiles with half power radii ranging from 35μm to 125μm. The corneal power is adjusted with neutral density filters and the temperatures are recorded at the end of 1 and 10 second laser pulses.

The differences between the center temperatures for a given corneal power are due to the differences in half power radii for the experimental temperature versus corneal power measurements. For example, the profile for the experiment denoted by monkey 1 has a half power radius of 35μm, the retina profile for monkey 6 has a half power radius of 98μm and the half power radius for the retina image for monkey 2 is 125μm.

Threshold Temperature Measurements

Threshold temperatures associated with the appearance of an ophthalmoscopically visible lesion 5 minutes post exposure are measured both at the center of the image and at the lesion radius. The center threshold temperature is the increase in temperature relative to 37°C baseline fundus temperature. The lesion radius temperature measurement is determined from subthreshold corneal power and horizontal (radial) scans of the retinal temperature

profile. The temperature at the lesion radius is extrapolated from the horizontal scan and the ophthalmoscopic measurement of the gray or white lesion radius. The measurements of temperature increase are accomplished with the thermocouple probe described earlier, while the thresholds are determined from a series of exposures near the probe insertion site for varying corneal power. The corneal power for the threshold is adjusted by neutral density filters from a value 50 to 100% above threshold to 20 to 50% below threshold. The value of corneal power which produces a burn which is visible 5 minutes post exposure is the threshold corneal power. Corneal powers above these values always produce a lesion before 5 minutes has elapsed. Power levels below the threshold corneal power do not produce a lesion within 5 minutes.

A summary of the threshold temperature rise at the center of the lesion for exposure durations from .002 second to 10 seconds is presented in Table V. The values in this table are extrapolated from subthreshold temperature measurements at the center of the image and at the axial position of highest temperature rise. All values in the table are referenced to the baseline fundus temperature of 37°C. Both macular exposures and paramacular exposures (temporal to the macula) are presented. The number of thresholds determined at each exposure duration with the mean temperature rise and standard deviation are listed.

TABLE V: Summary of Threshold Temperature Measurements

Exposure Duration	Paramacular Number	Paramacular Mean	Paramacular SD	Macular Number	Macular Mean	Macular SD
10s	7	24.8	1.7	13	19.9	1.5
1s	8	28.7	3.0	14	24.1	3.4
.1	8	39.9	5.1	14	29.4	4.1
.06				1	32.0	
.05	1	57.6				
.04	2	57.8	7.4	4	34.3	3.8
.035				1	39.2	
.03	1	43.0				
.02	2	52.0	8.5	1	47.2	
.01	3	55.9	14.6	2	66.1	44.3
.002	1	84.0				

At 10 seconds, 7 paramacular and 13 macular threshold measurements yield average temperature increases of 24.8°C and 19.9°C respectively; the standard deviations of the 10 second threshold temperature increases are 1.7°C for paramacular exposures and 1.5°C for macular exposures. For one second exposures, the temperature rise required to produce a visible lesion increases to 28.7°C and 27.1°C for paramacular and macular insertion sites. At 0.1 second paramacular and macular temperature increases are 39.9°C and 29.4°C respectively.

Generally, the standard deviation of the temperature increases is less for longer curation exposures than it is for shorter duration exposures. Even for longer time measurements for which the number of measurements is nearly the same as for shorter times of exposure, the standard deviation is smaller.

Expressed as percentages of the peak temperature the paramacular standard deviations for 10 second, 1 second, and .1 second duration are 7%, 10%, and 13%, respectively; macular temperature increase standard deviations are 8%, 14% and 14% for the 10 second, 1 second, and .1 second exposures.

In Figure 9 is illustrated the average temperature rise versus exposure duration. The figure is a plot of the data in Table V. The temperature increase for the appearance of a visible lesion is lower for macular exposures than for paramacular exposures. This figure illustrates a temperature-time dependence for lesion production which may be different for macular and paramacular sites. For an exposure duration of 10 seconds the macular temperature increase is 80% of the increase required to produce a paramacular lesion. For 1 second and .1 second exposures, the macular increase is 84% and 74% of the paramacular temperature increase respectively, while at .02 second, for a small number of exposures, the macular increase is 91% of the paramacular temperature rise.

For a number of the exposures, lesion radius measurements are accomplished with a reticle in the fundus camera eyepiece. In Table VI, a summary of the measurements of lesions radius and the extrapolated temperature from horizontal profile measurements is presented. The number of lesion measurements, the exposure duration, the lesion radius normalized to the half power radius

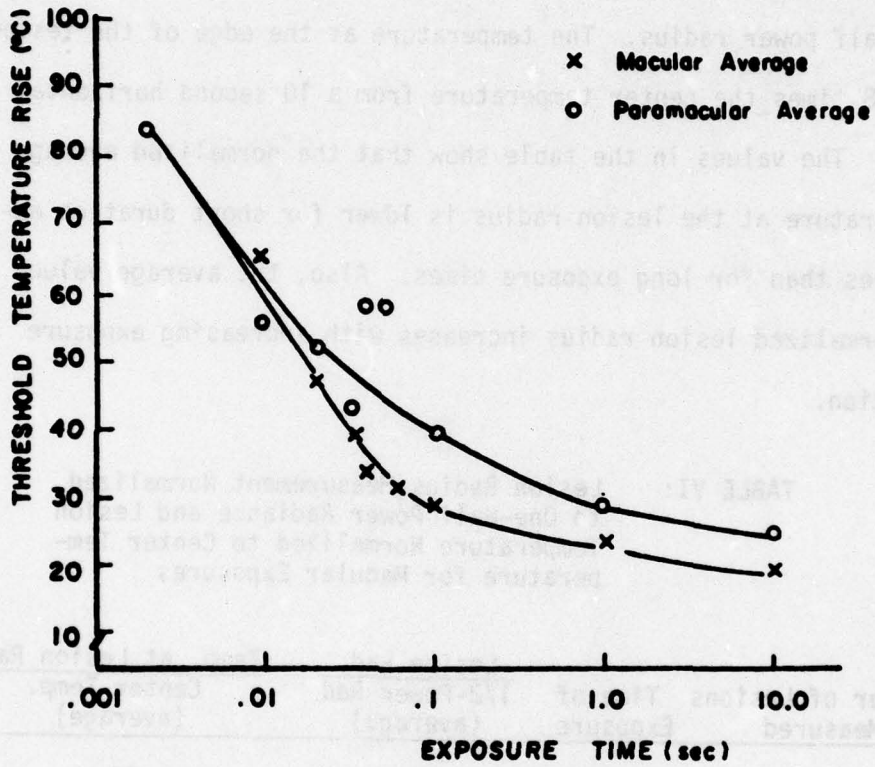

FIGURE 9: Experimental average temperature increases for macular and paramacular Argon laser exposures versus exposure duration.

of the retinal image, and the temperature at the lesion radius normalized to the center temperature are tabulated for exposure duration of .01 second to 10 seconds. At 10 seconds, thirteen lesion measurements yield an average lesion radius of .55 times the half power radius. The temperature at the edge of the lesion is .88 times the center temperature from a 10 second horizontal scan. The values in the table show that the normalized average temperature at the lesion radius is lower for short duration exposures than for long exposure times. Also, the average value of normalized lesion radius increases with increasing exposure duration.

TABLE VI: Lesion Radius Measurement Normalized to One-Half Power Radiance and Lesion Temperature Normalized to Center Temperature for Macular Exposures

Number of Lesions Measured	Time of Exposure	Lesion Rad. / 1/2-Power Rad. (average)	Temp. at Lesion Rad. / Center Temp. (average)
13	10.0s	.55	.88
12	1.0	.45	.82
13	.1	.33	.75
7	.01	.30	.58

Thermal Model Parameters

The source term in the heat conduction equation includes the absorption of the various layers in the ocular fundus and the retinal distribution of the input light energy. The source term also depends upon the value of the transmission of the preretinal ocular media (TOM). Tissue thermal parameters conductivity (k) and volumetric specific heat (ρc) also affect the solution for retinal temperature increase.

In Figure 10 is illustrated the effect of changing the transmission of the preretinal ocular media in the model. Changing the transmission of the preretinal ocular media from .79 to .51 in Figure 10, results in a reduction in the temperature increase for all times in the 10 second temperature-time history. The transmission parameter of .51 is 65% of the parameter .79. The temperature versus time for the two values of transmission exhibit the same decrease of 35% for the decrease in TOM from .79 to .51.

In Figure 11, model calculation of temperature rise versus corneal power is illustrated for times of .01 second, .1 second and 1 second. The temperature increases for a corneal power of 10 milliwatts are half the increases for 20 milliwatts corneal power. The temperature increase for all times of exposure is linear with corneal power. An increase in corneal power

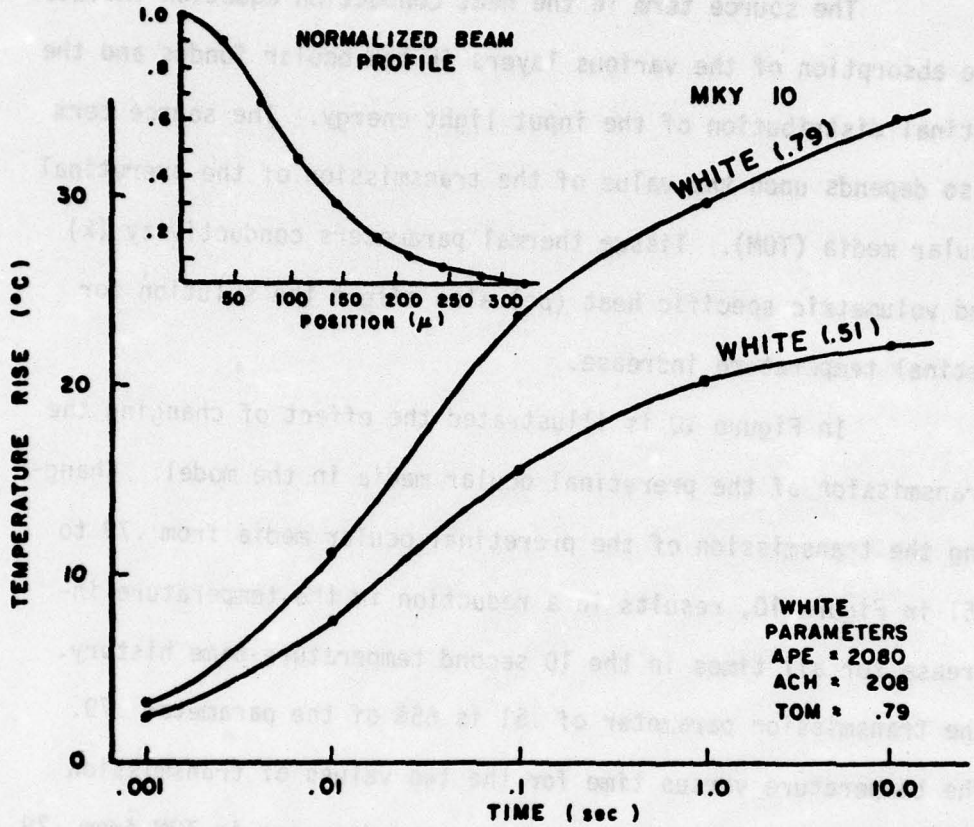

FIGURE 10: Model calculated temperature-time history for two values of transmission of the pre-retinal ocular media (TOM). Values for TOM of .79 and .51 are used for calculations of temperature as a function of time for the profile and absorpiton parameters shown on the figure.

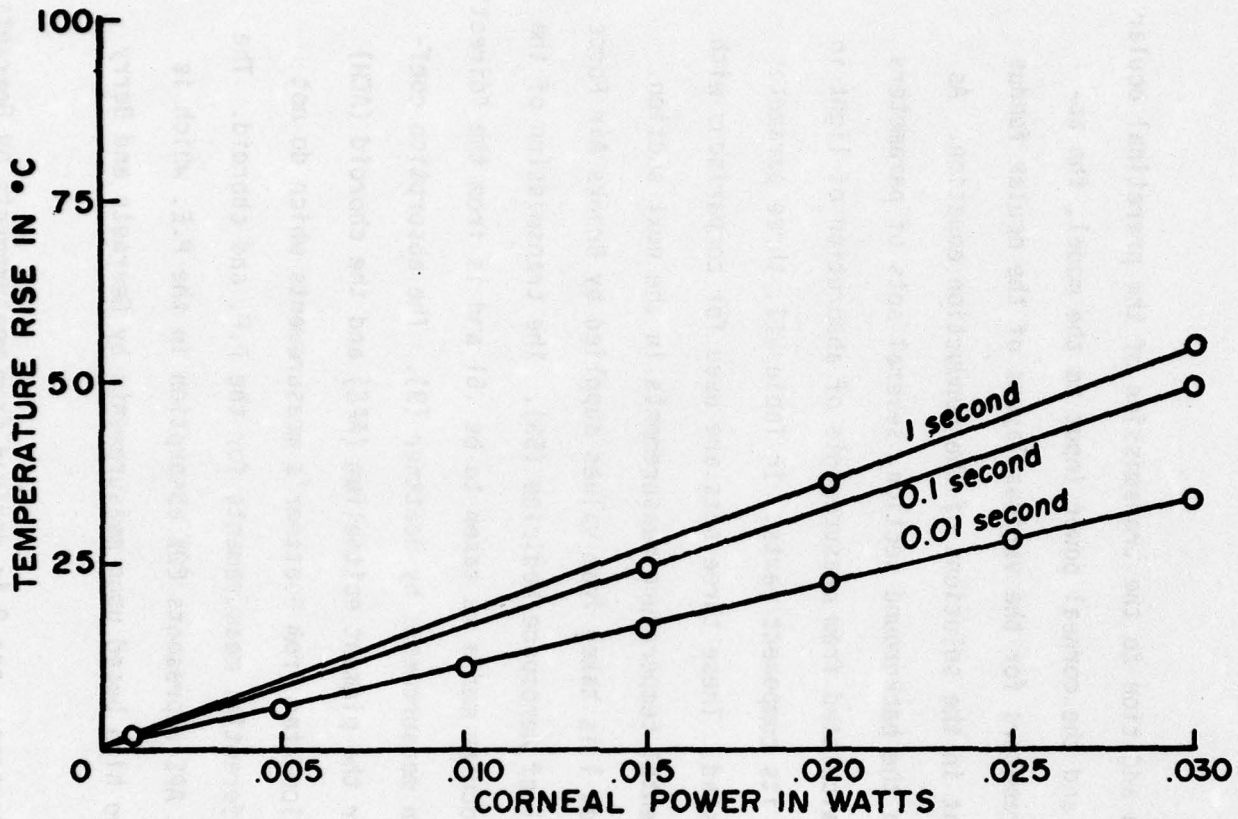

FIGURE 11: Calculated temperature as a function of corneal power for times of .01 second, .1 second and 1 second during a 1 second exposure.

is accompanied by the same percentage increase in temperature rise.

In addition to the transmission of the preretinal ocular media (TOM) and the corneal power input to the model, the absorption parameters for the various layers of the ocular fundus are important in the solutions of the conduction equation. As mentioned in the background section, several sets of parameters have been calculated from measurements of absorption of light in the eye and its component parts. In Table VII, three parameter sets are listed. These three sets are used for comparisons with the experimental temperature measurements in the next section. Parameter set 1 is taken from values supplied by Brooks Air Force Base, School of Aerospace Medicine (59). The transmission of the preretinal ocular media is taken to be .51 and is from the "direct" transmission measurements by Boettner (9). The absorption coefficients for the pigment epithelium (APE) and the choroid (ACH) are also calculated from Boettner's measurements which do not include differential measurements for the P.E. and choroid. The coefficient APE represents 80% absorption in the P.E. which is probably too high based upon measurements by Geeraets and Berry (7, 8).

Parameter set 2 is derived from measurements by Geeraets and Berry (7, 8). The transmission of the preretinal ocular media represents a trade-off between the total transmission value from

Geeraets and Berry and the direct transmission value from Boettner. The coefficient APE represents a 53% absorption of light energy in the P.E. The choroid absorbs 25% of the light reaching the P.E. This implies that 22% of the light entering the P.E. is transmitted through the choroid to the sclera.

Parameter set 3 is a combination of parameter sets 1 and 2 with an assumed absorption of 33% of the light energy reaching the P.E. in that layer and 58% absorption in the choroid. Of the light reaching the P.E., 9% is transmitted through the choroid into the sclera.

In Figure 12, the absorption of light versus depth from the front of the pigment epithelium for the three parameters sets in Table VII is illustrated. Parameter set 1 represents a high absorption of light in the P.E. Parameter set 3 gives a much larger absorption of light in the choroid, while parameter set 2 represents a lower absorption in the P.E. than set 1, and a lower absorption of light in the choroid than set 3.

TABLE VII: Absorption Parameters for Figure 12

SET	TOM	APE	ACH
1	.51	1622	189
2	.636	637.6	76.28
3	.65	395	195

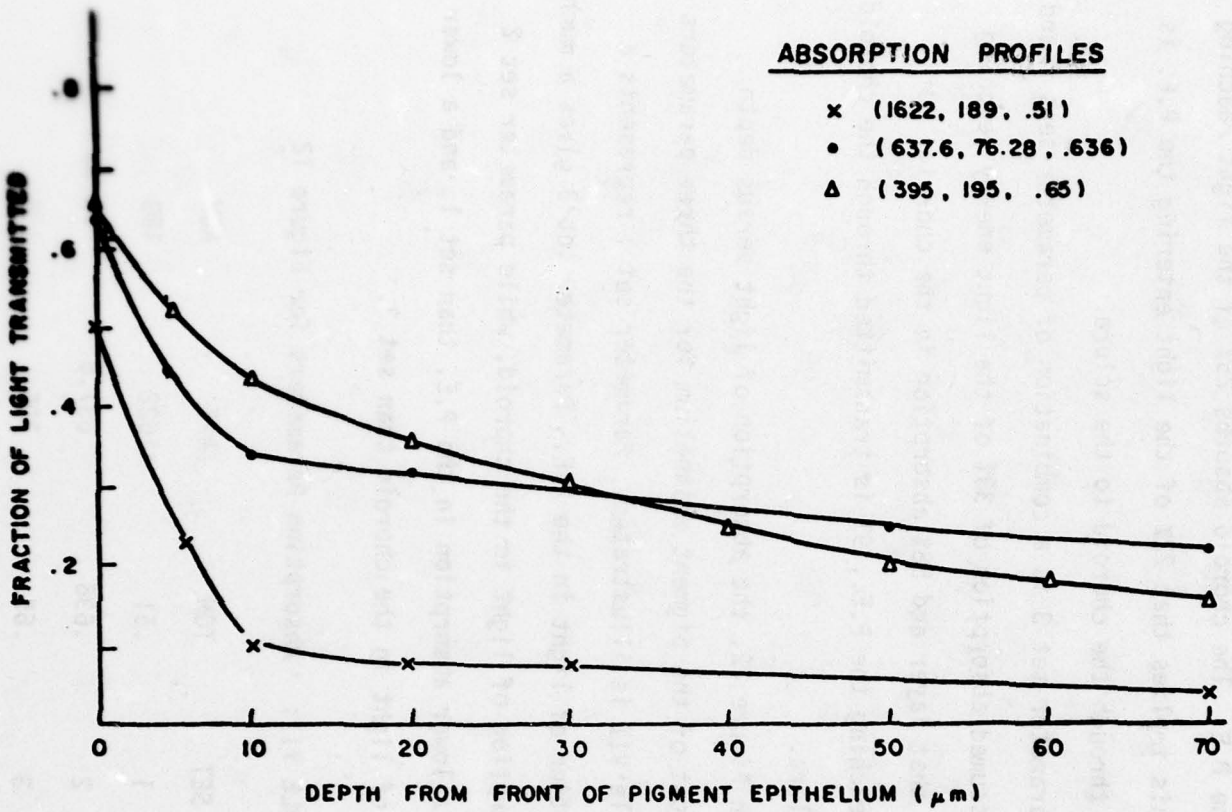

FIGURE 12: Absorption profiles for three parameter sets in Table VII. The axial distance is measured from the front of the pigment epithelium.

Model temperature-time histories for a 1 second exposure for the three parameter sets are illustrated in Figure 13. The temperature-time histories were generated using the experimentally measured retinal intensity profile from MKY8-74 and corneal power of 26 milliwatts. The third parameter set exhibits a longer time constant than the first set since the 10 millisecond temperature is approximately 75% of the temperature rise for set 1, while the 1.0 second temperature increases are almost equal.

The associated temperature decays for the temperature rise in Figure 13 at the end of the 1 second exposure are shown on Figure 14. The decays for sets 1, 2, and 3 indicate slightly different time constants with the time constant for set 3 being the longest. The decay time (time to .368 peak) for set 3 is .03 second. For set 1 the decay time is .018 second and for set 2 it is approximately .021 second.

Horizontal scans during the temperature rise for the three sets of model absorption parameters are illustrated in Figure 15. The temperature field at .01 second and 1.0 second for a standard one second exposure are illustrated for all parameter sets. The differences in time constants for the sets may be seen in the comparison of the .01 second and 1 second horizontal scans. The 1 second scan indicates that the peak temperatures for sets 1 and 3 are nearly the same while at .01 second the peak temperatures for sets 1 and 3 are nearly the same and the peak temperatures

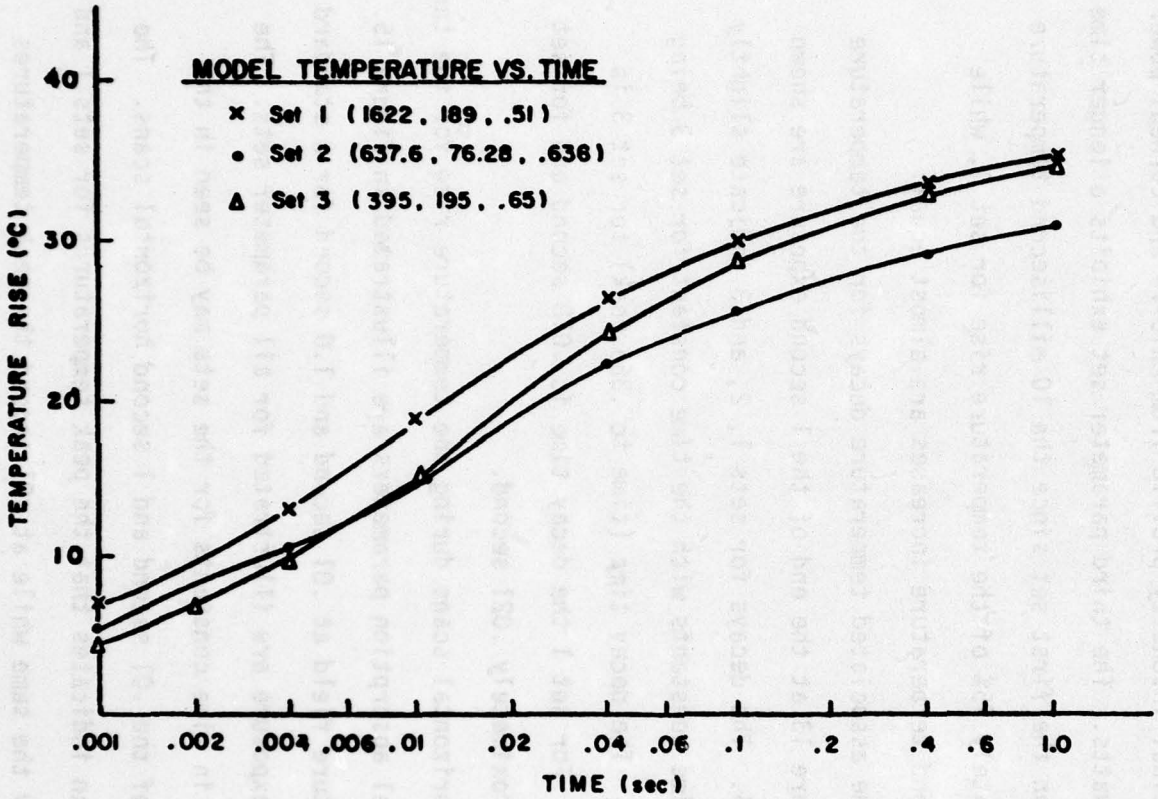

FIGURE 13: Model calculated temperature rise for a 1 second exposure for three parameter sets.

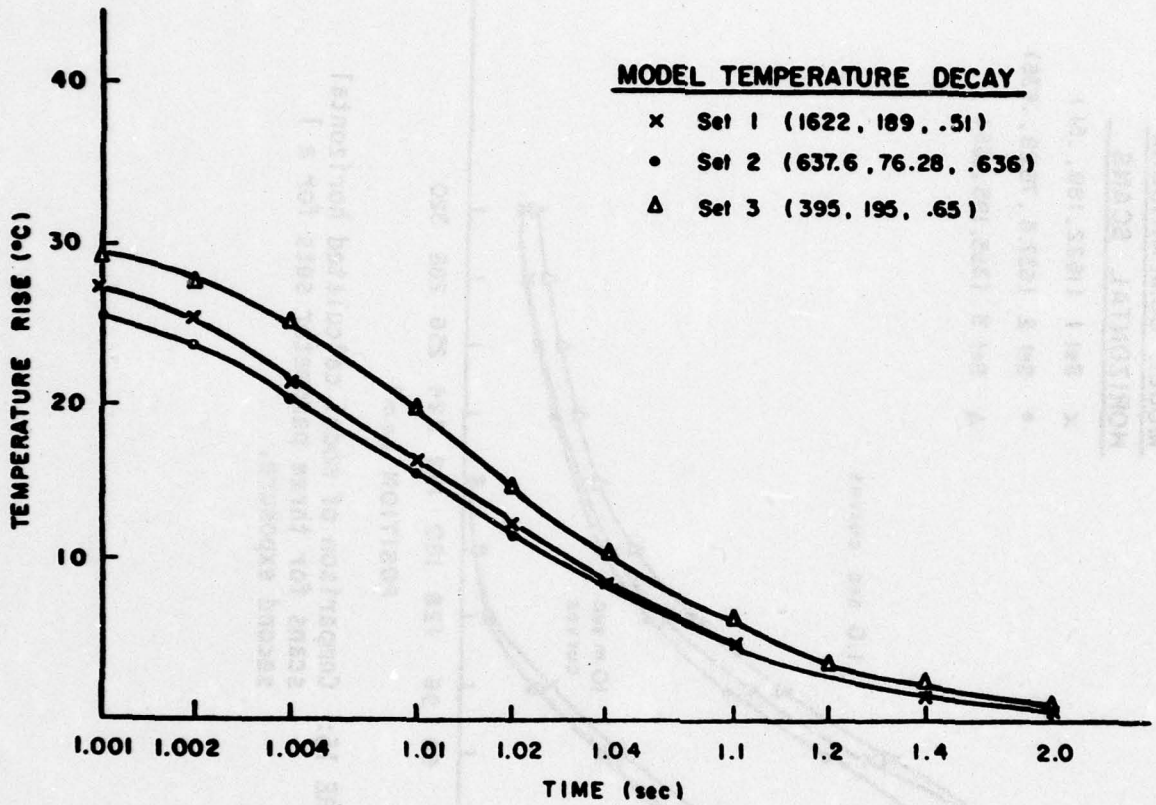

FIGURE 14: Model calculated temperature decay following 1 second rise in Figure 13 for the three parameter sets in Table VII.

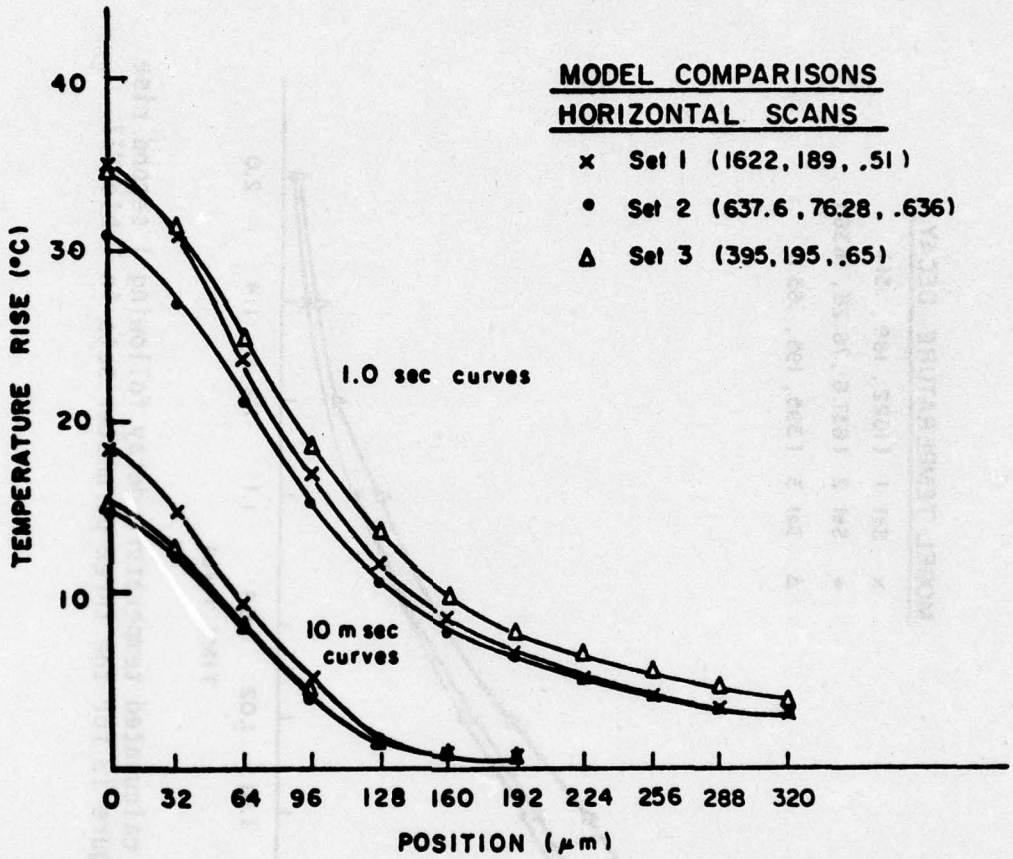

FIGURE 15: Comparison of model calculated horizontal scans for three parameter sets for a 1 second exposure.

for sets 2 and 3 are closely matched. The 1 second profile for set 3 is spread more radially than set 1.

The ratios of peak temperatures at .01 second to peak temperatures at 1 second are .53, .49, and .44 for sets 1, 2, and 3, respectively. The time constant, therefore, increases with decreasing absorption in the pigment epithelium. This reduces the P.E. source term and reduces short time temperatures. At long times, the temperature is a function of the energy deposited in the P.E. and choroid and the tissue conductivity. The total energy deposition is approximately equal for parameter sets 1 and 3, whereas the total energy deposition for set 2 is less than sets 1 and 3.

The axial profiles shown in Figure 16 illustrate the differences in model tissue volume heated by the energy deposited in retinal tissue by the three model parameter sets. The third set heats a larger volume of tissue to a higher temperature for the same irradiance profile at the front of the P.E. The axial position of highest temperature rise for sets 1 and 2 is at the center of the P.E., while for set 3 it is approximately 20μm behind the front of the P.E.

Once appropriate values have been chosen for the transmission, absorption and thermal parameters in the model, one more important parameter remains. The radius of the retinal image is extremely important in the accurate prediction of temperature.

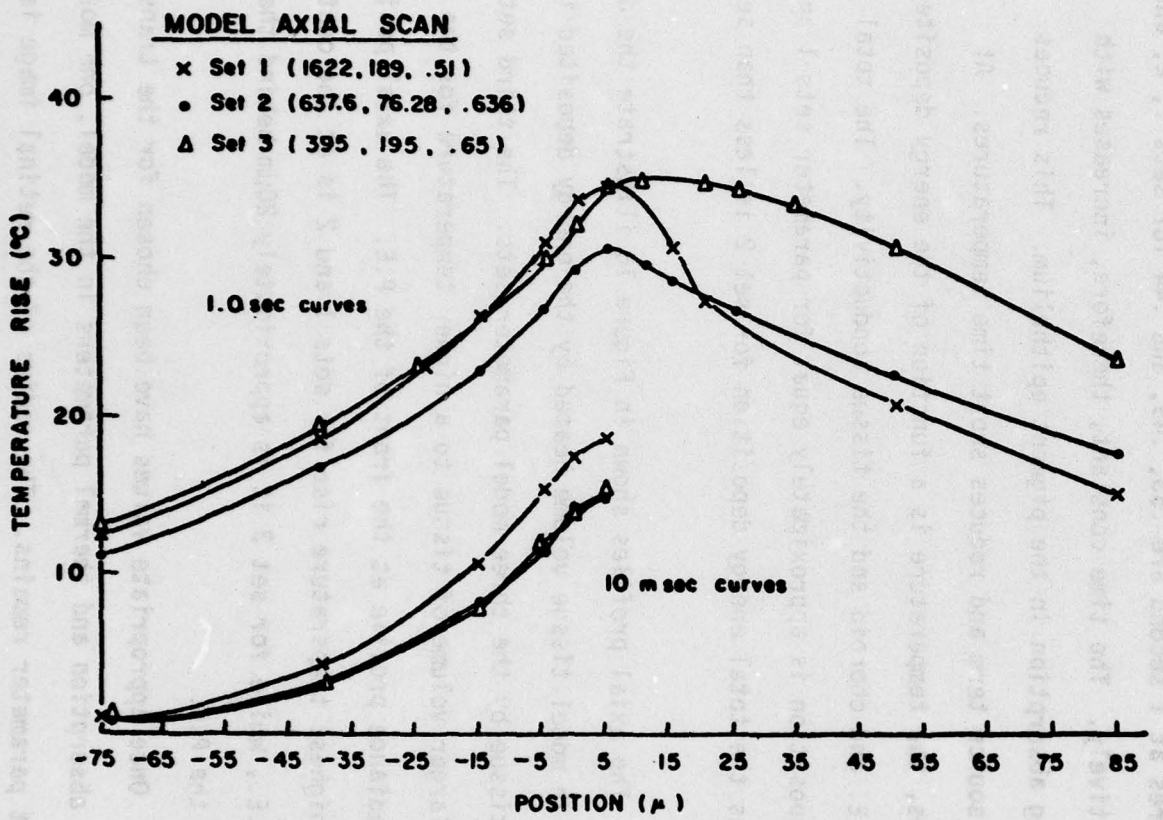

FIGURE 16: Model calculated axial scans for three parameter sets for a 1 second exposure.

For small images, the rise time of the temperature increase near the center of the image is much faster than the rise time for larger images. The image radius at the retina is measured during a horizontal scan with the thermocouple in the neural layers of the retina at a point where a large direct absorption and small tissue rise is present. Alternative methods for the determination of image size at the retina are from the geometric optics of the imaging system or from the point spread function of the eye convolved with the geometric image.

The effect of image radius on the rise time of computed temperature time histories is shown in Figure 17. For example, a 60% error in the measurement of maximum image radius (RIM) when the actual value is 160μm, would produce errors of 56%, 18% and 3% at .01 second, .1 second, and 1.0 second in a 10 second exposure calculation for the normalized temperature increase. However, measurement errors of 10% in RIM would not produce excessive errors in the computations of temperature for times greater than .01 second. Five different model parameter sets are used for calculation of the temperature rise in this figure.

For the model set with parameter set 3, the time to 90% of the 10 second temperature for a 23μm image is 22 milliseconds which is nearly the same as for the model with set 1 for a 40μm image radius. The model parameter set 3 (395, 195, .65) exhibits a longer rise time for a 150μm image than model set 1 (1622, 189,

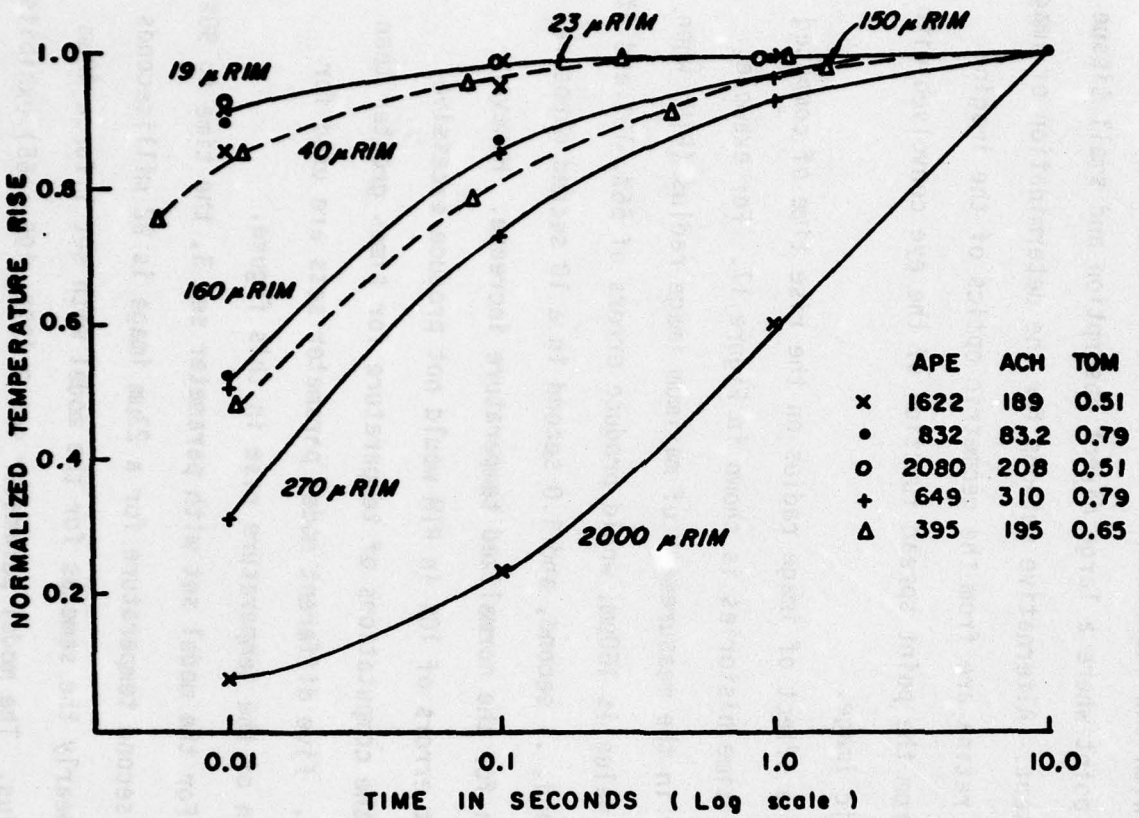

FIGURE 17: Calculated temperature versus time for 10 second exposures for varying image radii. Five model parameter sets are used to calculate the temperature rise. Temperature time profiles are normalized to the 10 second temperature rise for the particular beam profile and model parameter set.

.51) for a 160μm image radius. For model set 1 the time to 90% of the 10 second temperature versus image radius is 22 milliseconds for a 40μm image and 5.7 seconds for a 2000μm image radius. The time to 90% of the 10 second temperature for parameter set 3 is .29 seconds for a 150μm radius and 22 milliseconds for a 23μm image radius. The ratio of the heated volumes for set 3 and the 150μm image to the 23μm image is 42.5 while the rise time ratio is 12.6.

Comparison of Experimental and Model Threshold Temperatures

For most of the experimental thresholds the solution to the heat conduction equation is computed with the measured retinal profile and the threshold corneal power for the absorption and transmission parameter sets given in Table VII. The data are grouped according to lesion location (macular or paramacular). Within each group the data are divided by the corneal power required to produce a visible lesion for a given image size and the general shape of the image. A larger image requires a higher corneal power to produce a threshold lesion than a smaller image. If the half-power points are nearly equal the tail of the distribution of retinal power is larger for one image than another, the image with large tails requires a higher power to produce a visible lesion.

In Table VIII, threshold lesion temperatures at the radial center of the image and the axial position of highest temperature

TABLE VIII: Ten Second Threshold Data.

Experimental Subject	Image Radius (μm)	1/2-Power Radius (μm)	Experimental Temperature (°C)		Model set 1 Temperature (°C)		Model set 2 Temperature (°C)		Model set 3 Temperature (°C)		CP (mM)	
			M	P	M	P	M	P	M	P	M	P
1-73	168	35		24				14.7		29.3		27
2-73	400	125		22				14.6		17.5		33
3-73	230	75		24.1				30.5				33
4-73	350	100		24.5				17.5				29
6-73	480	98	17.5				17.1		20.3		33	
	480	98	19.6				15.6		18.5		30	
	480	98	20.8				19.2		22.8		37	
8-73	176	50		26.4		21.5		21.2		22.6		18.5
		50	21.5						19.9		16.3	
9-73	380	105		27		22.3		20.8		24.6		37.4
		105	21.2		16.1		15.0		17.8		27	
10-73	320	90		25.3				19.9		30.5		26.2
11-73	400	75	21.5		19.3				20.0		25	
12-73	176	53	21.5		22.5		20.1		25.1		19	
13-73	192	65	17.5				16.4		19.0		18	
15-73	152	40	19.5				18.1				12.5	
	144	30	20.3				22.6				13	
17-73	380	100	19.0				20.8				37.7	
18-73	210	75	18.0								18.5	
19-73	200	80	21.0								20.5	
$\bar{x}$			19.9	24.8	19.3	21.9	18.3	19.9	20.4	24.9		
s			1.5	1.7	3.2	.6	2.6	5.4	2.4	5.3		
n			13	7	3	2	9	7	8	5		

increase are presented for a 10 second exposure. In the table, the maximum image radius (RIM), the half-power radius, experimental and model temperatures for macular (M) and paramacular (P) insertion sites and the threshold corneal power are presented for each experiment. For 13 macular insertions, the mean experimental temperature rise is 19.9°C with a standard deviation of 1.5°C. For model set 3 the average temperature increases for macular and paramacular exposures are 20.4 ± 2.4°C and 24.9 ± 5.3°C respectively. No average values for corneal power are given, since the threshold corneal power depends not only upon the image size and distribution but also the insertion site.

Threshold data for one second exposures are shown in Table IX. Experimentally measured temperatures at the center of the visible lesion are 24.1°C ± 3.4°C for macular exposures and 28.7°C ± 3.0°C for exposures in the paramacular region temporal to the macula. The average temperature for the macular exposures with set 2 excludes one data point for experiment 2/11/75 which indicates a much higher than average temperature rise of 60.7°C.

Exposures of .1 second duration which produce threshold visible lesions and the associated temperature increase at lesion center are listed in Table X. Fifteen macular exposures and 8 paramacular exposures yield average experimental temperature increases of 29.4°C ± 3.9°C and 40.0°C ± 5.1°C. The total corneal power required to produce a visible lesion 5 minutes post exposure

TABLE IX: One Second Threshold Data

Experimental Subject	Image Radius (μm)	1/2-Power Radius (μm)	Experimental Temerpature (°C)		Model set 1 Temperature (°C)		Model set 2 Temperature (°C)		Model set 3 Temperature (°C)		CP (mW)	
			M	P	M	P	M	P	M	P	M	P
3-73	230	75		25.8				35.2				42
4-73	350	100		26.0				19.6				38.4
6-73	480	98	23.6				22.6		26.6		49	
	480	98	24.2				18.9		22.3		41	
	480	98	28.2				24.9		29.3		54	
8-73	176	50		32.8		29.4		26.1		29.3		26
9-73	380	105		31.8		28.2		26		30.2		52.5
	380	105	28.4		20.2		18.6		21.6		37.5	
10-73	320	90		28				22.1		34.3		
11-73	400	75	27		29.6		26.1		29.8		41.6	
12-73	176	53	22.3		27.1		25.5		27.6		23.2	
13-73	192	65	22				20.2		23.5		23.9	
2/11/75	192	50	31.7				60.7*				70	
15-73	152	40	21				20.6				16.2	
	144	30	22				30.4				18.3	
1-74	247	105	22.6		17.7		15.0		17.4		28.8	
3-74	285	75		25.7		20.3		18.5		21.3		31.6
4-74	237	80	21.0		19.1		17.1		19.9		28.8	
8-74	152	50		32.0		32.3		28.5		31.7		26
9-74	400	240	21.7		18.4						44.5	
10-74	168	104	21.0		25.2		22.8		26.4		27.4	
11-74	144	78		27.8		26.1						21.5
$\bar{x}$			24.1	28.7	21.8	27.3	24.9	25.1	24.4	29.4		
s			3.4	3.0	5.7	4.5	11.5	5.8	4.6	4.9		
n			14	8	7	5	13	7	10	5		
							21.9*					
							4.4					
							12					

*Not included in average denoted by *

TABLE X: Threshold Data for .1 Second Exposures

Experimental Subject	Image Radius (μm)	1/2-Power Radius (μm)	Experimental Temperature (°C)		Model set 1 Temperature (°C)		Model set 2 Temperature (°C)		Model set 3 Temperature (°C)		CP (mM)	
			M	P	M	P	M	P	M	P	M	P
3-73	230	75		37				58				84
6-73	480	98	35.2				31.2		36.3		98	
	480	98	28.1				25.6		30.0		81	
	480	98	33.6				33.4		38.9		105	
8-73	176	50		42		57		49.5		54.4		60
9-73	380	105		40		38.5		34.4		38.9		101
	380	105	34.4		27.4		24.6		27.8		72.1	
10-73	320	90	30.1				32.2		55.8*		62.6	
11-73	400	75	30.1		39.2		33.6		37.2		71	
12-73	176	53	26.4		31.2		30.4		31.6		33	
2-11-75	192	50	34.5		120 *						173	
1-23-75	72	43	28.6		70.9*						39	
15-73	152	40	24.2				41.8				28	
1-74	247	105	24.2		26.3		19.4		22.1		54.7	
3-74	285	75		35.9		33.2		29.3		32.8		69
4-74	237	80	23.4		28.8		24.8		28.1		58	
5-74	285	100	31.8		30.3		27.0		31.1		65	
6-74	144	75		39.7		49.6		44.2		48.3		51.2
8-74	152	50		38.8		55.3		47.9		52.1		52.3
9-74	400	240	26.8		13.3						83.8	
10-74	168	104	29		37.9		33.5		38.1		51.3	
11-74	144	78		51.3*		54.3						53.5
1-21-75	248	88	35			46.3		41.0		46.4		75
$\bar{x}$			29.4	40.0	42.5	47.7	29.8	43.5	34.3	45.5		
s			3.9	5.1	21.0	9.0	5.9	9.6	8.8	8.2		
n			15	8	10	7	7	12	7	11		
				38.3*	29.3*					32.1		
				2.5	8.0					5.4		
				7	8					10		

*Not included in average denoted by *

AD-A035 057 TEXAS UNIV AT AUSTIN ELECTRONICS RESEARCH CENTER F/G 6/18
THE MEASUREMENT OF THRESHOLD TEMPERATURES IN THE OCULAR FUNDUS --ETC(U)
FEB 76 L A PRIEBE, A J WELCH F44620-71-C-0091
UNCLASSIFIED TR-180 AFOSR-TR-77-0005 NL

2 OF 3
AD
A035057

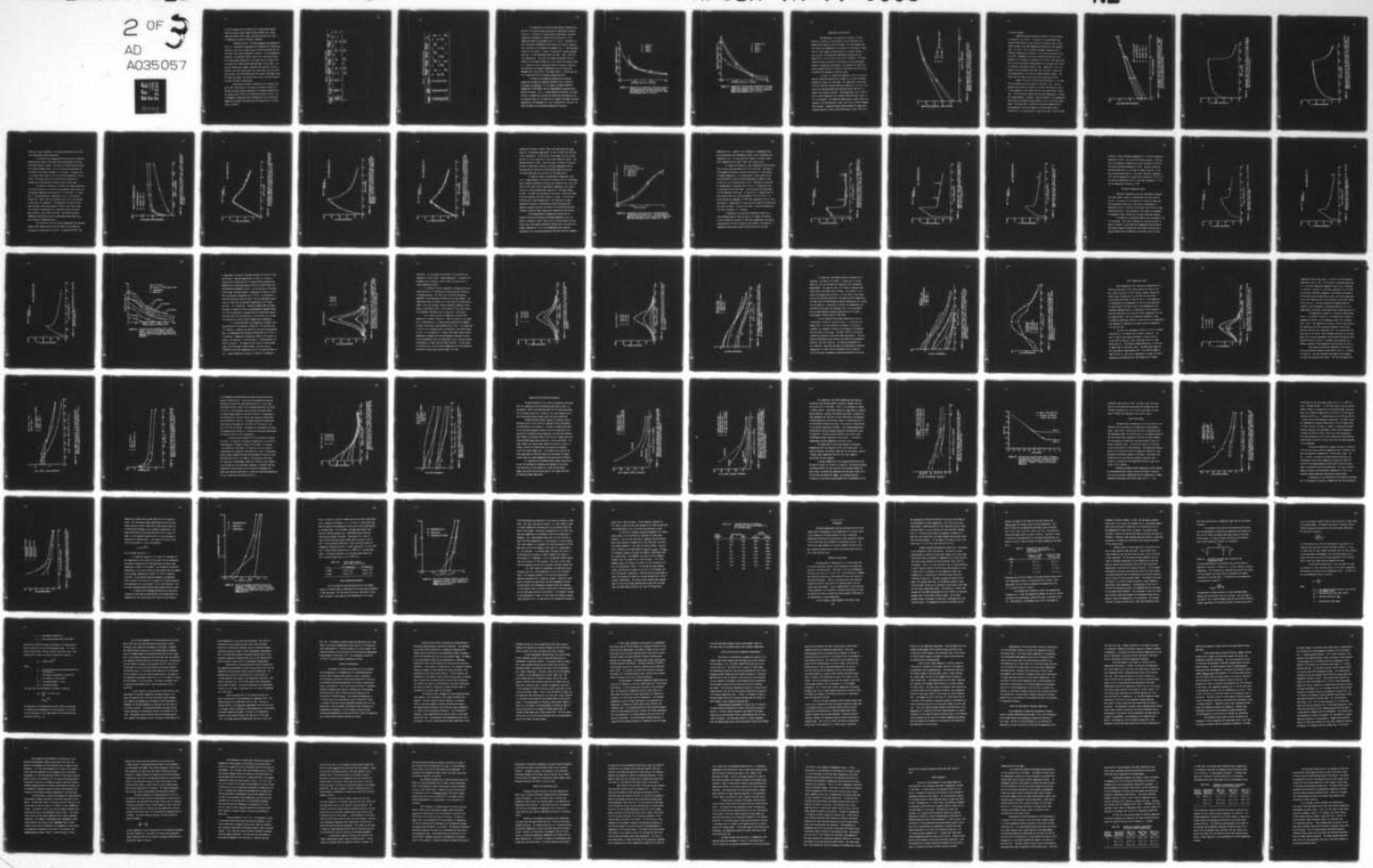

is from a minimum of 28 milliwatts for a 152μm maximum radius (40μm half-power) radius image to 105 milliwatts for a 480μm (98μm half-power) radius image, (excluding the point not used in temperature average) for macular exposures.

Threshold data for .01 second exposures are presented in Table XI. Experimental measurements at 3 macular and 4 paramacular insertion sites yield average values of 66.1°C and 55.9°C for the threshold lesion center temperature increase. For the paramacular exposures, the threshold corneal power varies from 90 milliwatts for an 88μm radius image with a half-power radius of 30μm to 270 milliwatts for a 248μm radius 88μm half-power radius image. The macular temperatures probably represent some anomalies in the experiment since the corneal power for a 72μm image does not differ significantly from the corneal power for a much larger 285μm image. For these two images, the corneal power values are 248 milliwatts and 214 milliwatts, respectively.

Miscellaneous threshold temperatures for exposure durations from .002 second to .05 second are present in Table XII. The data include 4 macular exposures of .04 second duration with an average value of 34°C and a standard deviation of 4.3°C. For 2 extramacular insertions with .04 second duration, the average temperature increase associated with the appearance of a visible lesion is 57.8°C.

TABLE XI: Threshold Data for .01 Second Exposures

Experimental Subject	Image Radius (μm)	1/2-Power Radius (μm)	Experimental Temperature (°C)		Model set 1 Temperature (°C)		Model set 2 Temperature (°C)		Model set 3 Temperature (°C)		CP (mW)	
			M	P	M	P	M	P	M	P	M	P
5-74	285	100	34.8		48.6		38.9		41.1		234	
6-74	144	75		69.5		96.6		78.8		79.9		171
1/21/75	248	88		57.6		81		66.6		68.4		270
1/23/75	72	43	97.4								214	
2/27/75	88	30		40.5				99.6		98.1		90
$\bar{x}$			66.1	55.9	48.6	88.8	-	81.7		82.1		
s			44.3	14.6		11.0		16.7		15.0		
n			2	4		2		3		3		

TABLE XII: Threshold Data for Miscellaneous Exposures

Experimental Subject	Exposure Duration (seconds)	1/2-Power Radius (μm)	Experimental Temperature (°C)		Model set 1 Temperature (°C)		Model set 2 Temperature (°C)		Model set 3 Temperature (°C)		CP (mM)	
			M	P	M	P	M	P	M	P	M	P
10-74	.035	100	39.2		135.7		128.1		142.3		260	
3-74	.03	75		43		50.5		42.6		48.7		148
3-74	.02	75		46		59.0		49.6		52.4		191
8-74	.02	50		58		144.6		120.1		124.8		184
14-73	.02	40	47.2								105	
4-74	.04	80	29.2		44.2		36.8		40.6		113	
6-74	.04	75		63		104.7						123
12-73	.04	53	32.0		40.4		33.6		37.1		72	
14-73	.04	40	35.6		50.1		41.7		46.0		80.4	
11-73	.04	75	39.1		47.2		39.3		43.4		143	
9-73	.04	105		52.6		87.4						210
6-74	.05	75		57.6		99		88.4		97.4		116
2/27/75	.002	30		84		109						240

The comparisons of model and experimental threshold temperature rise versus exposure duration are summarized in Figures 18 and 19. In Figure 18, average macular experimental threshold temperature increases are compared with the solutions of the temperature model with parameter sets 1, 2, and 3. The model predicts the macular temperature within 30% at all times of exposure from .04 second to 10 seconds for parameters set 1. The percentage errors for .04 second, .1 second, 1 second and 10 second exposures using set 1 in the temperature model are +30%, -.34%, -9.5%, and -3%, respectively. The errors for exposure durations from .04 second to 10 seconds for model set 2 are +14% at .04 second, +1.4% at .1 second, +3.3% at 1 second and -8% at 10 seconds. Errors in the prediction of threshold temperature using the model with parameter set 3 are +2.7% at .04 second, +9% at .1 second, and +1% for 1 second and +3% at 10 seconds exposure duration.

In Figure 19, extramacular measured and predicted temperature increase for exposure durations from .01 second to 10 seconds are displayed. At .01 second, the model predicted temperature is 57% higher than the experimentally determined temperature increase. For a .1 second duration irradiation, the model predicts a temperature increase 25% higher than the measured rise. For exposure times of 1.0 second and 10 seconds, the model predicted temperatures with parameter set 1 are, respectively, 4.9% and 11.7% below the empirically determined temperature increases.

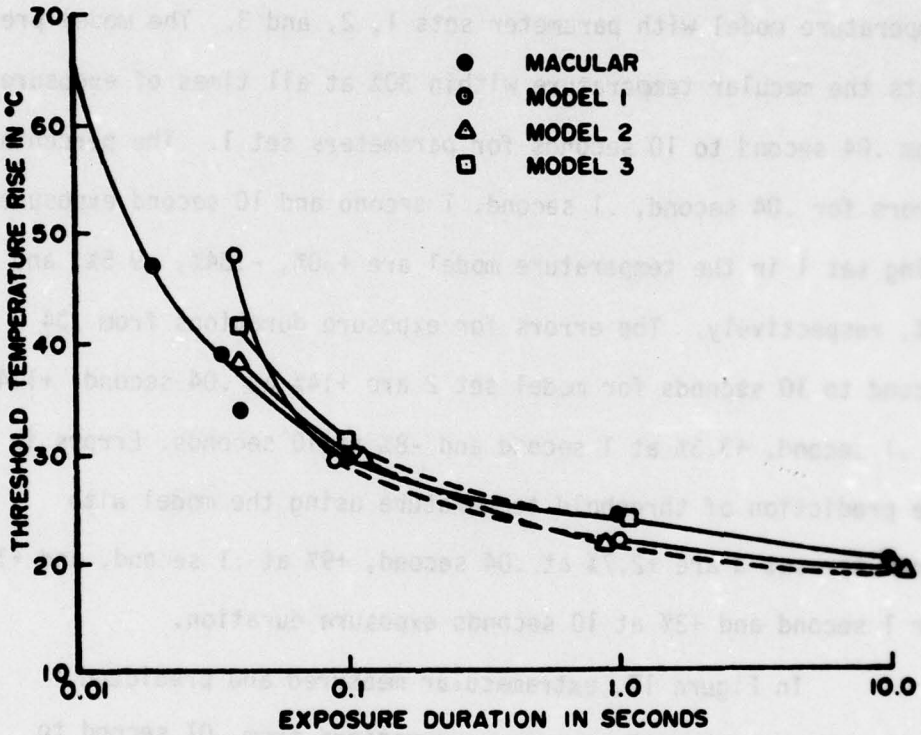

FIGURE 18: Comparison of temperature increases required for the production of macular lesions with calculated values from the conduction model with parameter sets 1, 2 and 3.

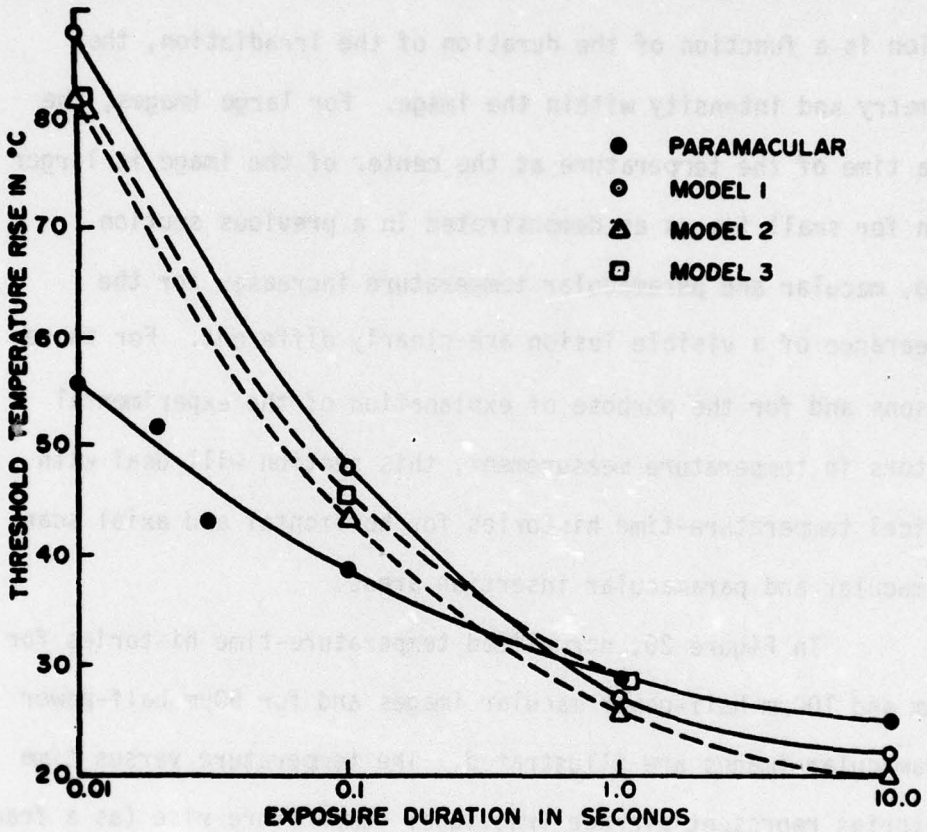

FIGURE 19: Comparison of experimental temperature increases required to produce visible lesions in the paramacula with computed values from the conduction model with parameter sets 1, 2 and 3.

Temperature-Time Histories

The temperature rise required to produce a visible lesion is a function of the duration of the irradiation, the geometry and intensity within the image. For large images, the rise time of the temperature at the center of the image is larger than for small images as demonstrated in a previous section. Also, macular and paramacular temperature increases for the appearance of a visible lesion are clearly different. For these reasons and for the purpose of explanation of the experimental factors in temperature measurement, this section will deal with typical temperature-time histories for horizontal and axial scans in macular and paramacular insertion areas.

In Figure 20, normalized temperature-time histories for 50μm and 100μm half-power macular images and for 50μm half-power paramacular images are illustrated. The temperature versus time histories represent average fractional temperature rise (as a fraction of the maximum temperature achieved) versus time for a 10 second laser exposure duration. The average rise time to .632 of the 10 second temperature for a macular 50μm half-power radius is 77.6 milliseconds. The 100μm half-power macular images require an average of 176 milliseconds to reach .632 of the 10 second temperature increase. A 50μm half-power radius paramacular temperature increase requires a time of 228 milliseconds to reach .632 of the

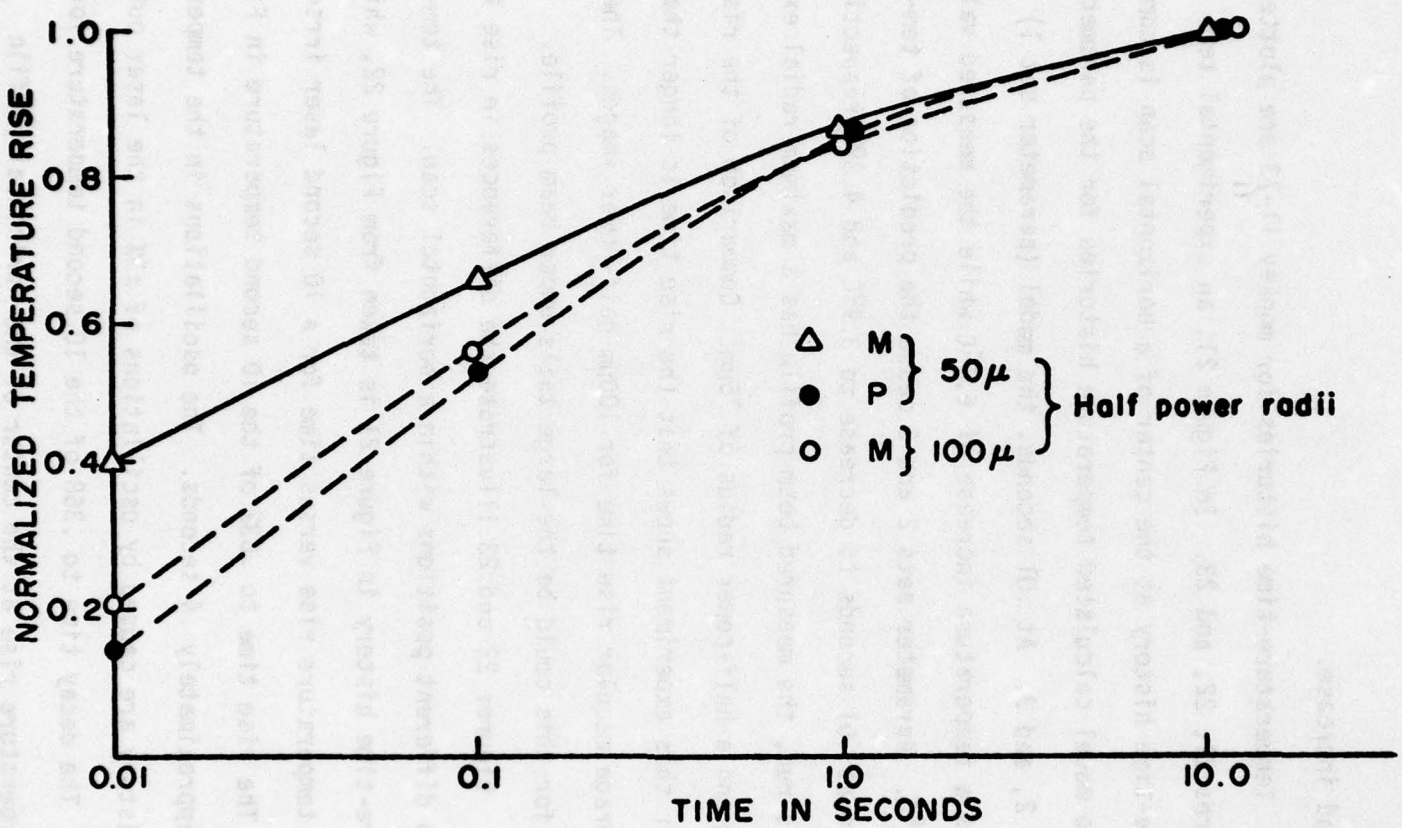

FIGURE 20: Average temperature-time histories for macular and paramacular insertion sites. Fractional temperature rise is plotted versus time during a 10 second exposure.

10 second increase.

Temperature-time histories for monkey 11-73 are plotted in Figures 21, 22, and 23. In Figure 21, an experimental temperature-time history at the center of a horizontal scan is compared to model calculated temperature histories for the parameter sets 1, 2, and 3. At .01 seconds, the model (parameter set 1) predicts a temperature increase of 6.1^{o}C while the measured value is 2.15^{o}C. Parameter sets 2 and 3 cause the prediction of temperature at .01 seconds to decrease to 3.9^{o}C and 4.3^{o}C respectively. For this run, the measured beam profile has a maximum radial extent or 40μm and a half-power radius of 75μm. Comparison of the rise time for this experiment shows that the rise time is longer than the average macular rise time for 100μm half-power images. The reason for this could be the large tails under beam profile.

Figures 22 and 23 illustrate the differences in rise time for two different positions within a horizontal scan. The temperature-time history in Figure 21 is taken from Figure 22, which is the temperature rise versus time for a 10 second laser irradiation. The rise time to .632 of the 10 second temperature in Figure 22 is approximately .4 seconds. The oscillations in the temperature time history are caused by oscillations of ±3% in the laser output power. The decay time to .368 of the 10 second temperature for the temperature rise at the center of the horizontal profile (Figure 22) is .42 second which is nearly the same as the rise time

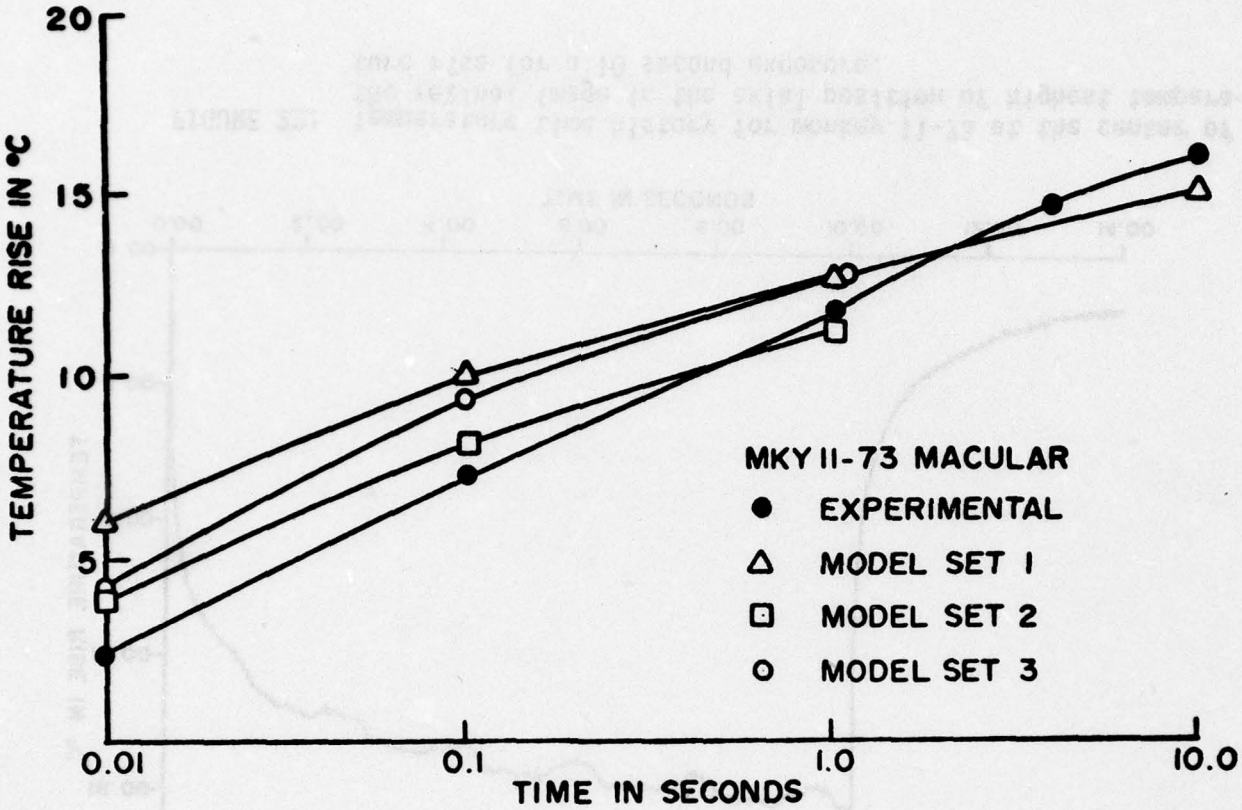

FIGURE 21: Experimental and model calculated temperature-time histories for monkey 11-73 for a 10 second exposure duration. Model calculations of temperature increase with three parameter sets are plotted with measured values.

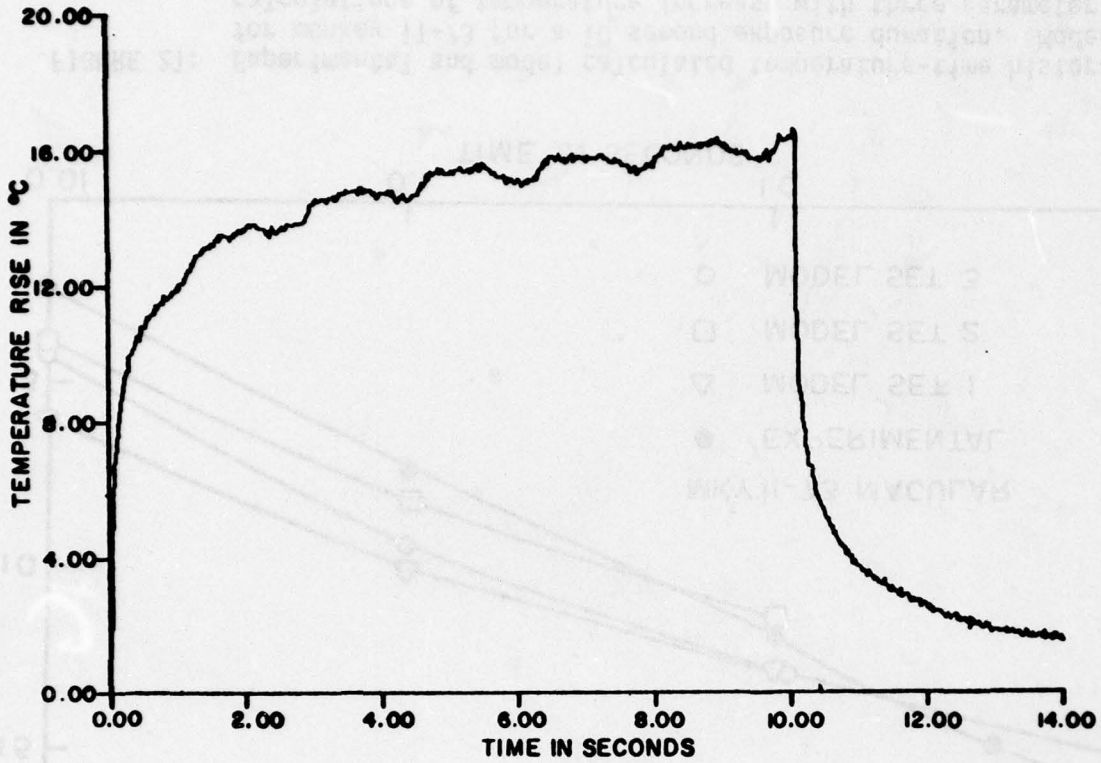

FIGURE 22: Temperature time history for monkey 11-73 at the center of the retinal image in the axial position of highest temperature rise for a 10 second exposure.

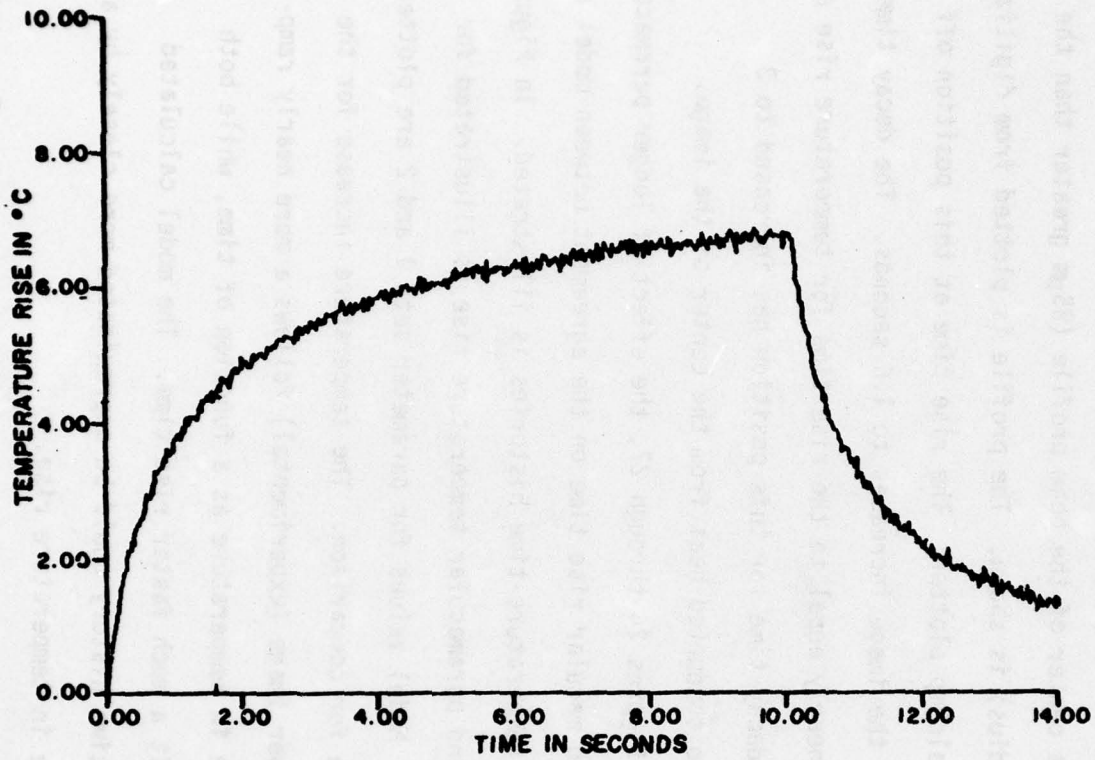

FIGURE 23: Temperature-time history for monkey 11-73 at a radial position 160μm from the center of the laser image and in the axial position of highest temperature rise for a 10 second exposure.

during the laser irradiation. The direct absorption for this run is not measurable above system noise.

In Figure 23, the temperature-time history for a position 160μm from the center of the beam profile (85μm greater than the half-power radius) is shown. The profile is plotted from digitized data on the Calcomp plotter. The rise time at this position off the center of the image increases to 1.6 seconds. The decay time is no longer nearly equal to the rise time for temperature rise off center. The decay time for this position has increased to 3 seconds due to conducted heat from the center of the image.

In Figures 24 through 27, the effect of longer paramacular rise time than macular rise time on the agreement between model and experimental temperature-time histories is illustrated. In Figure 24, a .1 second paramacular temperature rise is illustrated for monkey 8-74. Model values for parameter sets 1 and 2 are plotted on the figure for comparison. The temperature increase for the 50μm half-power image (experimental) follows a more nearly ramp-like increase in temperature as a function of time, while both models exhibit a much faster rise time. The model calculated temperature-time history could be approximated more closely by a step increase in temperature rise.

The variation in the rise time of temperature for positions ±200μm off the image center and at the center of the image are illustrated in Figures 25, 26, and 27. In Figures 25 and 27, the

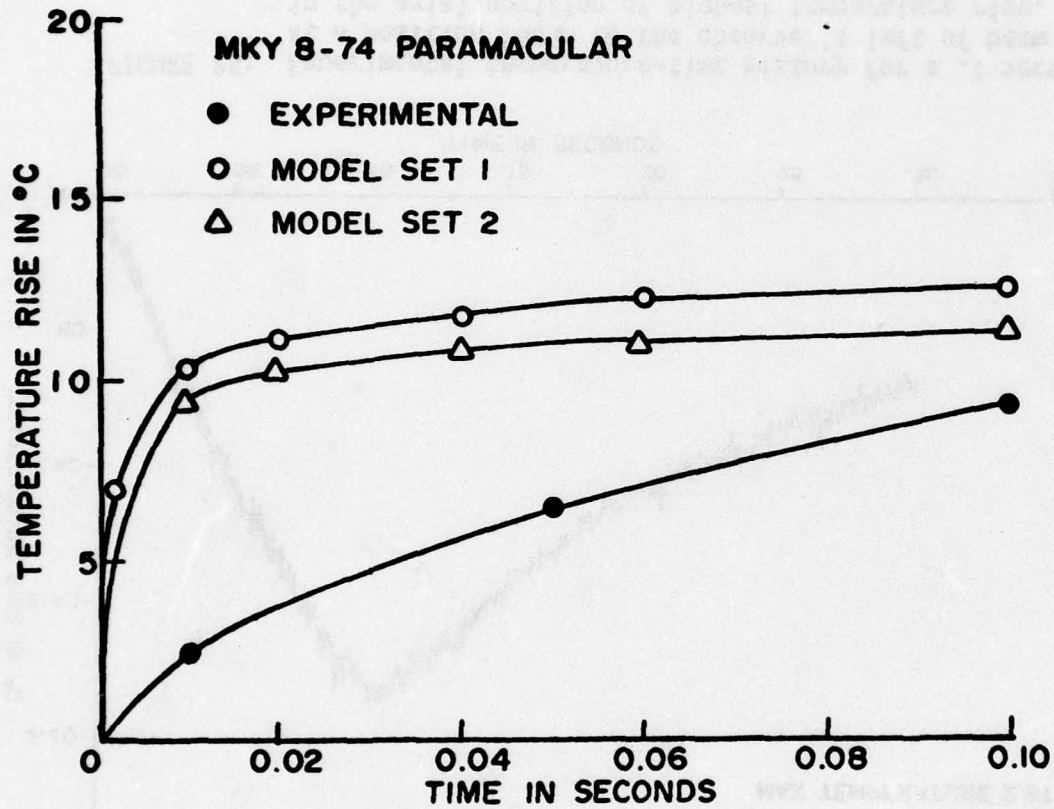

FIGURE 24: Experimental and model (parameter sets 1 and 2) temperature-time histories for monkey 8-74. Note that the time scale is linear.

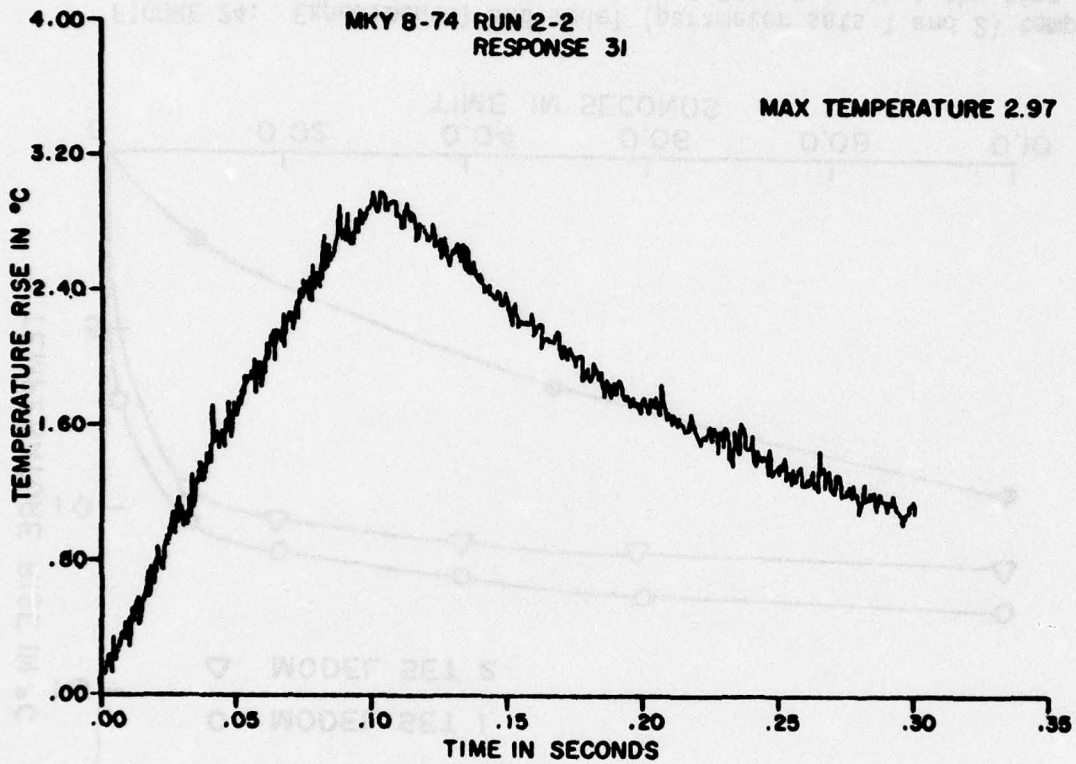

FIGURE 25: Experimental temperature-time history for a .1 second exposure at a position 200μm to the observer's left of beam center and in the axial position of highest temperature rise.

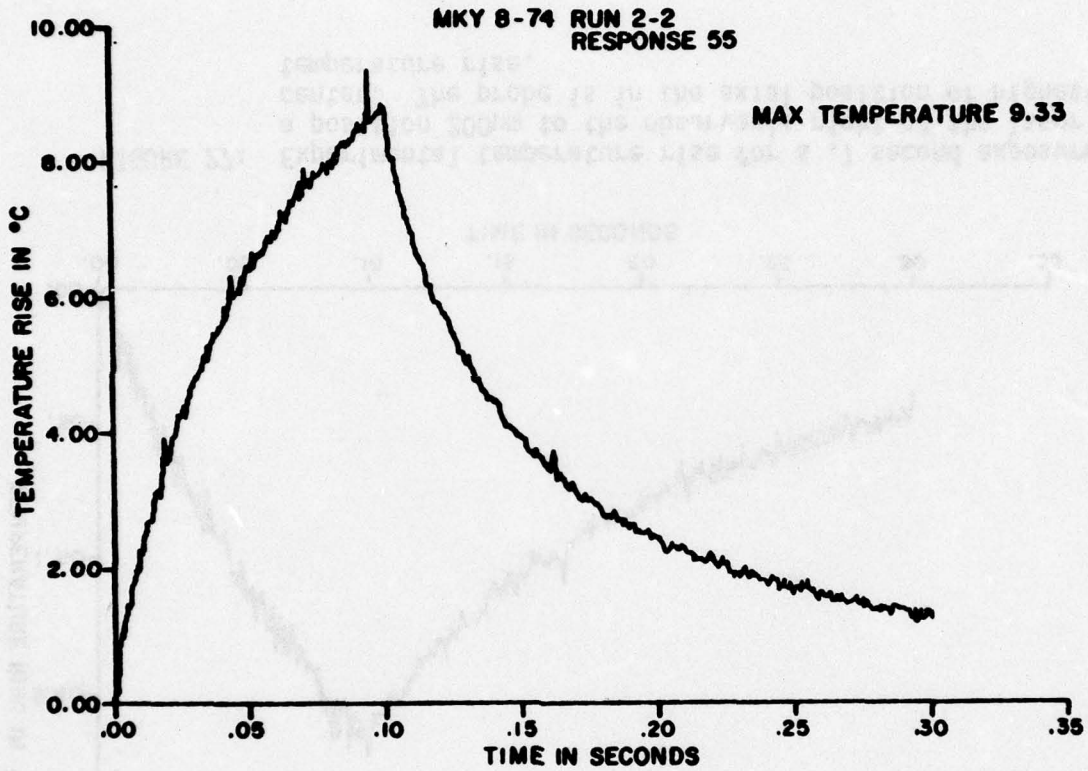

FIGURE 26: Experimental temperature-time history for a .1 second exposure. The probe is positioned in the center of the beam and at the axial position of highest temperature increase.

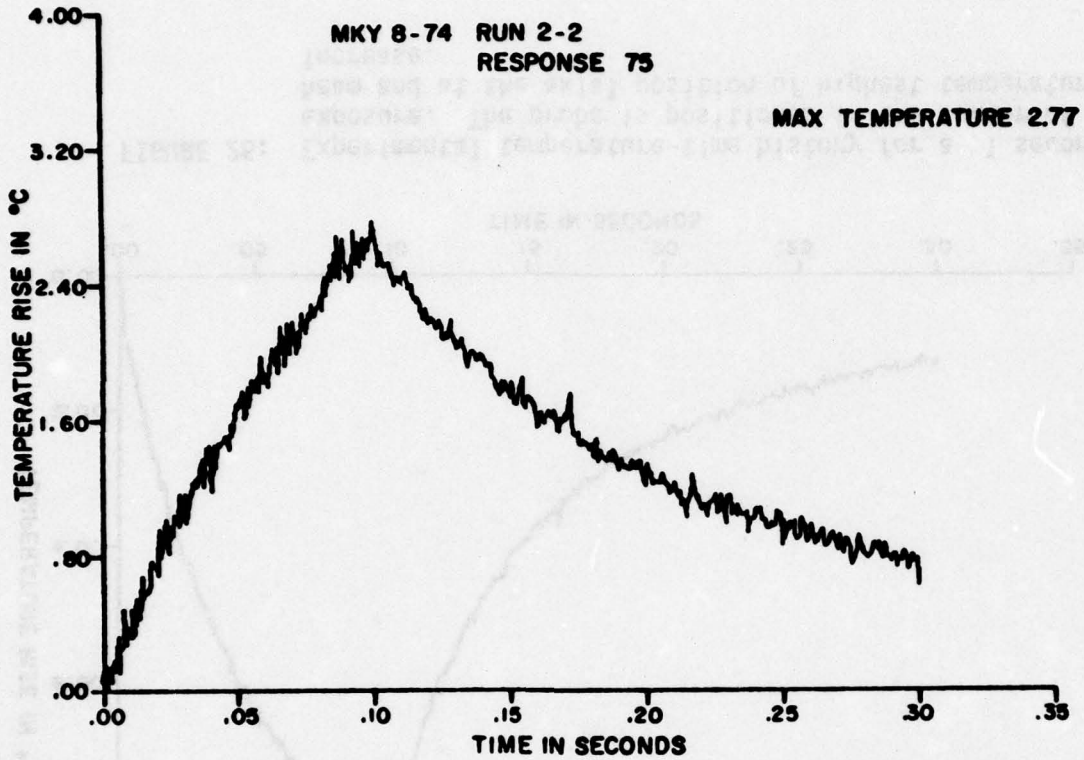

FIGURE 27: Experimental temperature rise for a .1 second exposure at a position 200μm to the observer's right of the laser image center. The probe is in the axial position of highest temperature rise.

temperature increase is nearly linear with time during the laser exposure. The maximum temperatures for these figures are 3.0°C and 2.8°C, respectively. At the center of the image, the rise of temperature is not as ramp-like as the increase 200μm off center. The maximum increase is 9.3°C. Near the center, the decay of the temperature is more rapid relative to the peak temperature than at two positions off center due to heat being conducted away from the center and toward the positions off the image center.

In Figure 28, model and experimental temperature rises for a 1 second exposure in the macula of monkey 4-74 are illustrated. Model predicted temperature increases for parameter sets 1 and 3 are shown in the figure with an experimental temperature rise at the center of a 237μm maximum radius image with a half-power radius of 80μm. The model and experimental values match closely for times during the exposure from .001 second to 1 second. The rise time (assuming the 1 second temperature is .87 times the 10 second temperature increase) is approximately 200 milliseconds which compares favorably with the rise time of 176 milliseconds for the "average" 100μm half-power image macula temperature-time history.

In the measurement of temperature increase and the location of the axial position of maximum temperature rise, the probe is withdrawn in small steps from the vitreous humor into the retina and to the pigment epithelium (theoretically the position of highest temperature). All of the temperature-time histories presented in this section were taken at the axial position of highest

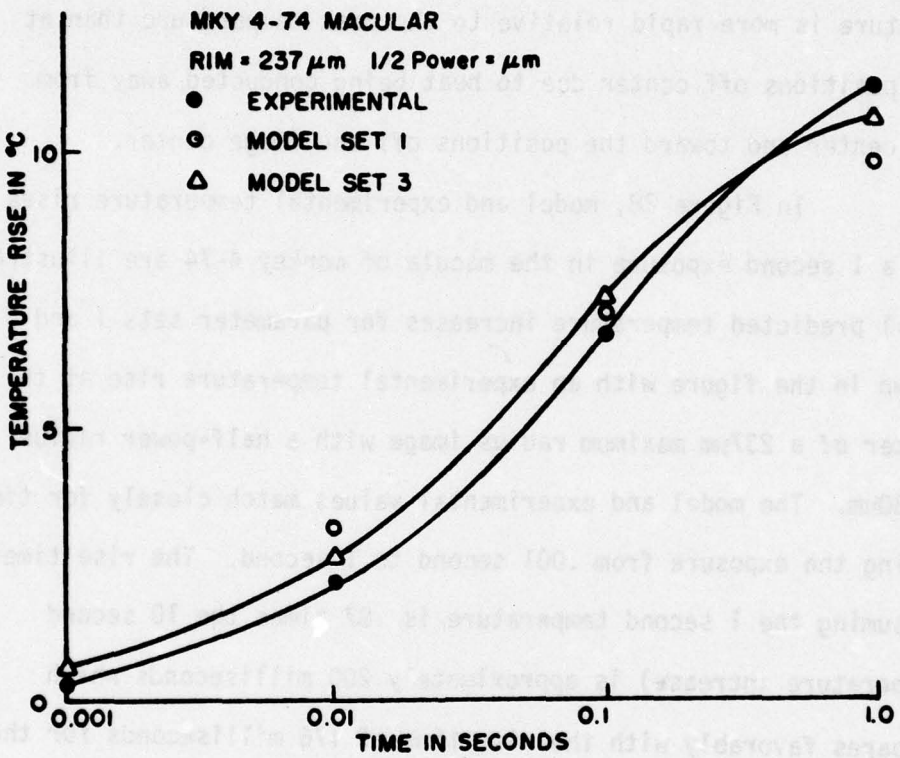

FIGURE 28: Temperature versus time for a 1 second exposure in the macula of monkey 4-74. The experimentally measured temperature rise is plotted for comparison with the calculated rise for model sets 1 and 3.

temperature rise. Generally, two components of temperature rise may be observed on the thermocouple output, direct absorption and temperature rise. For low power runs, however, the direct absorption component may be absent (lower than system noise).

In Figures 29 through 34, single temperature-time histories from an axial scan from moneky 8-74 are illustrated. The probe is first peaked horizontally, vertically and axially in the position of highest temperature. The thermocouple is then driven axially with the hydraulic drive on the micromanipulator, 360μm in front of the P.E. at an insertion angle of 10°. Withdrawal of the probe is accomplished in 10μm steps until the P.E. is reached and then in 5μm steps for the next 120μm. Ten micron steps are then taken for the remainder of the scan. In Figure 30 is a computer plot of the digitized data for a position 280μm in front of the P.E. A direct absorption component of $1.8^{o}C$ and a temperature rise of $.7^{o}C$, which may be a combination of tissue rise and conduction from the hot spot down the probe, is seen on the record. The pulse duration for the laser irradiation is .01 second.

A temperature rise and direct absorption record for a probe placement 80μm in front of the P.E. is shown in Figure 30. A direct absorption increase of $4.8^{o}C$ and a temperature rise due to conducted heat of $3.6^{o}C$ is present on the record. In Figure 31, a temperature-time history 10μm in front of the axial hot spot

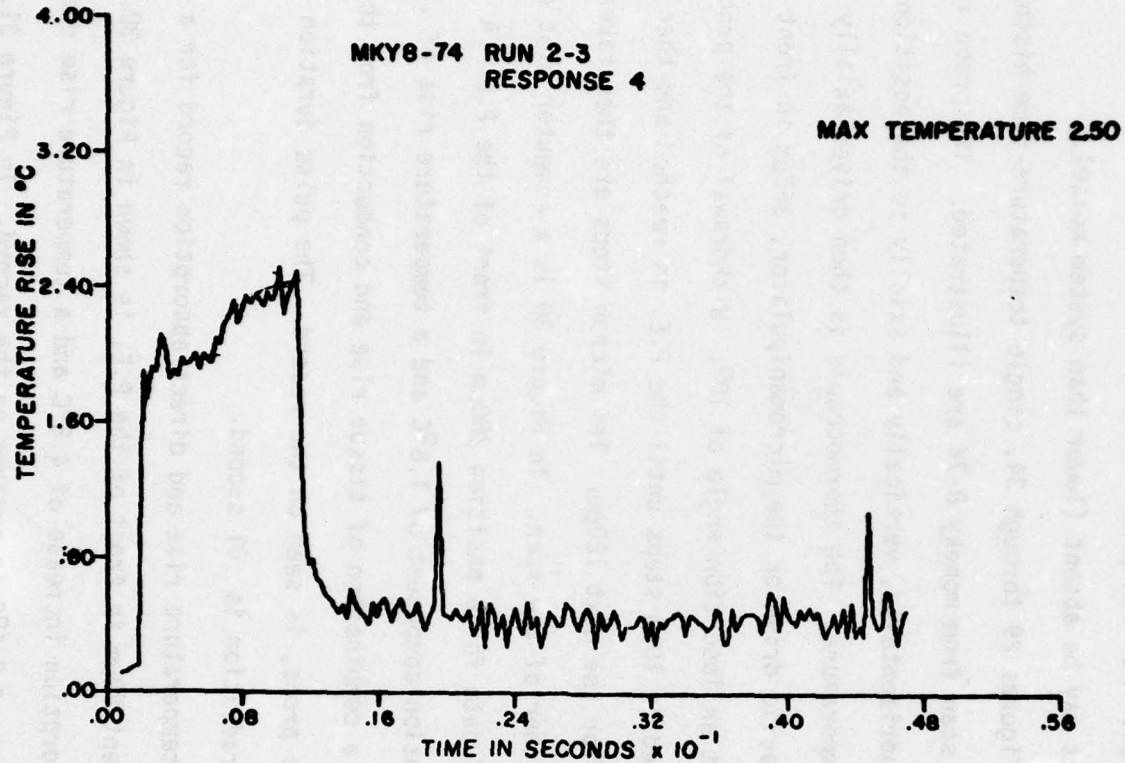

FIGURE 29: Temperature-time history for a .01 second exposure at a position 280μm in front of the P.E. The insertion angle is 10^{0} for this position in the axial scan.

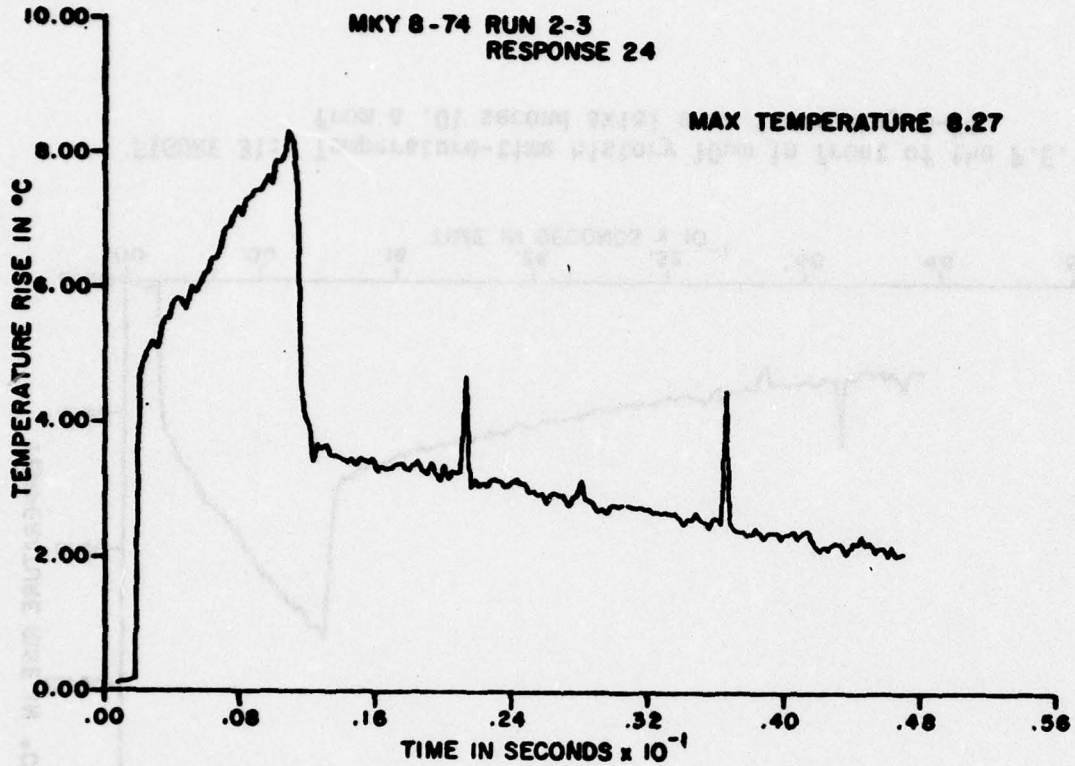

FIGURE 30: Temperature-time history for a probe placement 80μm in front of the P.E. The temperature is measured for an axial scan in monkey 8-74.

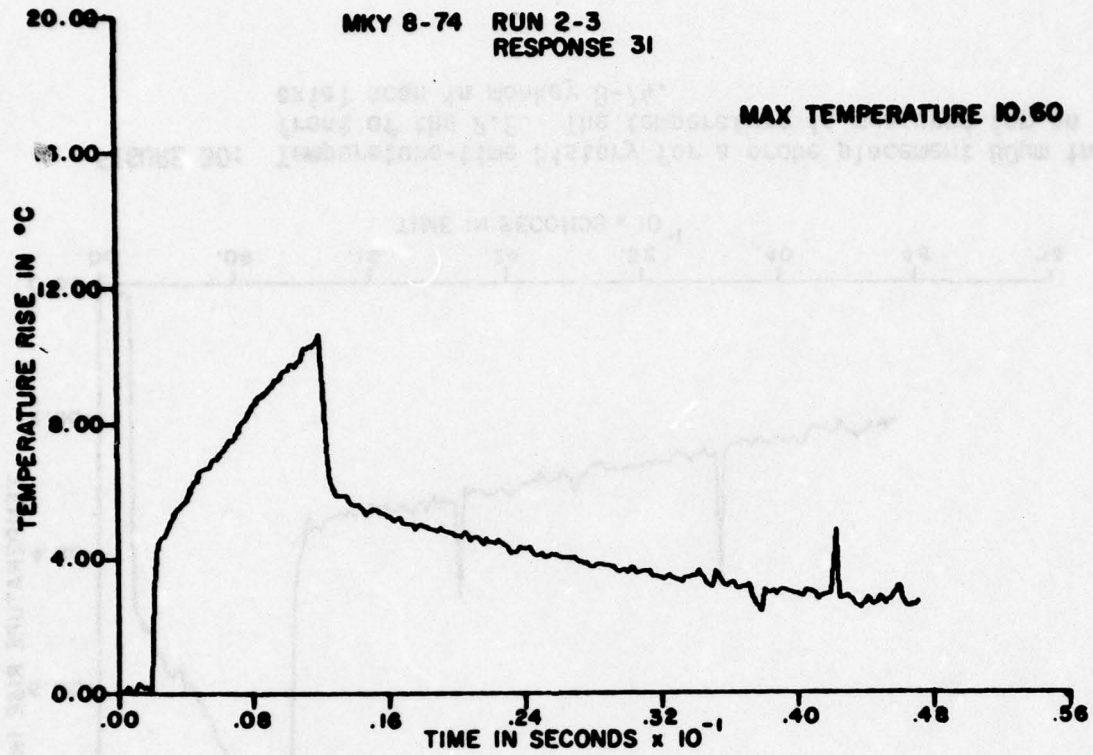

FIGURE 31: Temperature-time history 10μm in front of the P.E. from a .01 second axial scan for monkey 8-74.

indicates a direct absorption component of 4.7°C and a conduction component of 5.9°C. For the 10 millisecond exposure, in the hot spot, the conduction temperature rise has increased to 6.0°C and the direct absorption component is 4.6°C. Two other runs 20μm and 60μm behind the P.E. are shown in Figure 33 and 34. At the position 20μm behind the P.E., the direct absorption component is 3.5°C and the temperature increase due to conduction is 7.6°C. At the position 60μm behind the P.E., the direct component is 3.2°C and the temperature increase is 7.2°C.

Horizontal Temperature Scans

Horizontal temperature scans are performed by rotating the animal about a center of rotation near the nodal point of the eye. The effect of this rotation is to move the image past the thermocouple probe and to thus effect a measurement of temperature rise as a function of horizontal position for a given image distribution. Scans obtained in this manner are compared to temperature model solutions of the heat conduction equation.

In Figure 35, a horizontal (radial) scan for monkey 11-73 is illustrated. This scan is obtained for the same run that is shown in Figure 21 in the section on temperature-time histories. The retinal image distribution for this macular insertion has a maximum image radius of 400μm and a half-power radius of 75μm.

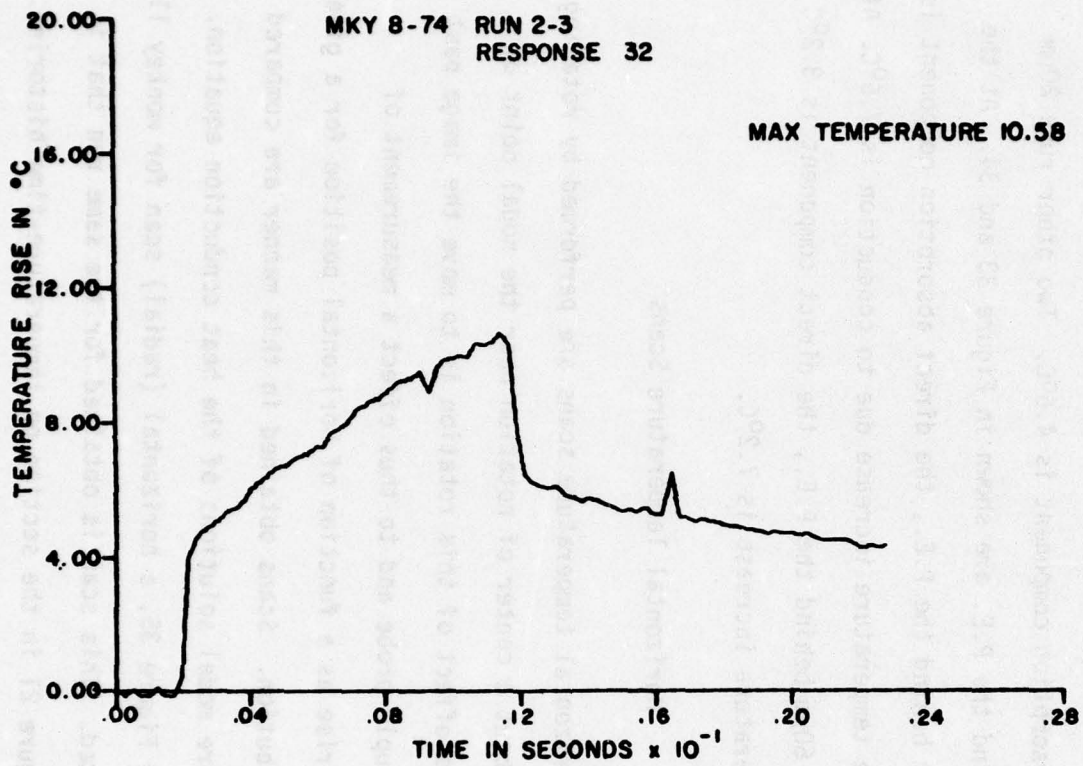

FIGURE 32: Temperature-time history in the P.E. for a .01 second axial scan at beam center.

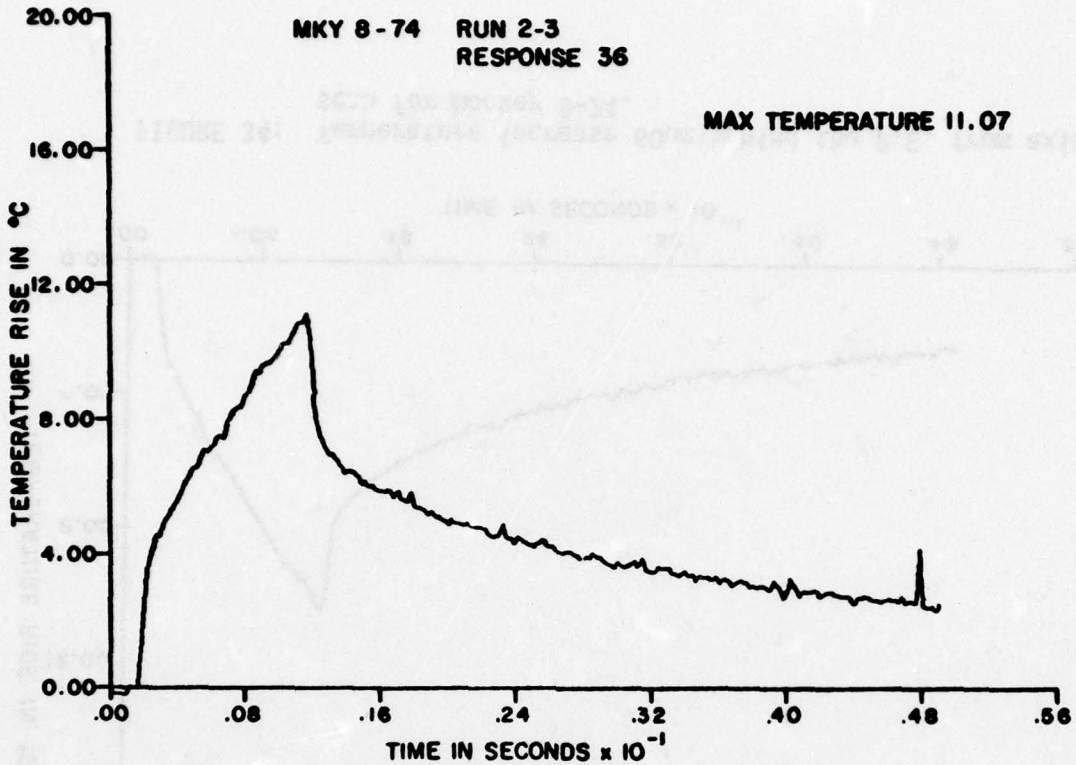

FIGURE 33: Temperature-time history 20μm behind the P.E. from the .01 second axial scan of monkey 8-74.

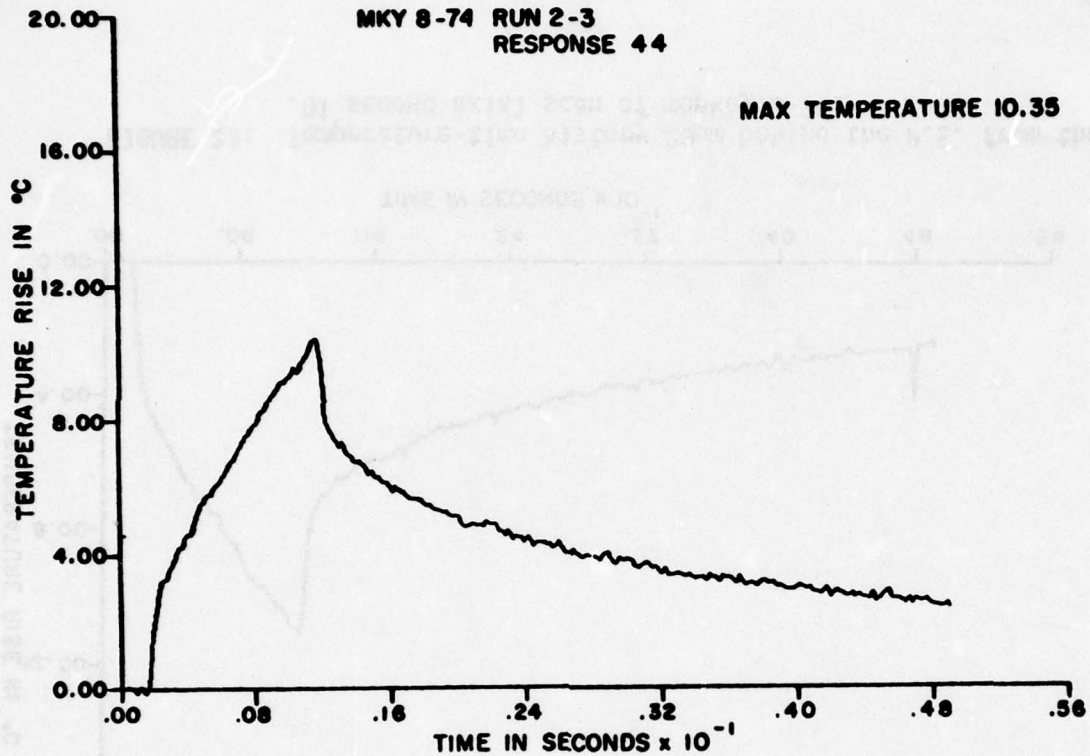

FIGURE 34: Temperature increase 60μm behind the P.E. from axial scan for monkey 8-74.

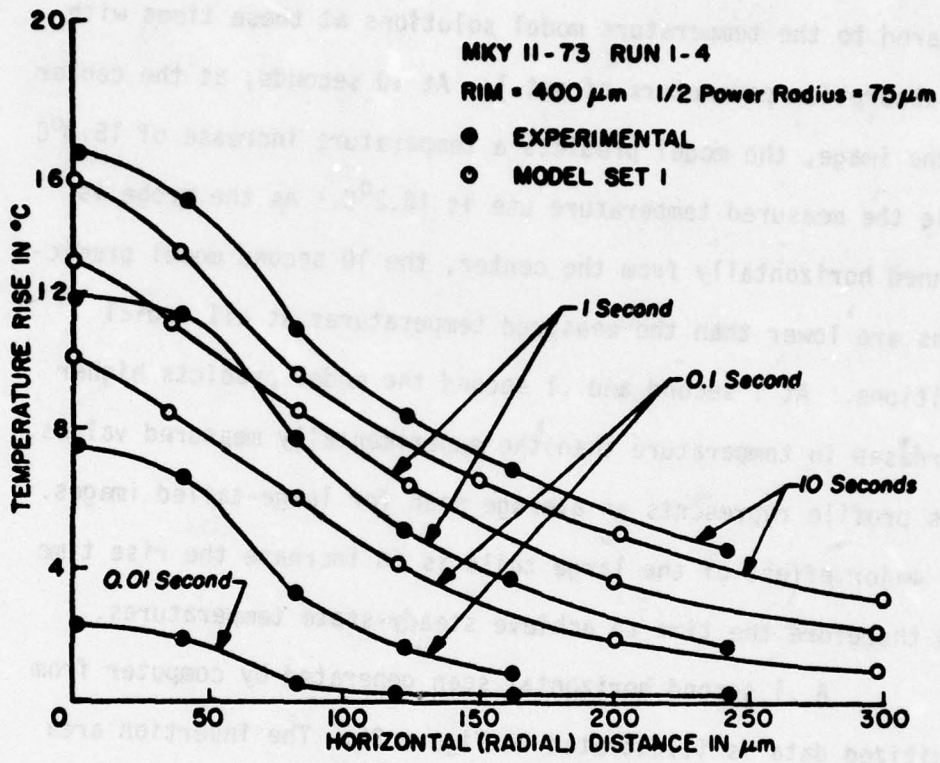

FIGURE 35: Horizontal scan for monkey 11-74 in the macula. The 10 second exposure duration scan is compared to the model solution with parameter set 1 at various times during the exposure.

A large amount of energy is therefore present in the tails of the distribution. Measured temperatures at times of .1 second, 1 second, and 10 seconds during a 10 second duration exposure are compared to the temperature model solutions at these times with the absorption parameters of set 1. At 10 seconds, at the center of the image, the model predicts a temperature increase of 15.3°C while the measured temperature use is 16.2°C. As the probe is scanned horizontally from the center, the 10 second model predictions are lower than the measured temperatures at all radial positions. At 1 second and .1 second the model predicts higher increases in temperature than the experimentally measured values. This profile represents an average scan for large-tailed images. The major effect of the large tails is to increase the rise time and therefore the time to achieve steady-state temperatures.

A .1 second horizontal scan generated by computer from digitized data is illustrated in Figure 36. The insertion area is extramacular temporal and superior to the macula approximately 2mm. The temperature-time history corresponding to this scan is in Figure 24. Temperature increases at times of .001 second, .01 second, .05 second and .1 second during a .1 second exposure are shown in Figure 37. The image for this run has a 152μm maximum radius and a half-power radius of 50μm. The slow rise, as evidenced by the small temperature rise at .01 second relative to the .1 second temperature increase, is typical of paramacular

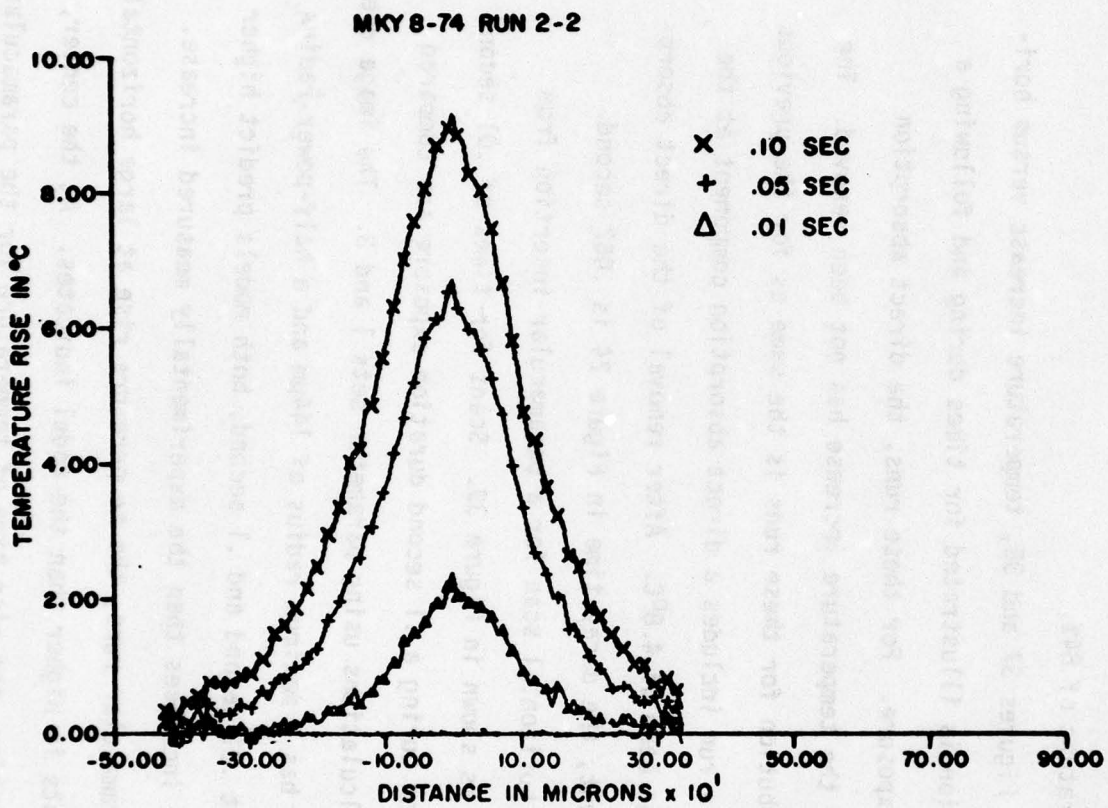

FIGURE 36: Experimental horizontal scan for a .1 second exposure in the paramacular region of the eye of monkey 8-74. Temperature increases at times of .01 second, .05 second and .01 second are plotted versus radial position.

insertions. At .01 second, at the center of the profile, the temperature is 26% of the .1 second temperature. The model with paramater set 2, predicts a ratio of the .01 second to the .1 second temperature of 84%.

In Figures 37 and 38, temperature increase versus horizontal position is illustrated for times during and following a .01 second exposure. For these runs, the direct absorption component of the temperature increase has not been removed. The image distribution for these runs is the same as for the previous figure. This run includes a direct absorption component at the center of the beam of 4.8^{o}C. After removal of the direct absorption component, the decay time in Figure 24 is .062 second.

A horizontal scan for a paramacular insertion from monkey 6-74 is shown in Figure 39. Scans for times of .01 second and .1 second during a .1 second duration exposure are compared to model calculations using parameter sets 1 and 3. The image used in this run has a maximum radius of 144μm and a half-power radius of 75μm. At .01 second and .1 second, both models predict higher temperature increases than the experimentally measured increase. In most paramacular runs, the temperature rise at large horizontal displacements is higher than the model indicates. At the center, as noted earlier, the rise time of temperature for the paramacular insertions is much longer than the model rise time.

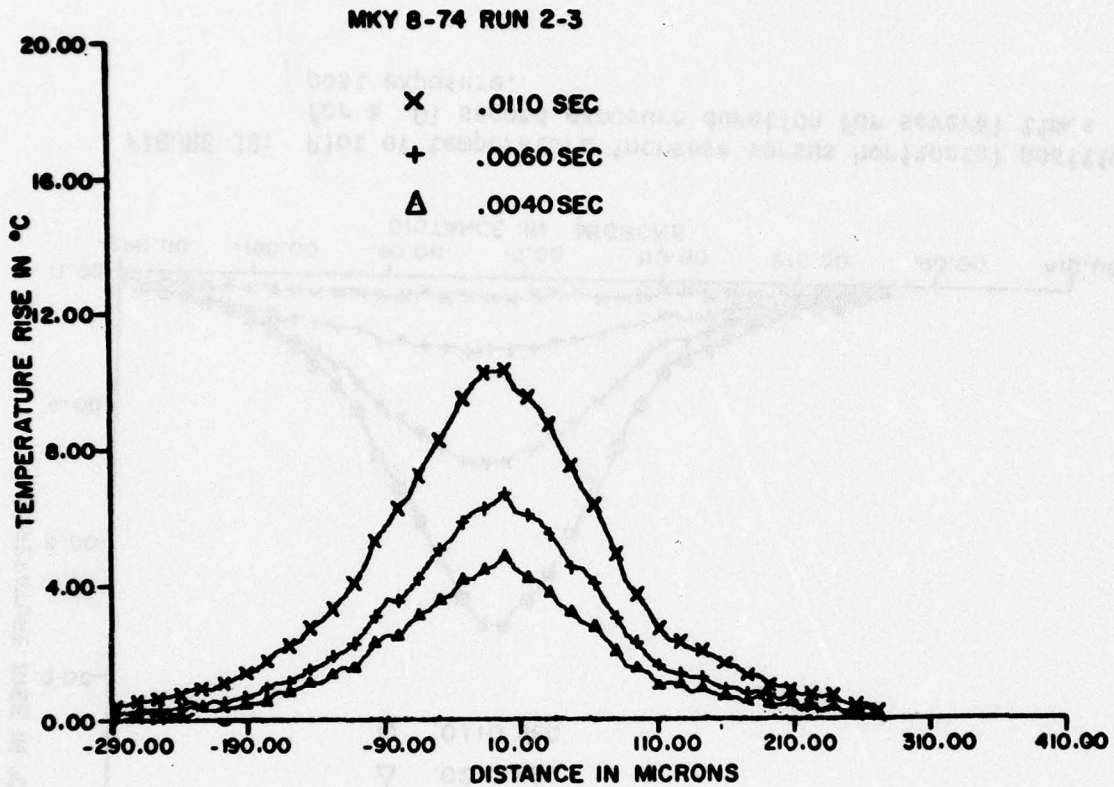

FIGURE 37: Experimental horizontal scan for a .01 second exposure for monkey 8-74 showing various times during the exposure.

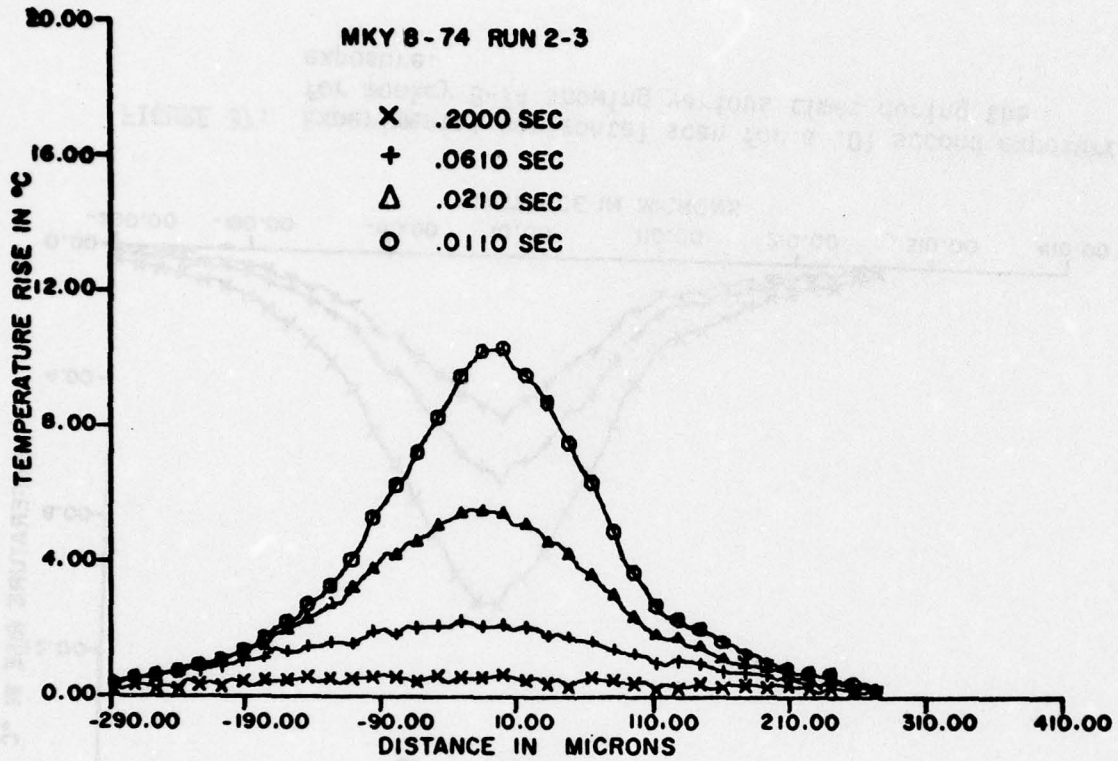

FIGURE 38: Plot of temperature increase versus horizontal position for a .01 second exposure duration for several times post exposure.

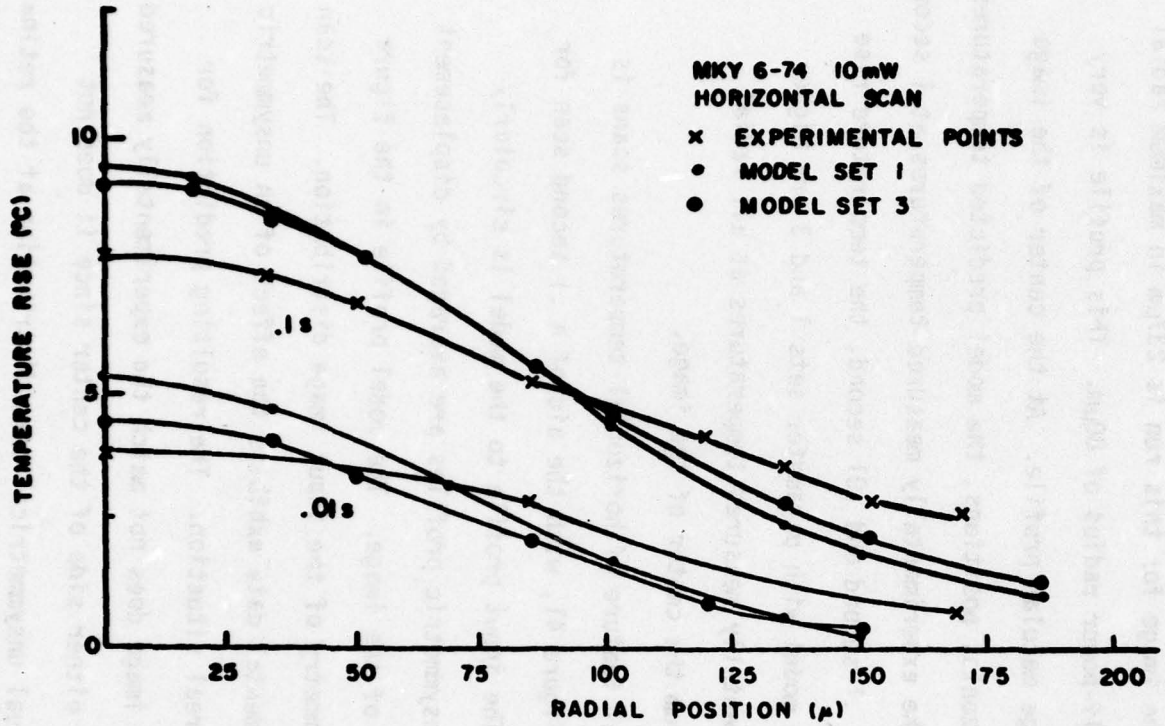

FIGURE 39: Horizontal experimental and model (sets 1 and 3) scans for a .1 second exposure comparing model and experimental values at .01 second and .1 second.

In Figure 40, a horizontal profile for monkey 4-74 is displayed. At times of .01 second, .1 second and 1.0 second, model set 1 and 3 are plotted for comparison with experimental measurements. The image for this run is 237μm in maximum radial extent with a half-power radius of 80μm. This profile is very nearly the average macular profile. At the center of the image and for all horizontal positions, the model predicted temperatures are lower than the experimentally measured temperatures at 1 second. For the times of .1 second and .01 second, the temperature rise predicted by the model with parameter sets 1 and 3 are higher than the experimentally measured temperatures at all radial displacements from the center of the image.

A final feature of horizontal temperatures scans is illustrated in Figure 41, with the aid of a .1 second scan for monkey 10-74. The input profile to the model is circularly symmetric, so unsymmetric profiles are averaged by displacement from the center of the image. The model profile in the figure reflects the symmetry of the input image distribution. The scan from the experimental data exhibits the effect of an unsymmetric profile in the real situation. The resulting prediction for the "idealized" image does not match the experimentally measured temperatures on either side of the center since it does not utilize the actual unsymmetrical beam distribution at the retina.

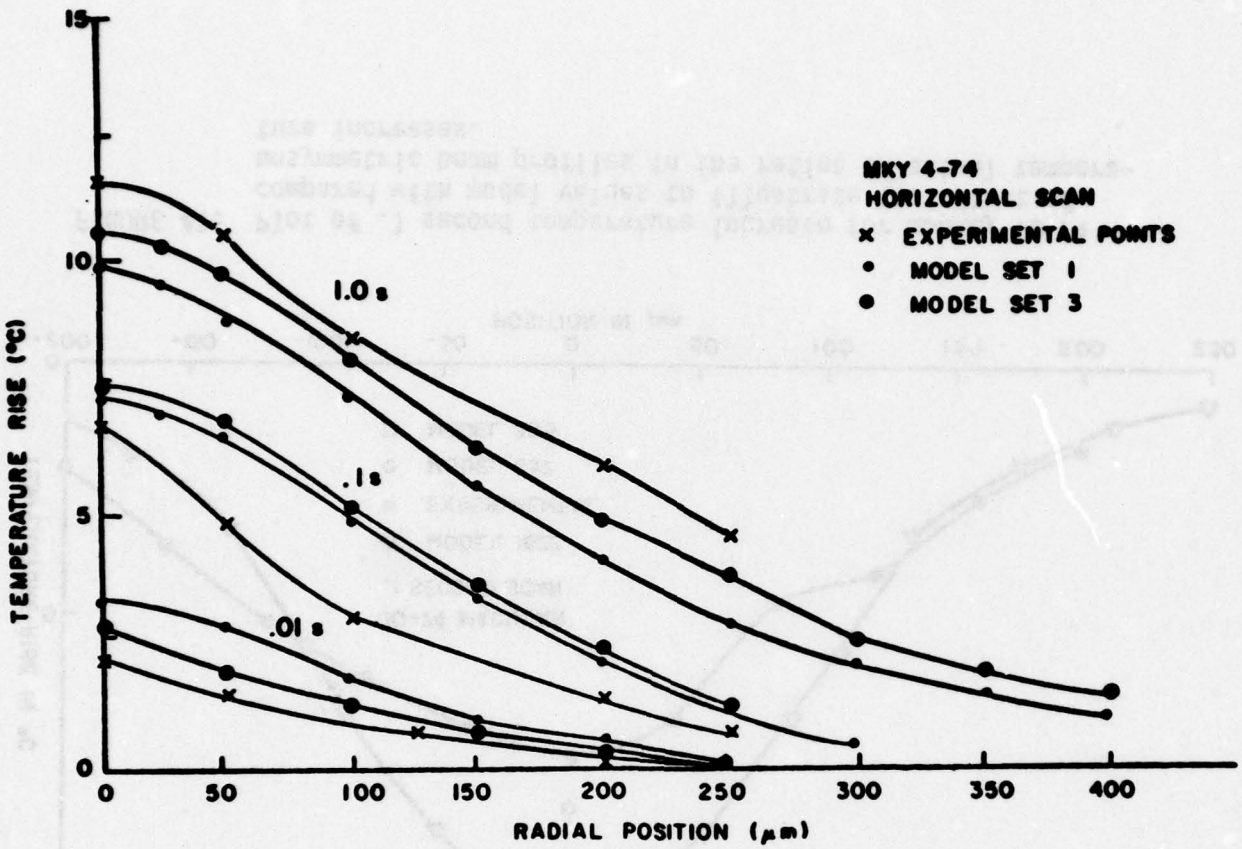

FIGURE 40: Horizontal experimental and model temperature scan for a 1 second exposure. Model sets 1 and 3 are compared to the experimentally measured profile at .01 second, .1 second, and 1.0 second.

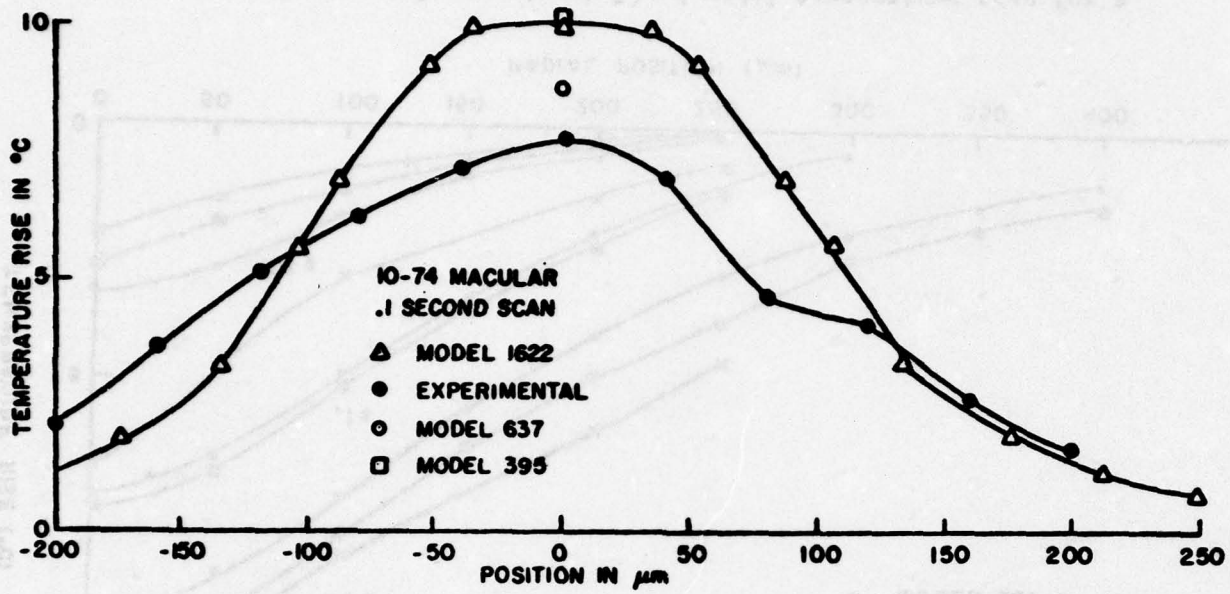

FIGURE 41: Plot of .1 second temperature increase for monkey 10-74 compared with model values to illustrate the effect of unsymmetric beam profiles in the retina on actual temperature increases.

Axial Temperature Scans

Axial temperature scans indicate the temperature as a function of position in the various layers and fluids of the eye. Axial scans start in the vitreous, progress through the neural retina, through the P.E. and then into the choroid. In the layers and fluids in front of the P.E., the temperature rise recorded by the thermocouple is due to direct absorption of light energy in the metal films of the thermocouple and a conducted component which is a combination of heat conduction down the probe from the hot spot and tissue temperature rise due to conducted heat. The direct absorption component is used to determine absorption profiles in the tissue and the temperature rise component is compared to the model predicted temperature rise for each scan.

An axial scan from 360μm in front of the P.E. to 300μm behind the P.E. for monkey 8-74 is shown in Figure 42. The scan is taken in 10μm steps from 360μm in front of the P.E. to the front of the P.E., then in 5μm steps from 0 to 120μm behind the P.E.. From 120μm to 300μm behind the P.E., the scan is again taken in 10μm axial steps. The probe track angle for this experiment is approximately 10°. At a position 360μm in front of the P.E., the rise in temperature is almost all direct absorption as evidenced by the .003 second and .01 second

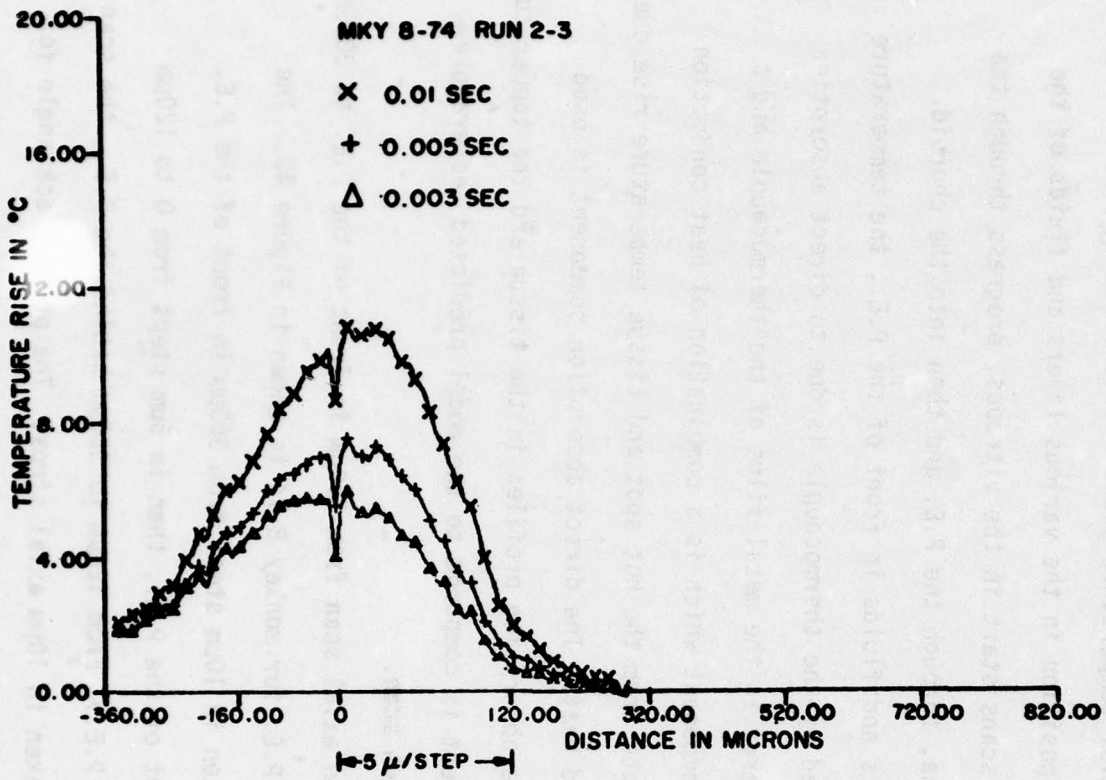

FIGURE 42: Axial temperature scan for monkey 8-74 for a .01 second exposure duration. Note the expanded scale from a position of 0μm to 120μm from the front of the P.E.

temperatures being nearly equal. The initial direct absorption temperature rise is 1.9°C. As the probe is withdrawn toward the P.E., the direct absorption component increase due to the angle of insertion. At the P.E., the direct absorption rise is 4.9°C. If the direct absorption component is corrected by the angle of the insertion and the beam profile values, the direct absorption rise at the -360μm position is nearly equal to the direct absorption at the P.E. The direct absorption component drops off rapidly as the thermocouple is withdrawn behind the P.E. The temperature rise reaches a peak approximately 20μm behind the P.E.

The temperature increase as a function of depth behind the P.E. is plotted in Figure 43. This temperature increase is compared to solutions of the temperature model using parameter sets 1 and 3. The temperature increase is derived from Figure 43 by subtracting the direct absorption component at each axial position from the total temperature rise. The exposure time for this scan is .01 second. Both the model predicted scan for parameter set 3 and the experimental profile peak approximately 20μm behind the front of the P.E. The model using parameter set 1, however, predicts a peak temperature near the center of the P.E.

From Figure 42, the direct absorption versus depth in the axial direction relative to the front of the P.E. is plotted in Figure 44. Two other profiles from monkey 4-74 and monkey 9-74 are also plotted on the figure. The scan from monkey 8-74

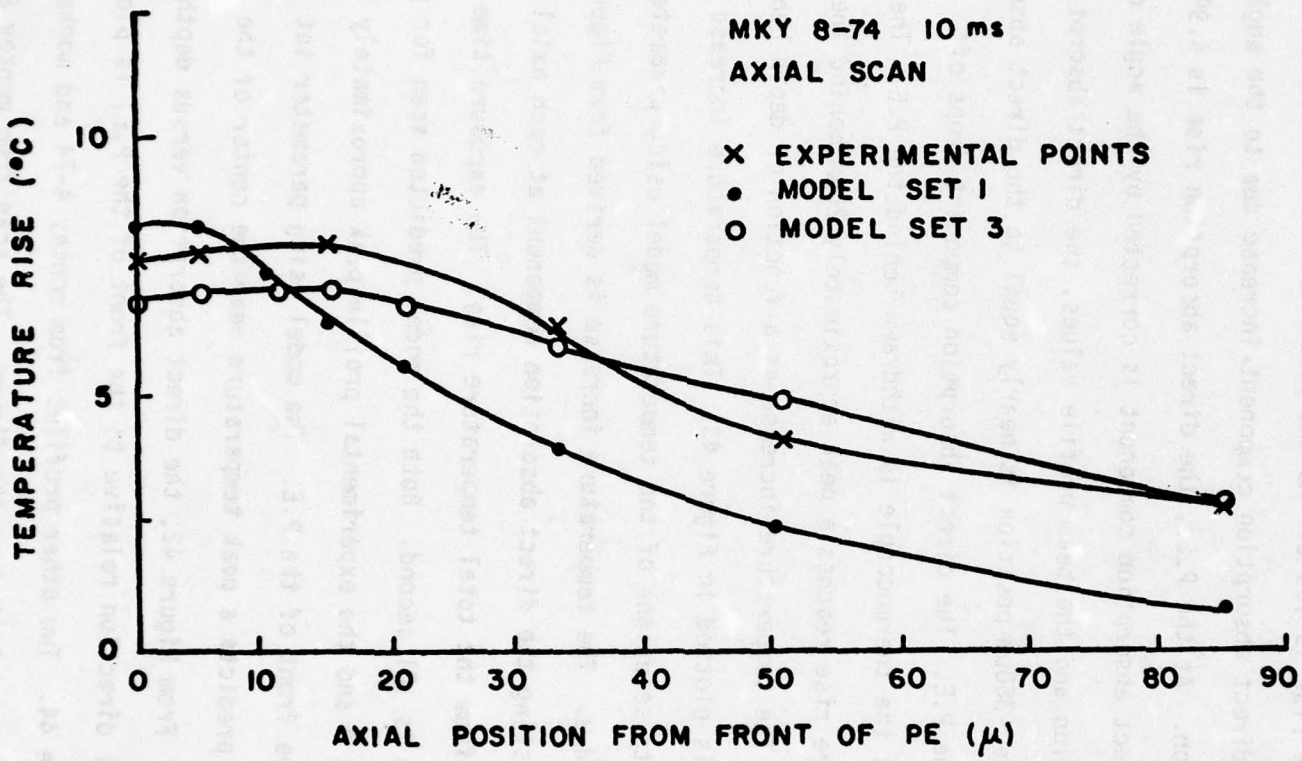

FIGURE 43: *Axial temperature scan for a .01 second expsoure for monkey 8-74. Experimental values are plotted with calculated temperature increases for model sets 1 and 3.*

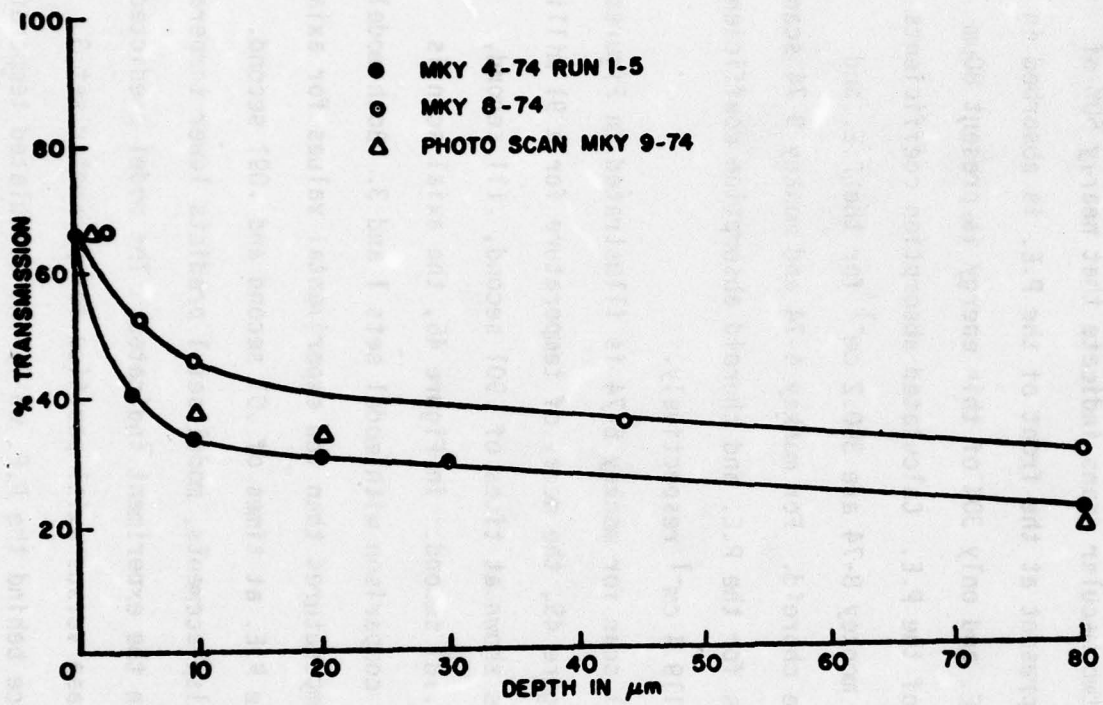

FIGURE 44: Plot of direct absorption as a function of depth from the front of the P.E. for three experiments. The scans from monkey 4-74 and 9-74 are for macular insertions.

is a paramacular insertion while the other two profiles are for macular insertion sites. The profile from monkey 8-74 shows an absorption of 32% of the light reaching the P.E. in that layer and almost half this light is still present 80μm behind the front of the P.E. The two macular scans indicate that nearly 50% of the light energy present at the front of the P.E. is absorbed in the 10μm thick P.E. and only 30% of this energy is present 80μm behind the front of the P.E. Calculated absorption coefficients from the scan for monkey 8-74 are 390.2 cm^{-1} for the P.E. and 102.6 cm^{-1} for the choroid. For monkey 4-74 and monkey 9-74 scans, the average values for the P.E. and choroid absorption coefficients are 648 cm^{-1} and 119.4 cm^{-1} respectively.

An axial scan for monkey 6-74 is illustrated in Figures 45 and 46. In Figure 45, the decay of temperature for a 91 millisecond exposure is shown at times of .901 second, .111 second, .141 second, and .181 second. In Figure 46, the axial scan is plotted again for comparison with model sets 1 and 3. Both models predict higher temperatures than the experimental values for axial positions near the P.E. at times of .01 second and .091 second. For large axial displacements, model set 1 predicts lower temperature increase than the experiment indicates. The model predicted temperature increase versus axial position for parameter set 3 peaks some distance behind the P.E. while the calculated temperature for set 1 peaks near the center of the P.E.

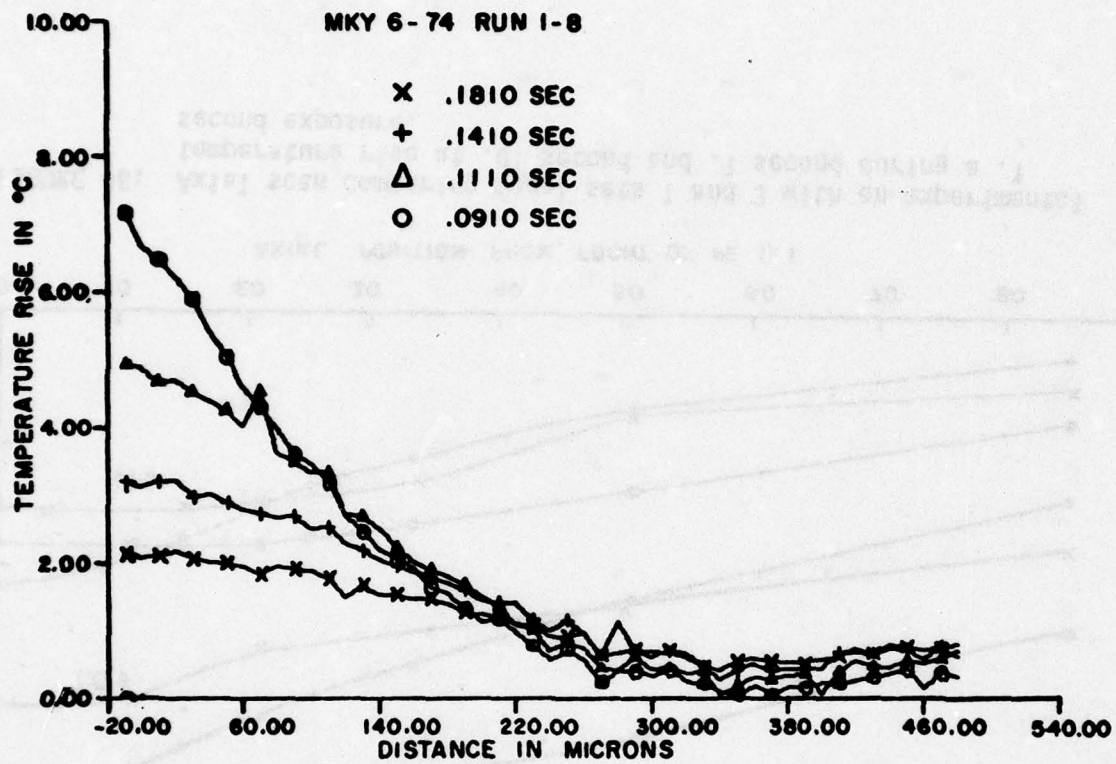

FIGURE 45: Experimental axial scan for monkey 6-74 from the pigment epithelium into the sclera. Several times following the .091 second exposure are plotted versus distance from the P.E.

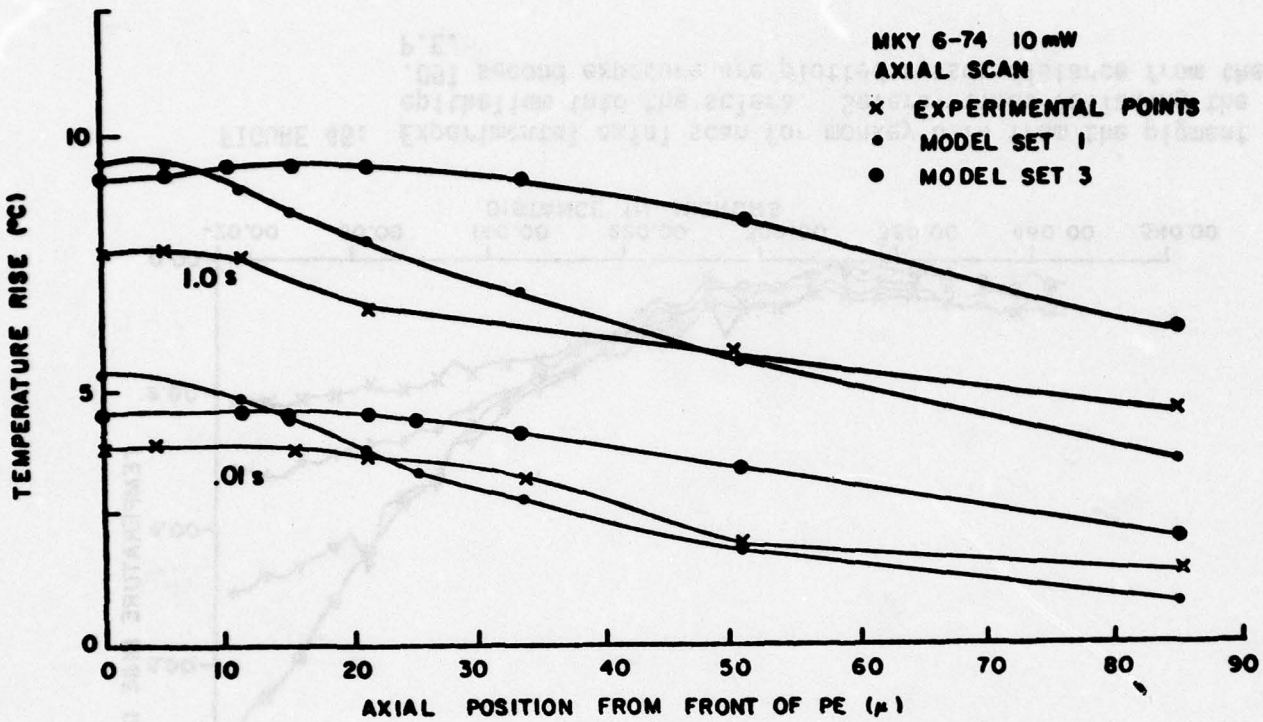

FIGURE 46: Axial scan comparing model sets 1 and 3 with an experimental temperature rise at .01 second and .1 second during a .1 second exposure.

Comparison with Published Thresholds

The data obtained in this study are grouped by half-power radii for comparison with the thresholds published by other investigators. Most of the published data for the argon wavelengths are for minimal image sizes. Therefore, the larger images used in this study should require higher power for lesion production.

Threshold corneal powers required to produce a macular threshold lesion in this study are compared to data from Gibbons (15) and Clarke (1) in Figure 47. The data of Gibbons and Clarke are for one hour threshold criteria, while the exposures in this study are for threshold lesion appearance 5 minutes post exposure. Also, Gibbon's and Clarke's data are for minimal images versus the 180μm and 280μm image radius exposures in these experiments. For large images, the corneal power required to produce a lesion is higher, as would be expected, than that required to produce a lesion for minimal image sizes. The shorter time criterion for these experiments (5 minutes) should also contribute to higher corneal power for lesion appearance than the one hour criterion.

In Figure 48, the threshold corneal powers required for lesions for extramacular exposures are compared to the values from Vassiliadis (6) and Clarke (1). Both 15μm and 100μm images from Vassiliadis data are shown in the figure with data for 180μm and 280μm image radii.

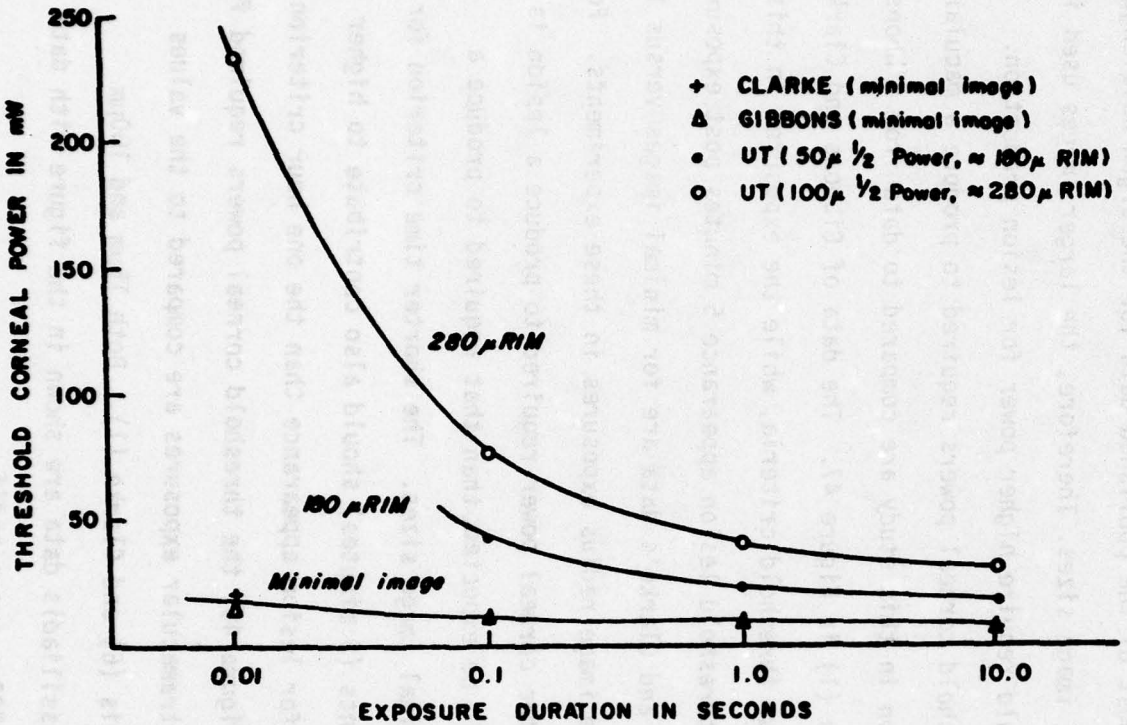

FIGURE 47: Comparison of experimental data (UT) for 180μm and 280μm radius images with the minimal image data of Clarke (1) and Gibbons (15) for macular exposures.

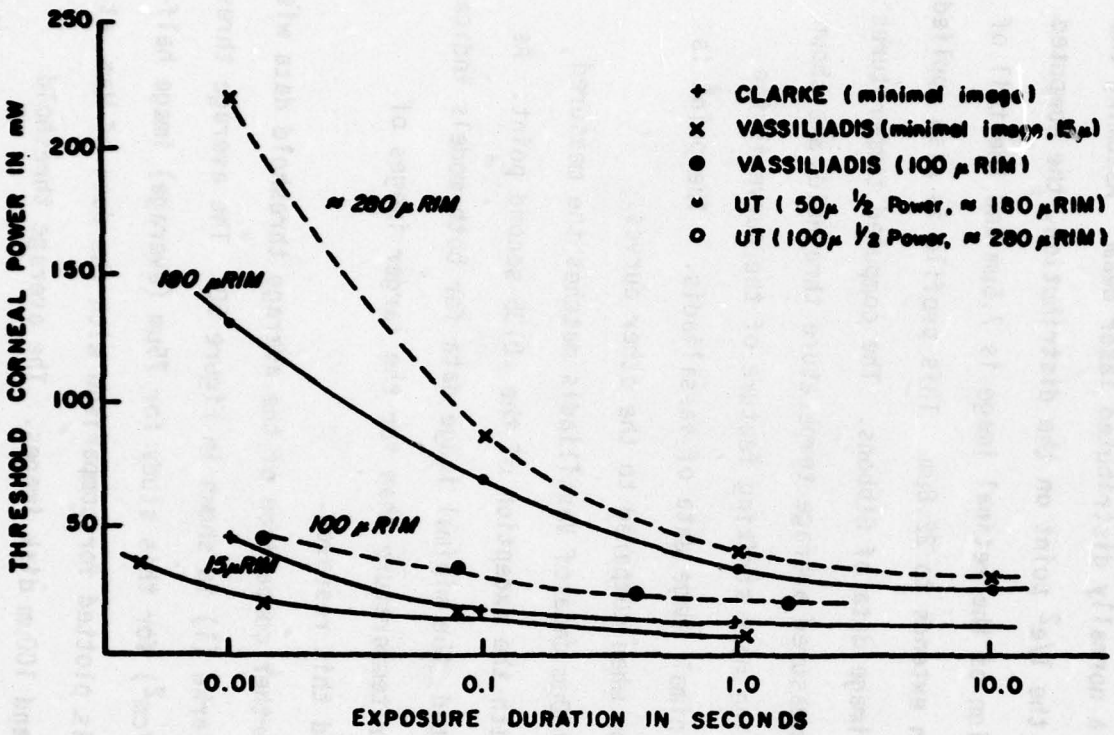

FIGURE 48: Comparison of experimental data (UT) for paramacular exposures with the data of Vassiliadis (6) and Clarke (1). Threshold data for images with 180μm and 280μm maximum radii are compared to the data of the other investigators for minimal and 100μm images.

For comparison, the center temperature that would be produced by the threshold powers reported by Gibbons (15) and Vassiliadis (6) is calculated. First, it is necessary to assume a retinal profile. Vassiliadis reports an image radius of approximately 15μm and a normally distributed laser beam. Assuming the 15μm represents the $1/e^2$ point on the distribution, the computed standard deviation of the retinal image is 7.5μm and the tail of the distribution extends to 22.8μm. This profile is also applied to the minimal image data of Gibbons. The computed temperatures along with the measured average temperature thresholds are shown in Figure 49. The most striking feature of the curve is the .0135 second minimal image data of Vassiliadis. The point is unexpectedly low when compared to the other curves.

The 100μm data of Vassiliadis matches the measured temperatures with the exception of the .0135 second point. As might be expected, the minimal image data for both models indicate a higher center temperature than for the larger images of Vassiliadis and this research.

A further comparison of the average threshold data with the data of Clarke (1) is shown in Figure 50. The average threshold irradiance (w/cm^2) for this study for 75μm (average) image half-power radius is plotted for comparison with the data of Ham et al. (5) for 10μm and 100μm disk images. The average threshold irradiance is calculated from the model with a transmission of the

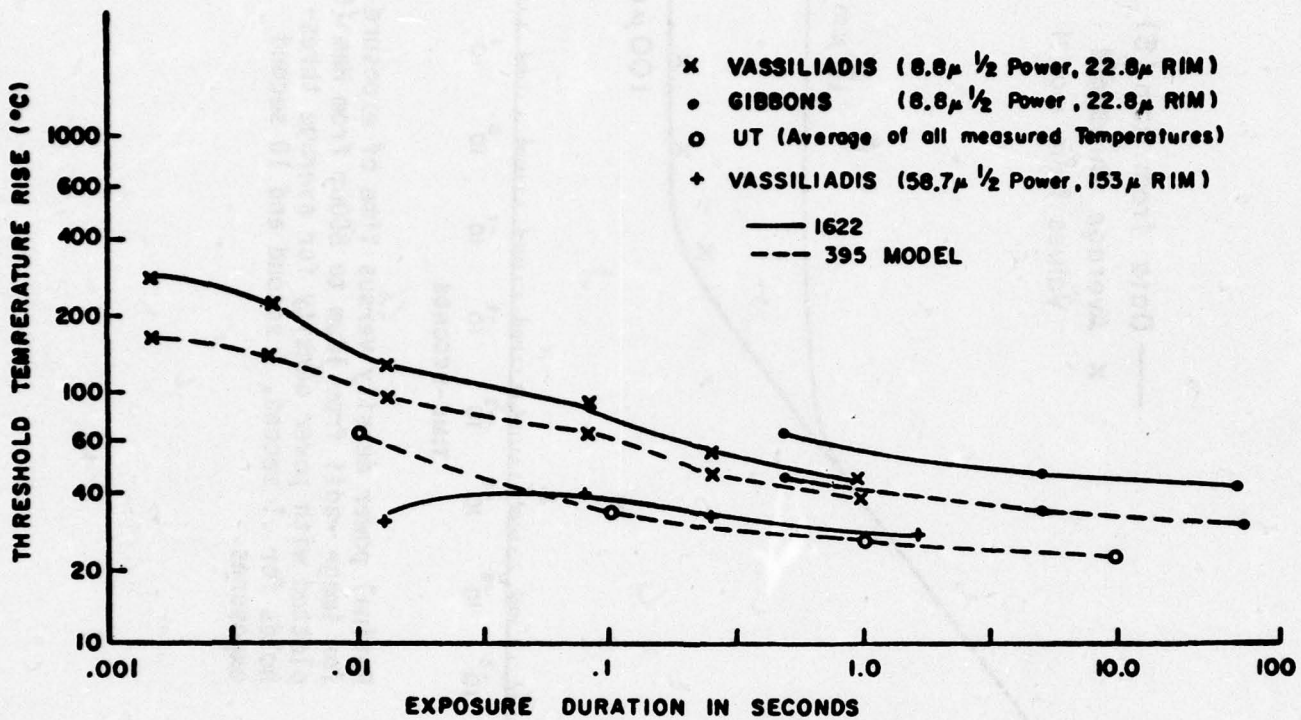

FIGURE 49: Comparison of measured temperatures with calculated temperatures for the threshold corneal powers from the data of Vassiliadis (6) and Gibbons (15).

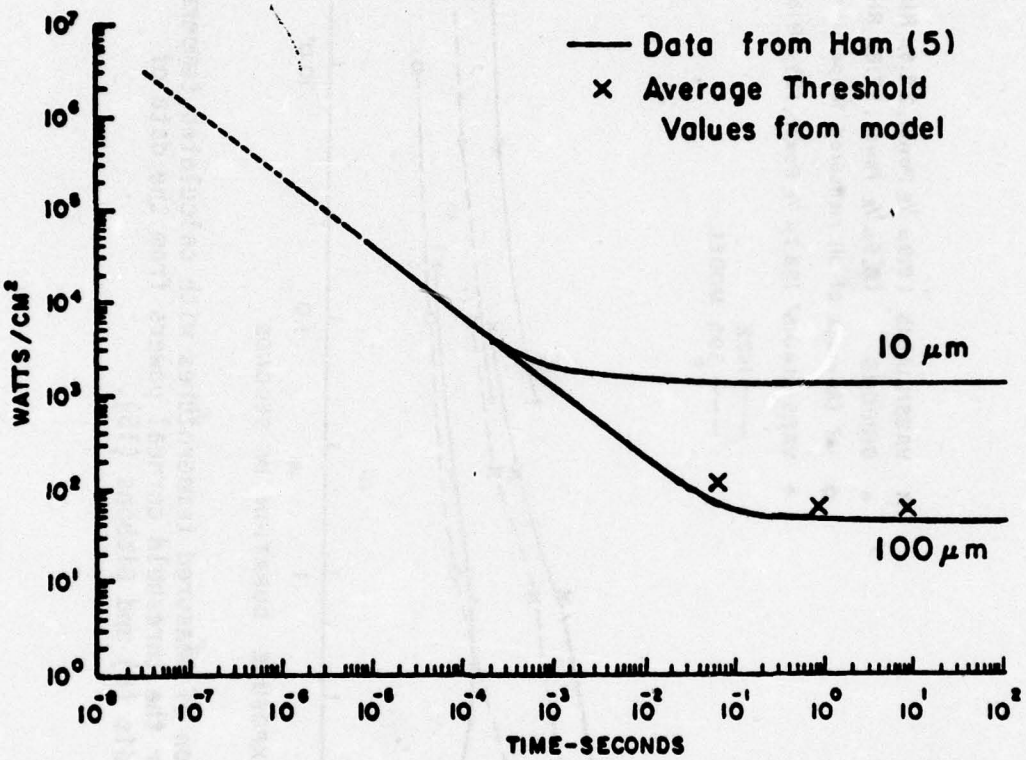

FIGURE 50: Retinal power density versus time of exposure for image radii from 10μm to 800μm from Ham (5) plotted with power density for average thresholds for .1 second, 1 second and 10 second exposures.

preretinal ocular media of .636. For Ham's study, the transmission of the preretinal ocular media was assumed to be 95%. The data from Ham et al. is for a white light xenon arc lamp with a filtered flat spectrum in the visible region.

Rate Process Model

The prediction of temperature rise in the retina is not sufficient for the prediction of damage due to high intensity light. Some "effect" function must be used in conjunction with the temperature model to indicate injury at the damage temperature. The rate process model proposed by Henriques (51) was intended for the purpose of prediction of porcine epidermal injury as a result of thermal insult. The form of the model is discussed in an earlier section of the background. The temperature measurements in this study that result in damage are compared to those predicted by the model proposed by Henriques. Rate model coefficients are also calculated for exposure durations from .1 second to 10 seconds for the temperature history at the lesion radius in this research.

Paramacular exposure center temperatures which produced an ophthalmoscopically visible lesion are plotted in Figure 51 with the lesion radius temperatures and the temperature of damage predicted by Henriques rate process model for $\Omega = 1$. The

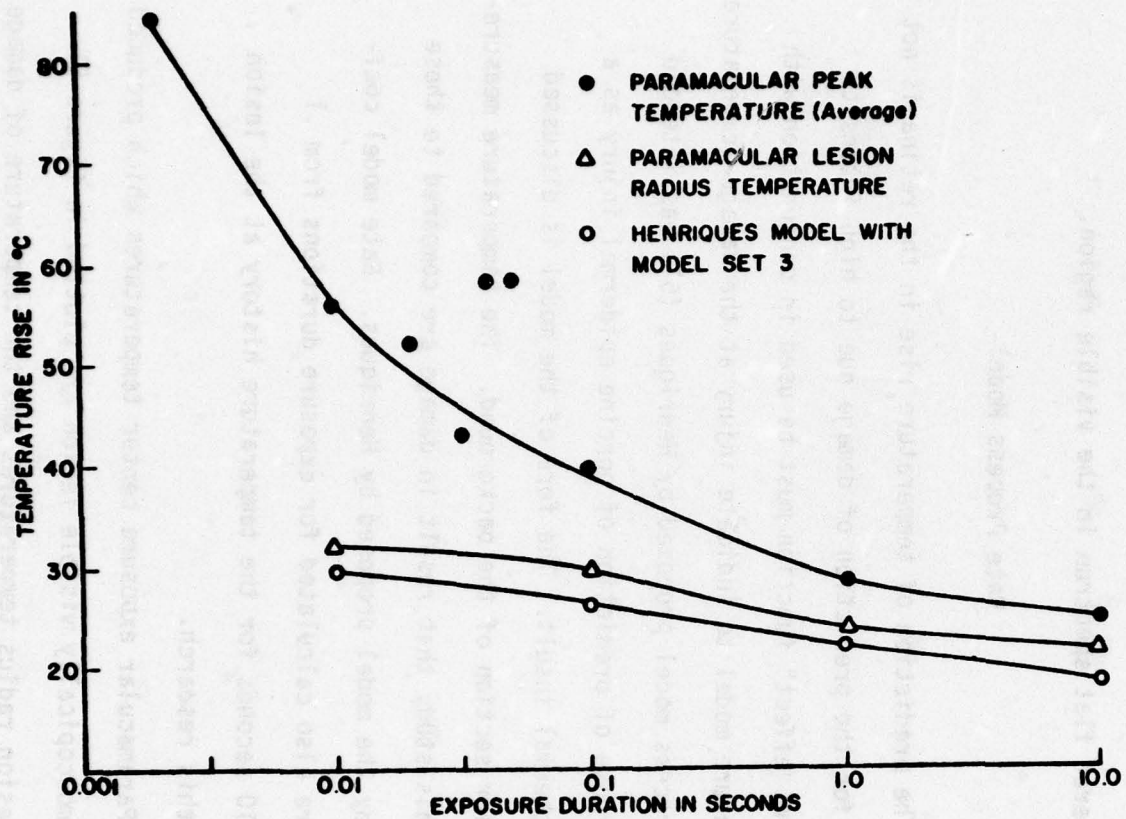

FIGURE 51: Plot of peak temperatures, lesion radius temperatures, and predicted temperatures from Henriques (51) model required to produce damage in the paramacular region of the eye.

coefficients in the rate process model are $A = 3.1 \times 10^{98}$ sec^{-1} and E = 150,000 cal/mole. At the lesion radius, the rate process damage integral in conjunction with the thermal model using parameter set 3 predicts temperatures of 29.5°C for a 10 millisecond exposure, 26.5°C for a .1 second exposure and 21.8°C and 18°C for 1 second and 10 second exposures respectively. The model values are computed for a gaussian image profile with half-power radius of 100μm. For the .01 second, .1 second, 1 second and 10 second exposure durations, the experimental lesion radius temperature increases are 39.4°C, 29.9°C, 23.5°C and 21.8°C, respectively. The higher paramacular lesion radius temperatures cause the rate process model to predict a larger radius than the radius observed in the experiment.

The macular temperature increases displayed in Figure 52 with the rate process predicted temperature show a different trend than the paramacular temperatures in the previous figure. For the .1 second, 1 second and 10 second exposure durations, the experimental lesion radius temperature increases are 83%, 91% and 97% of the damage temperature predicted by the rate process model in conjunction with the thermal model. For the .01 second exposure duration, the experimental temperature is 151% of the predicted damage temperature from the rate process model.

A comparison of the coefficients of the model by Henriques (51) for paramacular and macular temperatures with the experimental

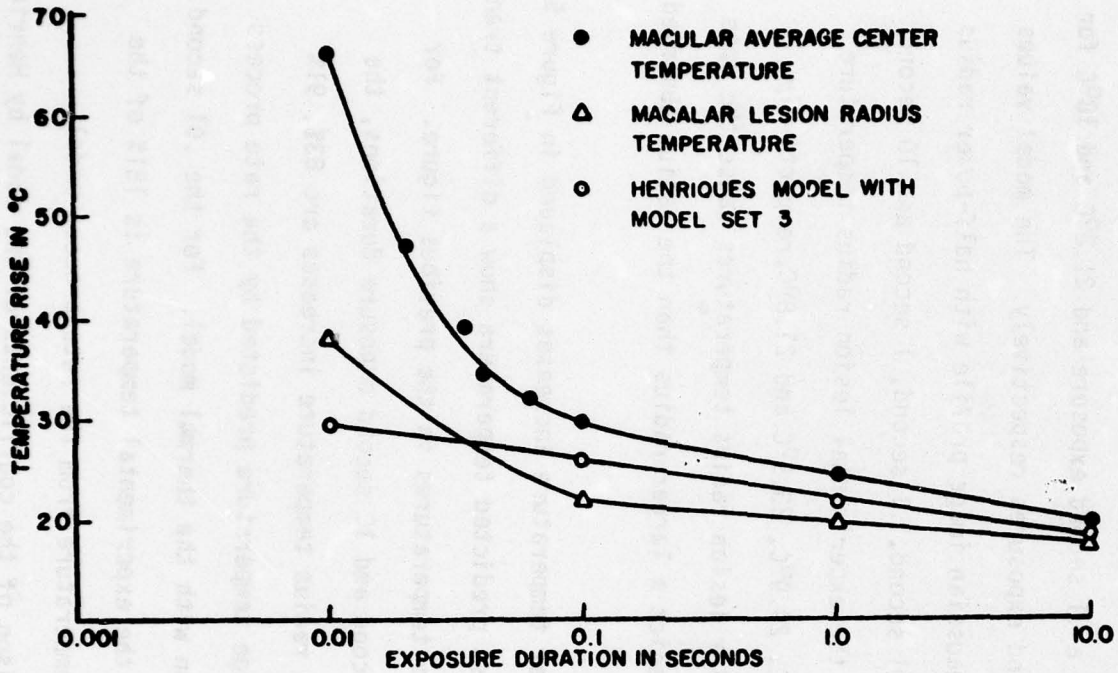

FIGURE 52: Plot of macular center temperature, lesion radius temperature and predicted damage temperatures versus exposure duration.

temperature increases may be made with the aid of Figures 53 and 54. The rate process model coefficients are derived from longer exposure durations than those in the present study and are obtained by assuming a step increase in temperature. The model coefficients are derived from a plot of $\ln t$ versus $1/T$ where t is the exposure duration and $1/T$ is the reciprocal of temperature in degrees Kelvin. The slope of this plot is E/R while the intercept is $-\ln A$ in the equation:

$$\Omega = Ae^{-E/RT} t$$

for an assumed value of $\Omega = 1$.

In Figure 53, graphs of $\ln t$ versus the reciprocal of the temperatures at the center of the lesion for both paramacular and macular exposures and for Henriques model assuming a step temperature increase is illustrated. The paramacular and macular temperatures at the lesion center are both greater than the temperature of damage (temperature at which $\Omega = 1$) for all exposure durations. At the shorter durations, however, the departure from a straight line plot for $\ln t$ versus $1/T$ is readily apparent. The temperature rise at the center is not a good indicator, since the area of damage extends radially some distance from the center.

In Figure 54, the paramacular and macular temperature increases at the center are multiplied by the average factor for temperature at the lesion radius (see Table VI) and plotted on

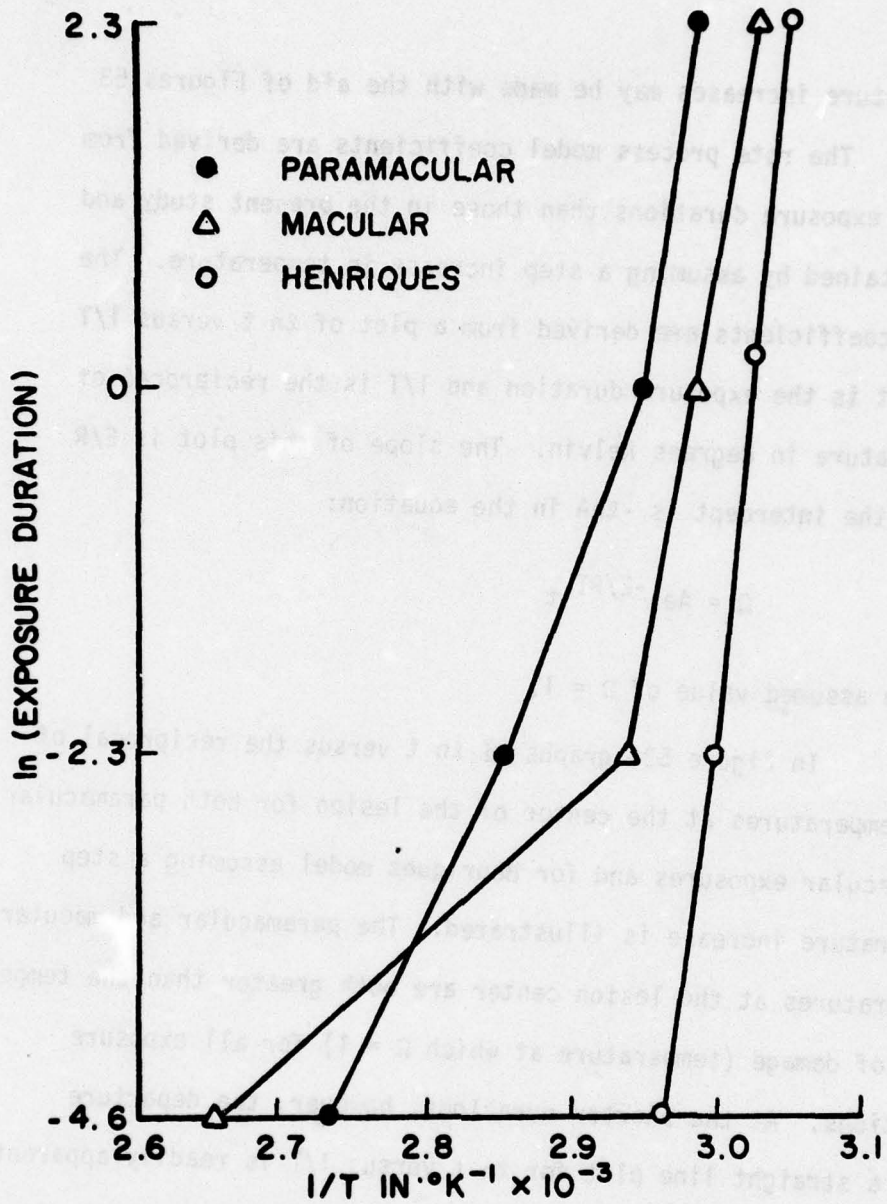

FIGURE 53: Plot of ℓn (exposure duration) versus the reciprocal of temperature rise at the center of macular and paramacular lesions. Henriques model predicted temperatures are plotted for comparison (51).

the ℓn t versus 1/T scale for comparison with the model by Henriques. From .1 second to 10 seconds (n t = -2.3 and 2.3 respectively) the data for macular and paramacular lesions may be nearly approximated by straight lines. At .01 seconds, the data again depart significantly from the straight line. Coefficients may be derived from the two straight line plots. The values of ℓn t and 1/T used to derive the rate process coefficients are given in Table XIII. The calculated coefficients in the rate process model for paramacular insertions are E/R = 71,956 cal/mole and A = 2.55×10^{94} sec^{-1} versus 75,000 cal/mole and 3.1×10^{98} sec^{-1} for Henriques model. For macular exposures, the calculated coefficients are E/R = 112,300 cal/mole and A = 8.4×10^{147} sec^{-1}.

TABLE XIII: Values Used to Derive Rate Process Coefficients

n t	1/T (Paramacular)	1/T (Macular)
2.3026	3.014×10^{-3}	3.053×10^{-3}
-2.3026	2.95×10^{-3}	3.012×10^{-3}

Probe Response Measurements

The rise time for the direct absorption of the thermocouple in different media is measured with an acousto-optic modulator in the laser beam. The rise time of the laser light pulse is less than 5μ seconds. Rise times for the thermocouple in air, water

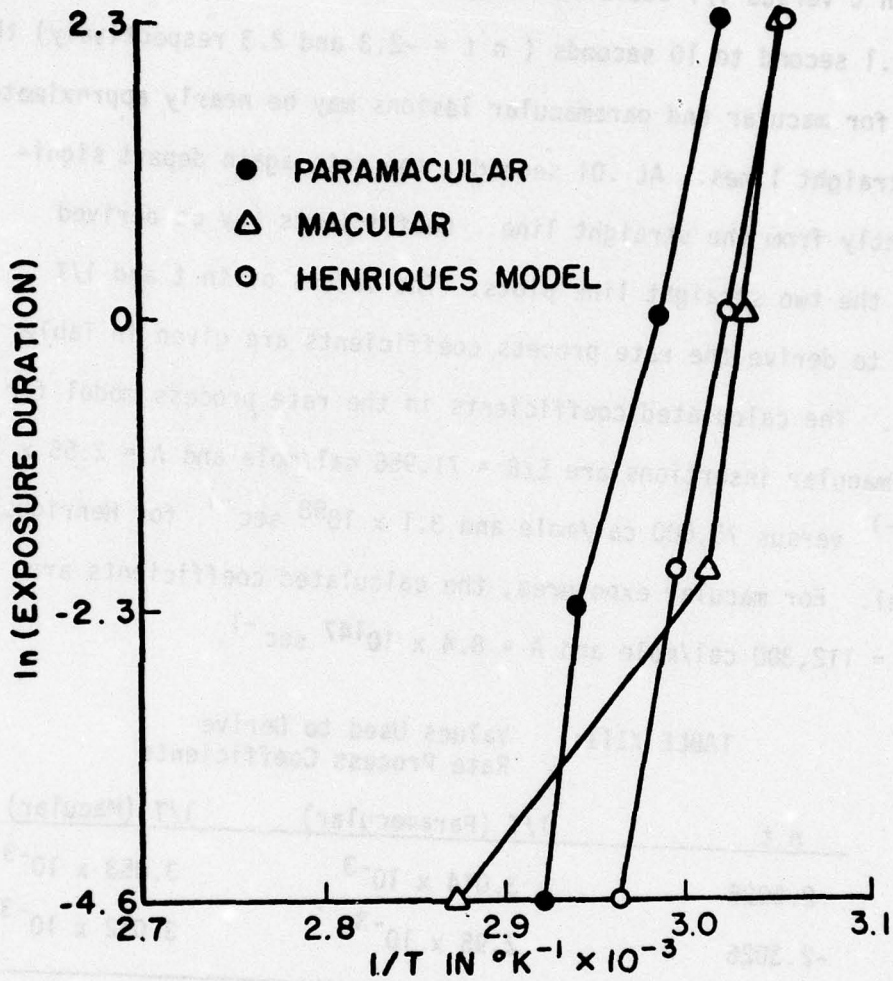

FIGURE 54: Plot of ℓn (exposure duration) versus the reciprocal of lesion radius temperature compared to Henriques model prediction of damage temperature (51).

and vitreous media are measured for the step-like increase in light input. The laser light must be focused to a small image in order to achieve temperature increases which can be measured above the noise of the system. Rise times are measured for 10 to 20°C rises above the temperature of the medium in which the thermocouple is imbedded. For a 19μm diameter probe, the rise time from 10% to 90% of the final temperature is .4 milliseconds in a water medium. This value compares to a computed rise time using equation 34 from Reed (49) for the step response of the probe in a heated medium of .3 milliseconds. In vitreous humor, the probe rise time is .7 milliseconds which compares to Reed's computed rise time of .8 milliseconds in a biomedium. In air, the measured 10-90% response time of the probe is 12 milliseconds. This value is much lower than the computed value of 30 milliseconds from Reed's model (49).

In a small number of experiments, the amplitude versus frequency plot for a few thermocouples is run in air and water media. The frequency response is run with the acousto-optic modulator modulated with a sinusoidal voltage. Focusing is again used to increase the power density at the thermocouple junction. The amplitude of the thermocouple response versus the frequency of the incoming light is plotted for both the air and water media for the same power density at the junction. The frequency response of the thermocouple in water is 10-20 times the frequency response (3dB frequency) in air. The amplitude of the thermocouple response is

larger for air than for water. If the frequency response (or rise time) in water 10 times the response in air then the amplitude of the temperature in air is 10 times the amplitude in water.

In Table XIV, frequency response measurements for thermocouple probes in air and water are tabulated for three probe diameters. The rise time indicated is computed from the 3dB frequency (the frequency of modulation of the light-input for which the voltage response is .707 times the input voltage). The rise time is related to the 3dB frequency (f_{3dB}) by $\tau_{10-90\%} = .35/f_{3dB}$. The frequency response is greater for smaller (19μm) probes than for larger probes. The computed rise times from the frequency response tests are higher for air than for water. For a 19μm diameter probe, the average rise time is 8.6 milliseconds in air and .35 milliseconds in water. For the 24μm and 30μm diameter probes, the average rise times in air are 15.7 milliseconds and 22.4 milliseconds, respectively. With the 24μm and 30μm probes in water, the average rise times are .63 milliseconds and 1.4 milliseconds, respectively. The ratios of the average probe response time in air to the average response time in water for the 19μm, 24μm, and 30μm probes are 24.6, 24.9, and 15.9 respectively.

TABLE XIV: Frequency Response and Computed Rise Time for Three Probe Diameters in Air and Water Media.

Probe Diameter (μm)	3dB Frequency Air (Hz)	3dB Frequency Water (Hz)	10-90% Rise Time Air (Seconds)	10-90% Rise Time Water (Seconds)
19	36.8	1000	.0095	.0035
19	35.0	875	.010	.0004
19	55	1170	.0064	.0003
24	25.8	556	.0136	.00063
24	17.8	520	.0197	.00067
24	25.5	600	.0137	.00058
30	15.0	243	.0233	.00144
30	16.4	220	.0214	.0016
30	--	292	--	.0012

CHAPTER V

DISCUSSION

Threshold temperatures have been measured with thin film copper-nickel thermocouples for the appearance of a visible lesion in the primate eye following exposure to laser irradiation. Temperature-time histories and profiles of the temperature increase in the retina have been presented in the previous section. The results have been compared to a digital computer solution of the heat conduction equation and a simple rate process model based on first order reaction rates.

Temperature Measurement

The measurement of temperature in a living tissue with an invasive technique presents several problems which affect the accuracy of the measurement. The probe is not truly authothermic with the tissue and is of finite size. The differences in thermal and absorptive properties of the probe and tissue cause errors in the probe measurement. Ideally, the probe should have identical properties with the tissue and be in intimate contact with the system under measurement. Since a complete match of the probe and tissue properties is not possible, care must be exercised in order to minimize the effect of probe and tissue property differences on the measurement of tissue temperature.

In this research, probe diameters from 10μm to 20μm

were employed to minimize the effect of the size of the probe on the measurement of tissue temperature. The finite size of the probe causes a shadowing effect for the light entering the tissue since the probe absorbs or reflects all the light which impinges upon it. To minimize the effect of shadowing, or removal of a portion of the source term, the image diameter must be much larger than the probe diameter. If the image is 10 times the size of the probe, only 1 or 2% of the source term will be lost.

Another problem associated with probe size is the averaging of temperature across the junction. Horizontal or radial averaging may be reduced by using larger images since large images tend to have smaller gradients in temperature with radial position. The ocular fundus contains two major absorbing layers, the P.E. and choroid. THE P.E. is only 10μm thick, and is highly absorbing, so small insertion angles of 10-30° cause some averaging to occur. A simple series of averages from the temperature model with parameter set 1, indicate that a 30° angle causes the errors indicated in Table XIV. The model averages are taken for half-power radii greater than 75μm. No horizontal average is taken since the model profile has no variation in the center of the beam for the 10μm or 20μm probe radius. The average is a simple axial average over the depth represented by D sin θ where D is the probe diameter and θ is the probe insertion angle. For the 20μm diameter probe, the average is taken over a 10μm depth for a 30° insertion angle. The temperature variation with depth for the

average is assumed to be linear over the small depth with $\left(\frac{T_{hot} + T_{cool}}{2}\right)$ the average value of tissue temperature. The data in Table XV are computed from the model values of monkey 9-73, 11-73, 1-74, 4-74, 9-74, 10-74, and 11-74. The values for RIM and half-power radii are given in Table X. The errors listed in Table XV are maximum errors for the probe positioned near the center of the P.E. (axial position of highest temperature for model set 1).

TABLE XV: Average Error Due to Axial Averaging of Temperature for Two Probe Diameters

Time	% Error for a 20μm Diameter Probe ($1 - \bar{x}$, s, n)	% Error for a 40μm Diameter Probe ($1 - \bar{x}$, s, n)
.001	26, 3, 7	46, 4, 7
.01	8, 1.2, 7	17, 2, 7
.1	4, .9, 7	7, 1.8, 7
1.0	3, .7, 6	6, 1.6, 6

Averaging over the axial length of the probe junction causes errors for a 20μm probe of 8% at .01 second and 3% at 1 second. For a 40μm probe, the error due to averaging is estimated to be 17% at .01 second and 6% at 1 second.

The averages above represent a worst case average with parameter set 1, since the absorption parameter for the P.E. implies that 80% of the light energy reaching the layer is absorbed in the P.E. Realistically, for parameter sets 2 and 3, the amount of

averaging is greatly reduced. In fact, for the 20μm or smaller probes used in this study, and parameter set 2, the average temperatures across the probe is within 5% at .01 second and for set 3, the temperature is within 3% at .01 second. The typical probe insertion is nearer 15° than the 30° used to calculate the effect of averaging. Therefore, probe averaging does not present a significant problem and is probably less than 3% for most exposure durations in the present study.

Another effect of finite probe size is the axial resistance to heat conduction down the probe. Larger probes have a larger effective cross-sectional area and thus a lower resistance to heat conduction. The resistance to heat conduction out the leads is inversely proportional to the conductivity of the lead material and the cross-sectional area of the lead and directly proportional to the effective length of the lead. In the present thermocouples, the small cross-sectional area of the high conductivity metal leads and the low conductivity of the quartz substrate tend to reduce the lead resistance effect. The effect of the lead resistance is to cause the probe to measure a lower temperature than actual tissue temperature. The magnitude of this error is difficult to determine because it also depends upon the resistance of the probe-tissue interface. This resistance is due to a finite heat transfer coefficient between the thermocouple probe and the medium in which the temperature is to be measured. For a higher junction to tissue resistance and a lower lead conduction resist-

ance, the probe measures a temperature lower than for the reverse situation.

An estimate of the effect of the probe lead resistance upon the measurement of steady-state temperature may be made with the aid of a simple resistance-capacitance analog of the probe-tissue system. In Figure 55 below, the analog to the measurement of step temperature increase is illustrated.

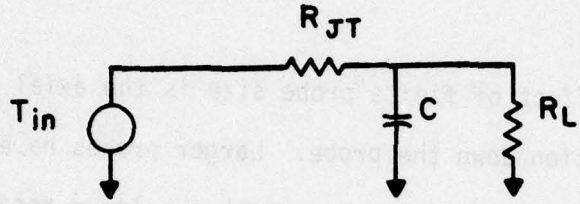

FIGURE 55: Resistance and Capacitance Analog for the Thermocouple Probe

For the measurements by Cain and Welch (32), and the model by Reed (49), the probe is inserted at t = 0 into a medium at constant temperature. The resistance R_{JT} represents the junction (or probe) to tissue thermal resistance, while R_L represents the thermal resistance of the probe leads. At steady-state, the temperature of the junction is given by

$$T_{probe} = \frac{T_{in} R_L}{R_{JT} + R_L} .$$

The magnitude of steady state error in the probe measurement depends upon the relative sizes of R_L and R_{JT}. The rise time of the probe in this situation depends upon the value of the effective thermal capacitance of the probe (C) which is given by $\rho V c_p$ where

ρc_p is the volumetric specific heat of the probe and V is the volume of the probe heated. The thermal resistances in parallel form an effective charging resistance for the probe thermal capacitance. The rise time is given by:

$$\tau = \frac{R_{JT} R_L}{R_{JT} + R_L} C.$$

For large values of R_L the rise time reduces to $R_{JT}C$ which is an idealized rise time and is the case for Reed's analysis. If R_{JT} is larger than the ideal thermal resistance, the rise time increases. In the experimental measurements, this resistance appears to be larger than ideal since the rise times measured by Cain and Welch (62) in water are longer than the computed rise times.

If the lead resistance (R_L) is less than about 10 times the junction to tissue resistance (R_{JT}), a significant temperature drop between the tissue and the thermocouple exists. The heat flux out the thermocouple leads is given by:

$$q_L = \frac{\Delta T_{J-\alpha}}{R_L}$$

where

$\Delta T_{J-\alpha}$ = the temperature drop from the tissue to the environment (37°C).

q_L = the heat flux out the leads cal/sec

R_L = the lead resistance = $\frac{\ell}{kA}$

ℓ = the effective lead length

k = the thermal conductivity

A = the cross-sectional area of the leads.

The heat flux from the tissue to the junction at steady state is equal to the heat flux out the thermocouple leads. For a horizontal cylinder (64), the heat transfer coefficient from a fluid medium (such as water) for natural convection is given by:

$$h_c = .53 \frac{k}{D} (GrPr)^{1/4}$$

where

h_c = the heat transfer coefficient from the fluid to the probe.

k = the thermal conductivity of the fluid

D = the diameter of the cylinder

Gr = the Grashof number = $f(\Delta T_{JT})$

Pr = the Prandtl number.

The heat flux from the medium to the probe is given by:

$$Q_{JT} = \frac{\Delta T_{JT}}{R_{JT}} = h_c(2\pi rL)\,\Delta T_{JT}$$

$$= f(\Delta T_{JT}^{5/4}).$$

The properties of the medium and the heat fluxes are functions of temperature and temperature driving potentials. The values for the resistances in the simple model are determined from the values for which $q_{JT} = q_L$.

The critical parameters in the determination of the error due to axial heat flow down the probe are the probe to tissue resistance, the length and the diameter of the probe. Blackwell (65, 66) has made calculations of the minimum length to diameter ratio for thermal probes for negligible errors due to axial conduction. He calculates steady state errors for the axial flow problem as a departure from the solution for radial flow only. He concludes that for length to diameter ratios greater than 25:1, the error is on the order of 2% for solid metal probes and low heat transfer coefficient values. For the much lower conductivity of the probes in this research, the error should be much smaller. The probe in the temperature measurement application is in 1 millimeter of tissue and the diameter is less than 20μm. The length to diameter ratio is therefore approximately 50:1, and the steady-state error is negligible.

A final property of the probe which causes errors in the measurement of transient temperature increases the eye or any other bio-system is the rise time of the probe tissue response. This reponse time depends upon the medium in which the probe is imbedded, the thermal properties of the probe, and the radius of the sensor substrate. The resistance between the probe and the tissue, mentioned in the previous section, also affects the rise time. From measured values and the sizes of the probes used in this research, the response time for the probe to reach 90% of the

tissue temperature is less than one millisecond. This value is assumed since the resistance to heat flow in the bio-system should not be drastically different from the resistance between the probe and water as shown in Cain's experimental measurements (62). For 10μm radius probes, calculated response times in skin and water and measured response times are all less than one millisecond for Reed's model and Cain's experimental measurements.

Other factors in the system which limit the accuracy of the temperature measurements include the system noise level and the bandwidth of the electronics which record the temperature. The measured input noise for the system used in this research is 4 μV RMS referred to the input of the thermocouple amplifier. This gives a resolution of ± .2°C for the copper-nickle thermocouple with an EMF of 20μV/°C. The overall bandwidth of the measurement system is 10 kHz, which is equivalent to a rise time of 35μseconds for a step input.

Other characteristics of the recording system also affect the accuracy of the measurement of temperature rise. The analog recorder has an RMS noise level of .05V. This has a varying effect on the temperature measurement since the gain prior to the tape system is important in the determination of the minimum resolvable temperature change. For most of the temperatures measured in the results section, the tape noise is less than .5°C. For higher values of pretape gain, the error is much less

than .5°C. The analog to digital conversion adds more noise to the record in the form of quantization noise, which is ± 1/2 times the least significant bit. The A/D converter is a 12 bit system. The cumulative effects of all the noise in the recording and measurement system amounts to less than ± 1°C. This represents an error of ± 5% for a 10 second threshold temperature of 20°C.

Threshold Determination

The method of threshold determination in this research was the appearance or non-appearance of an ophthalmoscopically visible lesion 5 minutes post exposure to laser irradiation. This criterion was chosen to allow rapid accumulation of data and to facilitate threshold determinations for several exposure durations in the same eye. The visible lesion criterion is relatively standard throughout past research, although other investigators have used various times of observation post exposure as the criterion for threshold damage. Even though the appearance of a visible lesion in no way implies a loss of functional vision, it provides a much more easily determined reference point for the comparison of results between investigators than histological or histochemical techniques. For the reasons of easy and rapid threshold determinations and the availability of data for comparison, the 5 minute visible lesion criterion was chosen.

Several factors affect the accuracy of threshold determination by ophthalmoscopic observation techniques. The determination of the visible threshold is a subjective technique which depends upon the condition of the experimental animal, the expertise of the observer and the size of the retinal image. The fundus of the experimental animal must be maintained at a reference temperature (37°C) and the condition of the eye must be carefully monitored. If the cornea is allowed to dry, the subsequent clouding reduces the amount of light reaching the retina and makes visual observation of the lesion more difficult. In this research, the temperature of the fundus is kept at 37°C and the cornea is covered with a contact lens to prevent drying of the corneal epithelium. The contact lens causes a 1.6% reduction in the power entering the eye since its index of refraction is higher than the index of refraction of the water layers at the cornea.

The observer makes a judgment of lesion appearance based upon changes in the reflectance of the fundus following laser exposure. For the 5 minute visible criterion, a "threshold" lesion is one which appears 5 minutes following the exposure. For super-threshold exposures, the lesion may appear immediately or a short time following the irradiation. For sub-threshold exposures, lesion appearance may or may not occur at some longer observation time. As mentioned in the background section, Davis and Mautner (14) note a 20% difference between immediately visible

threshold lesions and lesion appearing one hour post exposure, Gibbons (15) observes no difference between one hour and 24 hour lesion criteria for times of exposure less than 5 seconds.

In past experimental determinations, the corneal power of the irradiance (J/cm^2) at the retina have been used as a measurement of threshold exposure. The range of power or energy for a given exposure duration varies by more than an order of magnitude between investigators and within a set of experiments by a single investigator. The major reason for this discrepancy is probably in the determination of retinal image size. The point spread function of different animals, even of the same species, exhibits some variation since not all animals have the same total refractive power. Residual accommodation and errors in the placement of external lenses can cause large errors in the size of the retinal image. Errors in the estimation of image size are magnified since the energy per unit area used in past research is a function of the square of the assumed radius of the retinal image. In the measurement of thresholds using minimal images, an error of ± .25 diopter in the measurement of refractive power of the eye could result in an image of 34-45μm rather than the assumed 10-20μm image used in many studies (63). For this reason, the muscles of the lens must be paralyzed and an accurate measurement of the image size must be made.

In this study, paralysis of the muscles is accomplished with curare and the retinal image size is measured directly at the retina with the thermocouple. The effect of image size and distribution may be seen from the tabulated data in the results section. For small images, the power required is smaller than the power required for large images. For images which differ significantly from the Gaussian distribution, the power required to produce a lesion changes relative to a Gaussian profile with the same half-power radius. For example, a profile with large tails requires more power for a threshold exposure than a profile with a smaller amount of energy in the tails of the distribution.

The measurement of threshold temperature depends upon the linearity of temperature rise with corneal power for a given image distribution. In this research and the study by Cain and Welch (32), the linearity of temperature versus corneal power for a given image distribution has been demonstrated for temperature increases up to 50°C above baseline temperature. The threshold temperature in most of these experiments is extrapolated from temperature increases for corneal power levels 50-75% of the threshold value. The standard deviation of the threshold temperatures for each exposure duration is within 15% of peak temperature with the exception of .01 second exposures for which only a few points are available. The corneal power standard deviation is larger than the standard deviation in temperature since the image

size and distribution appear to have a much greater effect on the power level for threshold than on the threshold temperature.

Lesion Size and Lesion Temperature Measurements

The size of a lesion which is produced by exposure to an intense light source depends upon the image size and the duration of the exposure. Also, biological amplification may play a part in the lesion size. The lesion size is larger for large images and long exposure durations than would be expected for the lesions produced by small images and short duration exposures. Biological amplification is due to changes in the tissue such as the buildup of toxic metabolic by-products from increased cellular metabolism and the immune response of the tissue which results following cell death. The lesion may therefore be larger as a result of this "amplification" than the size that would be predicted on the basis of increased temperature alone. In fact, in response to injury, a minimum volume effect due to cellular necrosis may be evident for small images or short exposure durations (63).

Ophthalmoscopic measurement of lesions for .01 second to 10 second exposure durations are listed in the results section in Table VI. At short times of exposure, the radius of the image normalized to the half-power radius is much smaller than for long times of exposure. The half-power radius is a better parameter than the maximum image radius since calculations using the half-power

radius as the reference for lesion radius result in much lower standard deviation of normalized image radius. Using the ophthalmoscope reticle to estimate lesion diameter is limited in accuracy and may not provide a true picture of the lesion behavior with exposure duration. The resolution of lesion diameters measured with the ophthalmoscope is at best ± 20μm. The resulting 80-90% accuracy is due to the 13μm separation of the reticle divisions and the lesion boundaries are not clearly defined. The lesion appears as a gray or white circular area which represents a change in the reflectance of some of the layers in the fundus. The lesion probably occurs near the receptor layers (63) even through the major site of absorption is in the pigment epithelium. For a lesion to be visible, coagulation of proteins probably occurs over a large volume of the retinal tissue in order to produce the changes in the diffuse reflection of light which make the observation possible.

The fact that most threshold visible lesions require some finite time to develop (at least for exposure durations longer than 1 millisecond) points to a biological process such as protein coagulation and denaturation or localized edema rather than a physical response such as steam formation. Around the melanin granules, however, the temperature may be locally high enough to produce steam. This is not in itself sufficient to produce the effect seen in the formation of a visible lesion, since most

lesions are not immediately observable. Localized edema and fluid leakage around damaged cells certainly causes swelling of the tissue and a slight change in the refractive index of the tissue. All these effects combine to produce a visible lesion which can be observed with an ophthalmoscope.

Even for small image diameters, a critical volume of tissue must be involved in the thermal insult for the damage to be observable with an ophthalmoscope. The observed lesion size for minimal images of 20μm half-power radius is about 30-50μm. For larger images the size of the damaged volume increases in radial extent (63). The minimum lesion size for small images may be a function of biological amplification or a minimal response to tissue injury. The time course of biological amplification due to cellular death and the subsequent buildup of toxic byproducts follows a time course similar to that noted for lesion formation (63). The damage to cells in the area of a lesion may be due to a buildup of toxic metabolic byproducts because of interruption of local circulation and the loss of nutrients needed to sustain the cell. Thus, cell death and edema probably contribute more to the appearance of a threshold lesion than steam formation or acoustic transients in the range of exposure durations used in this research. These processes are the result of elevated temperature and depend upon the duration and intensity of the exposure and therefore fit the definition of a rate process.

Measurements of the lesion radius are used in conjunction with the horizontal profiles to predict the temperature rise at the lesion radius. The lesion radius temperature is extrapolated from subthreshold measurements by the ratio of threshold corneal power to the corneal power for the particular horizontal scan. The temperatures at a given radius for a particular image distribution are linear with corneal power as are the center temperatures discussed earlier. Because of the inaccuracy of lesion radius measurements, the variation in threshold lesion radius temperatures is larger than the variation in lesion center temperatures. The variation in lesion radius temperature due to the measurement uncertainity is much smaller for 10 second temperature measurements than for .01 second temperatures since the radial gradients are smaller for long times of exposure than for short exposure durations. The uncertainity in lesion radius threshold temperature therefore becomes less as the duration of the exposure for which the threshold is determined increases.

Model and Experimental Threshold Comparisons

In the comparison of model and experimental threshold values, a number observations may be made. First, real differences exist between macular and paramacular thresholds determined in this study. The most striking difference is the difference in temperature increase required for visible lesion appearance at the

two insertion sites. Another difference is the longer rise time for paramacular temperature increases compared to macular increases in temperature. The model calculated threshold temperatures fit the macular experimental values more closely than they fit the paramacular experimental threshold temperature increases.

Since the damage to the fundus is a function of the temperature-time history, a longer rise time for the temperature for a given image size or insertion site should imply a higher end point temperature than a temperature-time history with a shorter rise time. Even though the macular rise time is shorter by a factor of three than the paramacular rise time for 50μm half-power images, this in no way explains the approximately 20% higher temperatures required for paramacular visible lesions if the simple rate process model applies to the injury of retinal tissues. The rate process model based upon the Arrhenius equation is a very sensitive function of temperature. For the 20% increase in center temperature, the lesion in the paramacular region should be much larger in radial extent and axial extent than the lesion in the macula. The paramacular threshold lesion therefore would involve a much larger volume of tissue than the macular threshold lesion. Unfortunately, only macular lesion measurements have been made for a number of experiments. No differences can be demonstrated in macular and paramacular lesion diameters because only a few paramacular lesions have been measured and no direct comparisons of

macular and paramacular lesion sizes for the same image size have been made.

Several observations from past research, however, deserve further note in regard to the possible reasons for macular and paramacular threshold differences. The first observations relate to structural and anatomical differences between macular and paramacular regions. The macula appears darker on ophthalmoscopic observation than the paramacula. The macula also contains a yellow pigment (Macula Lutea) which absorbs in the blue and green spectra. Also, the neural layers are much thinner in the area of the macula and the fovea than in the paramacular region of the eye. The dominant cell types in the macula and paramacula are also different. In the macula, the predominant receptor cell is the cone cell while the extramacular receptor cells are predominantly rod cells. There is more circulation in the neural layers of the paramacula than in the macula. The neural retina in the paramacular region has major vessels and extensive capillary circulation while the macular retina is largely avascular. Therefore, several major anatomical differences exist between the macula and paramacula. Whether these differences contribute to the observed threshold temperature rise discrepancies or not can only be a matter for speculation.

The threshold corneal power required for macular and paramacular lesions produced by the same image sizes is also lower for macular thresholds than for paramacular thresholds. For 50μm

half-power images in the macula, the corneal power is approximately 33 milliwatts while the paramacular threshold is 65.2 milliwatts for a .1 second exposure duration. For a single threshold in the same eye, with 105μm half-power radius, the macular lesion requires a corneal power of 72.1 milliwatts while the paramacular lesion requires 101 milliwatts for threshold corneal power at .1 second exposure duration. At one second, macular lesions require 20-25% less corneal power than paramacular lesions. Ten second macular threshold lesions are produced with 20-25% less corneal power than paramacular threshold lesions. These observations parallel the results of other investigators (6, 12, 67) for other wavelengths. Lappin (12) found a reduction in corneal power for macular lesions, for He-Ne wavelengths, at 1 to 10 seconds of 20-25% from the power required for threshold lesions at extramacular exposure sits. At .01 second, the paramacular lesion threshold corneal power is more than twice the macular threshold power. For ruby exposures, Vassiliadis, et al. (6) find that the macula is 2.2 times more sensitive than the paramacula for 1.7 millisecond exposures. They state that the reason for the difference may be that the macula is more heavily pigmented than the extramacula. This implies that the absorption of light in the macular P.E. and choroid is greater than the absorption in the paramacula. Campbell (67) finds the macula 2.5 times more sensitive to ruby laser irradiation than the paramacular for exposure durations shorter than 1 millisecond.

The reasons for the difference in sensitivity of the macular and extramacular regions of the eye is not clear, but generally the arguments for the difference tend to support several hypotheses: (1) That the observation of a lesion in the macula is easier than the observation in the paramacula due to the darker background, (2) That the absorption profile in the macula and paramacular regions are different, (3) The cones and rods may exhibit differential sensitivity to damage by intense light which implies a different damage mechanism for macular and paramacular regions, and (4) anatomical differences between the macula and paramacula contribute to the different threshold temperatures in the two areas.

The differences in macular and paramacular light absorption and thickness probably contribute to the darker appearance of the macula. Brindley (68) finds a difference in optical density of the neural retina in the two regions of a factor of two at 5000Å wavelengths. The macular retina, even with its reduced thickness has a density twice that of the paramacular neural retina. This factor could account for the darker appearance of the macula ophthalmoscopically. The change in reflectance which represents a lesion could therefore be a result of the requirement that a larger volume of tissue must be denatured or be edematous in the thicker, less absorbent extramacular retina than in the thinner, more absorbent macular neural retina. A smaller volume of tissue

change would produce the same reflection in the macula that a larger volume of tissue change would produce in the paramacula for wavelengths near 5000Å. The thicker paramacular retina causes more scattering of light since for a small volume more retinal thickness is present between the observer and the lesion boundary. Assuming that less light is transmitted through the layer from the lesion in the paramacula because of light scatter than in the thinner macular layers, a small lesion or tissue volume change would be more observable in the macula. For longer wavelengths, the two areas exhibit approximately the same optical density.

The second hypothesis of higher absorption in the P.E. and choroid of the macula than in the extramacular region, may be supported by the observation that higher corneal power is required to produce a threshold lesion in the paramacular areas of the eye. This assumption does not indicate that the temperature should be different for the two sites, but the absorption parameters must be different. For short exposure durations, the heat conduction equation becomes:

$$\frac{\alpha H_0}{\rho c} = \frac{\partial T}{\partial t}$$

and the temperature rise is proportional to the absorption parameter and the irradiance H_0. The longer rise time of the paramacular region indicates that it has a smaller absorption coefficient than the macular region of the eye.

The difference in corneal power required for macular and paramacular lesions appears to be present at argon wavelengths used in this research as well as the helium neon (12) and ruby (6) wavelengths. This indicates that some difference exists in either the volume of damage required to produce an observable effect in the two major areas of the eye or of some difference in the damage mechanism by which the lesion becomes visible. Tso et al. (69, 70, 71) in studies of the repair and development of retinal lesions find that cone cells are much more susceptible to damage than rod cells. Although their studies are performed with an argon laser for the evaluation of differential rod and cone damage and they are done in the periphery of the monkey eye, they feel that the susceptibility of the cone cells is not wavelength dependent. They conclude that the differences in susceptibility of the two cell types to laser radiation explain the increased corneal power required to produce lesions in macular and paramacular areas (70).

Since experiments of Tso et al. are conducted in areas of the retina which contain both rod and cone receptors, the observed differences in damage to the two cell types are probably due to general morphological differences noted in their histologic studies. First, cone and rod cells exhibit different interfaces with the pigment epithelium. The cone cells are surrounded by more densely pigmented villi from the P.E. than are the rods.

The villi from the P.E. also appear to extend farther around the cone cell outer segments than around the rod outer segments. Nuclei of cone cells are observed often in the inner segments of the receptor layer in the normal retina as an anatomic variant. The nuclei of cone cells also appeared to be more sensitive to thermal effects from photic injury than the nuclei of rod cells since the nuclei of the cones are physically nearer to the pigment epithelium. The outer segments of cones in detached retinas of rhesus monkeys are observed to recover more slowly than the outer segments of rods.

The lesions in their studies extend over the inner and outer segments of the receptor layer of the neural retina with the approximate center at the external limiting membrane. All nuclei in the outer nuclear layer are affected initially, and the swelling of the tissue due to edema causes normal nuclei to be displaced from the lesion center. In the periphery of the lesion only rod nuclei may be seen at long times post exposure. The rod cells apparently regenerate after some period of time with the cone cells being selectively destroyed. This effect is also seen in Xenon arc lamp coagulation which leads to the conclusion that the sensitivity of rod cells may not be wavelength dependent.

In the macular region of the eye, the cone cells are densely packed and no neural layer circulation exists. In the fovea, an extremely high cell density of cones is present. As

the distance from the macula increases, the density of cones is very low and rods are predominant cell types. In the periphery of the retina, rod cells of lower density are predominant. In peripheral and extramacular neural layers, the inner layers have an extensive capillary circulation.

The absorptive properties of blood and blood vessels are higher for argon wavelengths than for other visible wavelengths. Thus, in the paramacula, some of the energy at argon wavelengths is lost in the retinal layers. However, as even larger percent of light may be lost in the Macula Lutea of the macular region. These source terms are not accounted for in the model since no reliable measurements of the magnitude of this absorption are available.

The difference in threshold power for macular and paramacular regions may be explained by damage volume differences required for observations or by the differential absorption and sensitivity of cone and rod areas of the retina. It does not appear that a true explanation of the differences in temperature rise can be resolved until histological or histochemical evidence of damage volume differences is available. The apparent differential absorption phenomena also need to be investigated for both macular and paramacular areas. Past studies have not indicated, in sufficient detail, adequate reasons for the temperature difference noted in this research. Without histological evidence and accurate

measurements of absorption parameters, the model cannot be expected to describe the effects that have been noted in this and other research. It appears, however, that because of real anatomical differences between the two major areas of the eye that a simple, universal model for temperature increase and thermal damage cannot adequately describe the injury in the two areas.

Model and Experimental Scans

From the horizontal and axial scan data compared with model values, several differences between model and experimental values are apparent. First, horizontal scans in macular and paramacular areas reflect the problems noted in the comparison of temperature-time histories. In the Results section, the measured rise time for the paramacular temperature rise is seen to be longer than the rise time for temperature increases in the macular region.

Generally, the paramacular measured center temperature are higher than the model predictions for 1 second and 10 second exposure durations. For exposure durations of .1 second and below, the measured temperature increases are lower than the calculated values. However, at large radial displacements from the lesion center, the measured paramacular temperatures are higher than the model temperatures. This effect is normally at displacements much larger than the lesion radius. It may be caused by the presence

of blood flow in the paramacular region which causes the effective conductivity to be larger since blood which absorbs light more heavily in the argon spectrum than in other parts of the spectrum enhances the transport of heat by a convective mechanism. In the macular region the lack of blood flow is probably the reason that this effect is not noted for horizontal scans in the macula.

Axial scans in the two areas of the eye are much smoother than the model predicted scan for parameter set 1. Some of this effect may be caused by probe averaging as mentioned earlier. The axial scans are the most difficult of the scans to accomplish. Some of the problems which may cause discrepancies between model and experimental axial scans are: (1) the condition of the probe track through the tissue; (2) the probe may hang on tissue during the scan; (3) the assumed homogeneity versus the actual inhomogenous structure of the various layers in the fundus, and (4) the lack of accurate knowledge of the absorption parameters in the various layers and areas of the fundus. The first point is very important to any attempt to measure the absorption parameters in the tissue by means of an axial scan and to the measurement of temperature in the various layers. The track of the probe through the tissue is at an angle to the axis of the beam and the finite size of the probe causes some tissue deformation. If a hole in the tissue exists, a larger than normal direct absorption component will be present on the axial temperature increase for at least the

first several tens of micrometers behind the P.E. A subretinal hemmorhage in the choroid will cause a lower blood perfusion rate than for normal tissue and may cause a local change in the absorption of light. A hole in the neural layers or in the P.E. and choroid increases the contact resistance of the probe-tissue interface. Most of these effects probably cause perturbation of temperature fields in the tissue, especially for short exposure durations. The volume effect of tissue heating tends to reduce these problems for longer exposure durations if the abnormality in the tissue is confined to a small volume of the heat source.

In most scans, the probe is withdrawn from the neural layers in small steps rather than driven into the tissue from the sclera. The reasons for this approach are that the image must first be located and the simplest method is by visual positioning of the probe in the laser image through the fundus camera and that the probe hangs on the tissue more frequently in the forward direction. If the probe hangs in the reverse direction, the scan is not good, but if it hangs in the forward direction it usually results in a broken probe. If the probe hangs on the tissue during withdrawal, the temperature exhibits an abrupt decrease at some point during the scan.

The model assumes that the tissue is homogeneous, with constant absorption parameters in the P.E. and choroid layers. This is clearly not an accurate representation of the tissue system.

The tissue is not arranged in homogeneous layers. In fact, uncertainity in the definition of the depth of the layers as well as local variations in the blood flow, pigmentation, and layer thickness make the descriptions of the absorption profiles and therefore the variation in temperature versus position for short exposures very difficult. The P.E. is not a homogeneous 10μm thick layer as the model assumes. This layer is non-uniform in thickness and has projections (villi) which reach into the neural layers (outer segments) which vary in pigmentation and length around rod and cone receptors as discussed before (70). The choroid layer contains both blood vessels and pigment granules which vary as a function of position in the eye. The choriocapillaris which underlies the P.E. extends only several tens of microns into the 100μm assumed thickness of the choroid. The band of pigmentation is irregular in extent through the choroid layer. These observations indicate that more layers should be included in the model especially for short duration exposures for which energy density rather than volume effects are important. The assumption of homogeneity may not be too bad for a point near the center of the irradiated volume of tissue for long exposure times. The exposure durations used in this research are relatively long compared to the times required for significant conduction effects to "average" the affects of varying absorption within layers. For times longer than 1 millisecond the tissue can probably be represented by average

absorption and thermal parameters within some small range of error.

Model Parameters

The value of the parameters in the thermal model are very important to the accurate prediction of temperature increase in the fundus. As noted before, the absorption profile in the tissue is probably not the same in the tissue as that assumed for homogeneous absorbing tissue layers. For long exposures, however, the averaging effect of heat conduction tends to reduce the effect of small inhomogeneities. At short times, the important parameters are absorption coefficients and volumetric specific heats for the absorbing bodies in the tissue. Calculations by Hayes and Wolbarsht (72) indicate that the melanin granules may achieve temperature increases of several hundred degrees centigrade for theshold exposures below a few microseconds. If this is true, local variations in tissue absorption around the melanin granules surely occur due to denaturation and coagulation of protein and steam bubble production in the tissue surrounding the granules. The .01 second duration exposures of this research may exceed phase change temperatures near the center of the lesion. Change of phase may also cause changes in the tissue absorption properties. Thus, the assumption of constant absorption parameters for the various layers is probably not valid for short duration threshold

temperatures with the model.

Local blood flow effects in the macula and paramacula are not accounted for in the model. The effect of blood flow on the temperature increase is not even included in the simplified thermal model used to predict retinal temperature increase. The parameters involved in the analysis of blood flow should account for the influence of not only the cooling effect on the tissue but also the spectral absorption of the vessels and hemoglobin within the layers in which significant blood flow is present. No accurate numbers exist for either blood perfusion rates or the absolute value of hemoglobin spectral absorption. Blood flow is variable within the various regions and layers of the tissue. Bebie et al. (73) estimate that 22% of the argon laser light reaching the paramacular neural retina is absorbed in the capillary bed in the neural layers.

Measurement of direct absorption on the thermocouple as a function of axial position in the tissue does, however, appear to fit the exponential absorption profile in the results section relatively well. The probe smoothing effect and probe track condition could, however, have a great effect on these measurements. The calculated absorption coefficients for two scans are 648 cm^{-1} and 119.4 cm^{-1} for the macular P.E. and choroid; for one run in the paramacula P.E. and choroid coefficients appear to be 390.2 cm^{-1} and 102.6 cm^{-1}. The small number of scans are due to the spectral techniques which must be employed to obtain these scans. The probe

track must be in good condition, the probe cannot hang on the tissue, and a high power and short pulse must be used to give sufficient direct absorption for the measurement.

The measured parameters do, however, closely correspond to parameter set 2 for the macular experimental values and to parameter set 3 for the paramacular experimental parameters. If these parameters are accurate, they provide a partial explanation for the differences in average rise time between the macular and paramacular temperature-time histories. The higher absorption parameter implies a greater initial slope of temperature versus time for the macula and, therefore a shorter rise time. The model also reflects this for parameter sets 2 and 3. Parameter set 2 has a greater initial slope of temperature versus time and a faster rise time due to the higher value for the P.E. absorption coefficient.

In Table XVI, the average values of threshold temperature for macular exposures are compared to the model predicted average values for exposure duration from 10 seconds to .1 second.

TABLE XVI: Comparison of Macular Experimental and Model Threshold Temperatures

Exposure Duration (seconds)	Experimental Temperature Rise (oC)	Model Set 1 Temp. Rise (oC)	Model Set 2 Temp. Rise (oC)	Model Set 3 Temp. Rise (oC)
10	19.9 ± 1.5	19.3 ± 3.2	18.3 ± 2.6	20.4 ± 2.4
1	24.1 ± 3.4	21.8 ± 5.7	21.9 ± 4.4	24.4 ± 4.1
.1	29.4 ± 3.9	29.3 ± 8.0	29.8 ± 5.9	32.1 ± 5.4

In Table XVII, the average lesion threshold center temperatures for paramacular exposures are compared to model predicted values for 10 second to .1 second exposure durations. It appears that model set 3 provides a slightly better "fit" to the macular experimental data and a much better fit for the paramacular data.

TABLE XVII: Comparison of Paramacular Experimental and Model Threshold Temperatures

Exposure Duration (seconds)	Experimental Temperature Rise (°C)	Model Set 1 Temp. Rise (°C)	Model Set 2 Temp. Rise (°C)	Model Set 3 Temp. Rise (°C)
10	24.8 ± 1.7	21.9 ± .6	19.9 ± 5.4	24.9 ± 5.3
1	28.7 ± 3.0	27.3 ± 4.5	25.1 ± 5.8	29.4 ± 4.9
.1	40.0 ± 5.1	47.7 ± 9.0	43.5 ± 9.6	45.5 ± 8.2

Since paramacular exposures represent only about one-third of the exposures in this research direct comparisons are difficult. The average temperature increases do not reflect changes in image sizes between macular and paramacular insertions as the corneal power average values do. The relatively good agreement of the model for both macular and paramacular exposures of duration longer than .1 second, for all parameter sets, indicates that the volume of the source term rather than the absolute value of the absorption parameters, is most important in the determination of tissue temperature increase.

The absorption values for set 1 are probably too high for the preretinal ocular media and the P.E. Sets 2 and 3 have a more realistic value for TOM based upon earlier discussions. The values of absorption in the P.E. and choroid for sets 2 and 3 agree fairly closely with the values obtained for a small number of axial scans in the macula and paramacula respectively. The model exhibits good agreement with both macular and paramacular temperature increases over the range of exposure durations from .1 second to 10 seconds. The values obtained are within the range of experimental errors discussed in earlier sections.

At .01 seconds, several problems were noted during the course of the experiments which affect the threshold temperature measurements and model values. First, for the higher corneal power required to produce a lesion at .01 seconds, the neutral density filters heated causing a change in power with time. Second, the laser exhibited larger divergence angles for high power than for lower power settings. These problems were not present for the lower power settings required for durations of exposure longer than 40 milliseconds. The .01 second exposures therefore required a different optical system and a much more time consuming experiment than the longer duration exposures. The large standard deviations seen in the .01 second exposures were due to the errors induced by he problems mentioned above.

AD-A035 057 TEXAS UNIV AT AUSTIN ELECTRONICS RESEARCH CENTER F/G 6/18
THE MEASUREMENT OF THRESHOLD TEMPERATURES IN THE OCULAR FUNDUS --ETC(U)
FEB 76 L A PRIEBE, A J WELCH F44620-71-C-0091
UNCLASSIFIED TR-180 AFOSR-TR-77-0005 NL

3 OF 3
AD
A035057

END
DATE
FILMED
3-77

Rate Process Model

The model of Henriques (51) does not accurately describe the damage to retinal tissues. The coefficients derived for macular and paramacular areas are different from one another and are not the same as Henriques coefficients. The reason for these observed differences in damage temperatures have been discussed in a previous section. The major difference is probably due to the fact that the damage observed in this study is not the result of a simple, first order reaction. The damage observed is probably due to denaturation and coagulation of retinal proteins and tissue edema which results from damage to retinal cells and deactivation of enzyme systems which are important in the synthesis of retinal proteins. Of these, tissue edema is probably the major effect which causes the observed change in fundus reflectance.

The rate process model depends upon a knowledge or the ability to predict temperature at all positions in the tissue. The process by which the damage occurs must be known or modeled empirically from observations of damage by some arbitrary criterion. At best, because of experimental error and variations in criteria for damage only an average effect may be predicted. Especially, the apparent volume effect of damage rather than the damage at a point must be considered. The possibility that the tissue exhibits a minimum response to tissue damage which is a function of biological

amplification that may not correspond to the same criteria as for protein or enzyme changes must be considered. Errors in the estimation of damage may be significant if a minimum volume must be damaged in order to observe a lesion. If the system response (e.g. edema) is larger than the actual volume of damage, a rate process model based on temperature increase alone may not predict the observed lesion radius accurately.

The retinal damage produced by threshold exposures from .01 second to 10 seconds in this study can be predicted by a rate process model. (1) The temperature required to produce the effect which is the criterion for damage increases with decreasing exposure duration. (2) The radius of the visible lesion decreases with decreasing exposure time due to the reduced effect of conduction at shorter exposure durations. Even though the measurement of lesion radius and, therefore, the actual temperature at which damage occurs cannot be measured accurately by ophthalmoscope, the trends which imply that the damage observed is a thermal rate process are clearly demonstrated by this research.

CHAPTER VI

CONCLUSIONS

Temperature increases in the primate fundus (*Macaca mulatta*) for threshold lesion appearance 5 minutes post exposure to argon laser irradiation have been measured for exposure durations from .01 second to 10 seconds. Comparisons of measured and calculated temperature increases have been presented for three sets of model parameters in the computer solution of the heat conduction equation. The rate process model predictions of damage temperature have been compared with the measured lesion center and lesion radius temperature increases. Conclusions resulting from this research are as follows:

1. The measured image center temperature increases at the axial position of highest temperature rise is higher for paramacular exposures than for macular exposures. The mean and standard deviation of temperature increase for paramacular exposure durations of .01 second, .1 second, 1 second, and 10 seconds are 55.9 ± 14.9°C, 39.9 ± 5.1°C, 28.7 ± 3.0°C, and 24.8 ± 1.7°C, respectively. For macular exposures of .01 second, .1 second, 1 second, and 10 seconds duration, the average values and the standard deviations of the measured temperature increases are 66.1 ± 44.3°C, 29.4 ± 4.1°C,

24.1 ± 3.4°C and 19.9 ± 1.5°C respectively.

2. The damage temperatures at the ophthalmoscopically measured lesion radius are estimated to be .58, .75, .82 and .88 times the lesion center temperatures for macular and paramacular exposure durations of .01 second, .1 second, 1 second and 10 seconds respectively. The error in this measurement is lower for long duration exposures than for short duration exposures.

3. The temperature model predicts lesion center temperatures within 20% of the measured temperature increases for exposure durations from .1 second to 10 seconds for paramacular exposures and within 10% for macular exposures. The model with parameter set 3 is within 14% for paramacular exposures and 6% for macular exposures for exposure durations of .1 second to 10 seconds.

4. The damage to retinal tissues resulting from laser irradiation for exposure durations used in this research is the result of increased temperature in the retinal tissues. Exposure durations shorter than 10 seconds required a higher temperature increase to produce damage. Therefore, the damage to the tissue conforms to the definition of a rate process since

the damage is dependent upon both the temperature increase and the exposure duration.

5. A simple rate process for protein denaturation by Henriques does not predict the estimated damage temperature at the lesion radius found in this research. In the macula, the predicted damage temperatures are higher, while in the paramacular, the predicted temperatures are lower than the experimental values. This implies a volume difference for damage which results in an observable lesion with the damaged volume being larger in the paramacular region of the eye.

6. Both measured and modeled temperatures display a lower standard deviation than the corneal power standard deviation. This implies that the damage temperature is less sensitive to changes in image radius and the shape of the image distribution than corneal power over the limited range of image sizes and distribution in this research. Therefore, an accurate knowledge of image size and distribution of power in the image is necessary for comparison of corneal powers required to produce damage.

7. The difference in rise time between the model and the experiment shows a need for the accurate determination of the absorption parameters for the P.E. and choroid. For the model to accurately predict temperature-time histories and damage profile, the time constant as well as "end point" temperature must be accurately matched since the rate process model employs an exponential function.
8. From this research, it appears that a universal model (i.e., constant absorption coefficients) cannot be used tc accurately predict retinal temperature in the macular and paramacular regions of the eye. The differences in both the rise time of temperature and the final value which produce damage in the two areas imply that different coefficients and damage models are required for the prediction of fundus damage.
9. Further experiments are necessary to provide accurate predictions of temperature rise at the lesion radius and the extent damage in the retina which results from exposure to intense light sources. Some of the basic questions which require further investigation are:

(a) The reasons for differences in macular and paramacular threshold temperature increases must be determined. Histological and histochemical studies are needed to determine macular and paramacular differences at the ophthalmoscopic thresholds for a number of exposure durations. In vivo measurements of the absorption of light in the neural layers, pigment epithelium, and choroid are required as a function of wavelength and position in the fundus. Accurate determinations of the preretinal ocular media transmission and the absorption coefficients of the various layers of the fundus are necessary for the accurate prediction of temperature increase in these two areas of the eye.

(b) Determination of the effect of blood flow on the retinal temperature increase. Measurements of threshold temperatures with and without blood flow can be used to determine the influence of vascular perfusion on temperature rise time and the final temperature required to produce damage. Accurate estimates of blood flow rates and the effect of blood flow on model calculated temperature-time histories are also needed.

(c) The optical transfer function for the prediction of damage from minimal image sizes must be obtained. The model requires accurate determination of the point spread function of the eye and measurement of temperatures for minimal image lesions. Histological studies should also be used to determine the effect of image size on damage volume for an observable lesion.

(d) Determination of changes in functional vision as evidenced by reduced local electrical activity for threshold and sub-threshold lesions. Local potential measurements in the lesion from a combination thermocouple and potential measurement electrode could be used to investigate changes in the local potentials following laser irradiation.

(e) Determination of the effects of laser irradiation on choroidal and retinal vasculature. This study would be of clinical importance in the use of lasers for photocoagulation. Histological studies in the eye and studies on the microcirculation in a simpler system could be used to study the production of thromboses in vessels following laser exposure.

REFERENCES

1. Clarke, A.M., "Ocular Hazards from Lasers and Other Optical Sources", CRC Critical Reviews in Environmental Control, 307, November 1970.

2. Van Pelt, W.F., W.R. Payne, R.W. Peterson, "A Review of Selected Bioeffects Thresholds for Various Spectral Ranges of Lights", U.S. Department of Health, Education, and Welfare, Publication (FDA) 74-8010, 60 pp., June 1973.

3. Sliney, David H., "The Development of Laser Safety Criteria Biological Considerations", Laser Applications in Medicine and Biology, Vol. 1, ed., M.L. Wobarsht, Plenum Press, New York, 163, 1971.

4. Zaret, M.M., G.M. Breinin, H. Schnidt, H. Ripps, and I. Siegel, "Photo-Coagulation Produced by a Coherent Light Source", Department of Ophthalmology, New York University Medical Center, Rome Air Development Center, Technical Note 61-64, Griffiss Air Force Base, New York (AD 264393), 1961.

5. Ham, W.T., R.C. Williams, H.A. Mueller, R.S. Ruffin, F.H. Schmidt, A.M. Clarke, and W.J. Geeraets, "Effects of Laser Radiation on the Mammaliam Eye", New York Academy of Science, Section II, Vol. 28, No. 4, 517, 1966.

6. Vassiliadis, A., H.C. Zweng, N.A. Peppers, R.R. Peabody, and R.C. Hovey, "Threshold of Laser Eye Hazards", Archives of Environmental Health, Vol. 20, 161, 1970.

7. Geeraets, W.J., and E.R. Berry, "Ocular Spectral Characteristics as Related to Hazard from Lasers and Other Light Sources", American Journal of Ophthalmology, Vol. 65, 15, 1968.

8. Geeraets, W.J., R.C. Williams, C. Than, W.T. Ham, and F.H. Schmidt, "The Loss of Light Energy in the Retina and Choroid", Archives of Ophthalmology, Vol. 64, 606, 1960.

9. Boettner, E.A., and I.R. Walter, "Transmission of the Ocular Media", Investigative Ophthalmology, Vol. 1, 776, 1962.

10. Ludvigh, E. and E.F. McCarthy, "Absorption of Visible Light by the Refractive Media of the Human Eye", Archives of Ophthalmology, Vol. 20, 37, 1938.

11. Zweng, H.C., H.L. Little, and R.R. Peabody, Laser Photo-Coagulation and Retinal Angiography, C.V. Mosby Company, St. Louis, 1969.

12. Lappin, P.W., "Ocular Damage Thresholds for the Helium-Neon Laser", Archives of Environmental Health, Vol. 20, 177, 1970.

13. Bruce, Bob, Personal Communication.

14. Davis, T.P., and W.J. Mautner, "Helium-Neon Laser Effects on the Eye", Annual Report, Contract No. DADA 17-69-C-9013, U.S. Army Medical Research and Development Company, Washington, D.C., 1969.

15. Gibbons, W.D., Threshold Damage Evaluation of Long-Term Exposure to Argon Laser Radiation, U.S. Air Force Report SAM-TR-74-29, August 1974.

16. Born, M., and E. Wolf, Principles of Optics, Permagon Press, New York, 381-400, 1959.

17. Ward, B. and W.R. Bruce, "The Role of Body Temperature in the Definition of Retinal Burn Threshold", Investigative Ophthalmology, Vol. 10, No. 12, 955-958, 1971.

18. Polhamus, G.D., and A.J. Welch, "Effect of Pre-Exposure Fundus Temperature on Threshold Lesion Temperatures in the Laser Irradiated Rabbit Retina", Investigative Ophthalmology, Vol. 14, 562-565, 1975.

19. Geeraets, W.J., and D. Ridgeway, "Retinal Damage for High Intendity Light", Acta Ophthalmologica Supplementum 76, 109-112, 1973.

20. McNeer, K.W., M. Ghosh, W.J. Geeraets, and D. Guerry, "ERG After Light Coagulation", Acta Ophthalmologica Supplementum 76, 94, 1963.

21. Priebe, L.A. and A.J. Welch, "Changes in the Rabbit Electroretinogram C-Wave Following Ruby Laser Insult", Aerospace Medicine, Vol. 44, No. 11, 1246-1250, November 1973.

22. Hempel, F.G. and A.J. Welch, "Evoked Potentials from the Laser-Irradiated Retina", TR No. 83, Electronics Research Center, University of Texas at Austin, March 20, 1970.

23. Mautner, W.J., "Effects of Subthreshold Laser Irradiation on the Evoked Cortical Response in Rabbits", Second International Laser Safety Conference and Workshop, Cincinnati, Ohio, 1969.

24. Farrar, D.N., E.S. Graham, W.T. Ham, W.J. Geeraets, R.C. Williams, H.A. Mueller, S.F. Cleary, and A.M. Clarke, "The Effect of Threshold Macular Lesions and Subthreshold Macular Doses on Visual Activity in the Rhesus Monkey", American Industrial Hygeine Association Journal, Vol. 31, 198, 1970.

25. Geeraets, W.J., J. Burkhart, and D. Guerry III, "Enzyme Activity in the Coagulated Retina: A Means of Studying Thermal Conduction as a Function of Exposure Time", Acta Ophthalmologica Supplementum 76, 79, 1963.

26. Najac, H., B. Cooper, J.H. Jacobson, M.H. Shamos, and M. Breitfeller, "Direct Thermocouple Measurements of Temperature Rise and Heat Conduction in the Rabbit Retina", Investigative Ophthalmology, Vol. 2(No. 1), 32, 1963.

27. Mellerio, J., "The Thermal Nature of Retinal Laser Photo-Coagulation", Experimental Eye Research, Vol. 5, 242, 1966.

28. Kohtiao, A., I. Resnick, J. Newton, and H.A. Schwell, "Temperature Rise and Photocoagulation of Rabbit Retinas Exposed to the C.W. Laser", American Journal of Ophthalmology, Vol. 62, No. 3, 524, September 1966.

29. Campbell, C.J., D.K. Noyori, M.C. Rittler and C.J. Koester, "Intraocular Temperature Changes Produced by Laser Coagulation", Acta Ophthalmologica Supplementum 76, 22, 1963.

30. Noyori, K.S., C.J. Campbell, M.C. Rittler and C.J. Koester, "Ocular Thermal Effects Produced by Photocoagulation", Archives of Ophthalmology, Vol. 70, 817, 1963.

31. Crowder, J., "Measurement of the Vitreous Temperature During Photocoagulation in the Rabbit Eye", Acta Ophthalmologica Supplementum 76, 32, 1963.

32. Cain, C.P. and A.J. Welch, "Measured and Predicted Laser-Induced Temperature Rises in the Rabbit Fundus", Investigative Ophthalmology, Vol. 13, No. 1, 60-70, 1974.

33. Vos, J.J., "Heat Damage to the Retina by Lasers and Photocoagulation", Ophthalmologica, Vol. 151, 652, 1966.

34. Hansen, W.P., L. Feigen and S. Fine, "A Worst Case Analysis of Continuous Wave Ne-Ne Laser Hazards to the Eye", Applied Optics, Vol. 6, No. 11, 1973, 1967.

35. Clarke, A.M., W.J. Geeraets and W.T. Ham, "An Equilibrium Thermal Model for Retinal Injury for Optical Sources", Applied Optics, Vol. 8, No. 5, 1051, 1969.

36. Roulier, A., "Calculation of Temperature Increase in the Eye Produced by Intense Light", Bulletin of Mathematical Biophysics, Vol. 32, 403, 1970.

37. Felstead, E.B. and R.S. Cobbold, "Analog Solution of Laser Retinal Coagulation", Medical Electronics, Biological Engineering, Vol. 3, 145, 1965.

38. Vos, J.J., "Digital Computation of Temperatures in Retinal Burn Problems", Institute for Perception, RUD-TNO, Report No. IZE 1965-16, Soesterberg, The Netherlands.

39. Mainster, M.A., T.J. White, J.H. Tips, and P.W. Wilson, "Spectral Dependence of Retinal Damage Produced by Intense Light Sources", Journal of the Optical Society of America, Vol. 60, No. 6, 848, June 1970.

40. White, T.J., M.A. Mainster, J.H. Tips, and P.W. Wilson, "Chorioretinal Thermal Behavior", Bulletin of Mathematical Biophysics, Vol. 32, 315, 1970.

41. Mainster, M.A., T.J. White, J.H. Tips, and P.W. Wilson, "Transient Thermal Behavior in Biological Systems", Bulletin of Mathematical Biophysics, Vol. 32, 303, 1970.

42. Allen, R.G., W.R. Bruce, K.R. Kay, L.K. Morrison, R.A. Neish, C.A. Polaski, and R.A. Richards, "Research on Ocular Effects Produced by Thermal Radiation", Final Report AF41 (609)-3099, Brooks AFB, Texas, 1967. [AD 659 146, Clearinghouse, U.S. Department of Commerce, Springfield, Virginia].

43. Peacock, G.R., "Surface Temperature as a Parameter in Estimating Laser Injury Thresholds", Report No. 733, U.S. Army Medical Research Laboratory, Fort Knox, Kentucky, 1961.

44. Spells, K.E., "The Thermal Conductivities of Some Biological Fluids", Physics in Medicine and Biology, Vol. 5, 139-153, 1960.

45. White, T.J., Personal Communication, 1974.

46. Brooks Air Force Base, School of Aerospace Medicine, Laser Effects Laboratory, Values Given at Quarterly Report Meeting, September 1974.

47. Smith, W.J., Modern Optical Engineering, McGraw-Hill, New York, 1966.

48. Davson, H., The Eye, Vol. 1, Academic Press, New York, 1962.

49. Reed, R.P. "Thin Film Sensors of Micron Size and Applications in Biothermology", Ph.D. Dissertation, The University of Texas at Austin, 1966.

50. Carslaw, H.S. and J.C. Jaeger, Conduction of Heat in Solids, Oxford University Press, Ely House, London, 1959.

51. Henriques, F.C., "Studies of Thermal Injury", Archives of Pathology, Vol. 43, 489, 1947.

52. Fugitt, G.H., "A Rate Process Theory of Thermal Injury", AFSWP 606, U.S. Army Special Weapons Project, Washington, D.C., 1955.

53. Stoll, Alice A., "A Computer Solution for Determination of Thermal Tissue Damage Integrals from Experimental Data," IRE Transactions on Medical Electronics, Vol. ME-7, 355, October 1960.

54. Weaver, John A., and Alice M. Stoll, "Mathematics Model of Skin Exposed to Thermal Radiation", Aerospace Medicine, Vol. 40, No. 1, 24, January 1969.

55. Stoll, A.M., and M.S. Chianta, "Burn Production and Prevention in Convective and Radiant Heat Transfer", Aerospace Medicine, Vol. 39, No. 10, 1097, October 1968.

56. Hu, Chia-Lun and F.S. Barnes, "The Thermal-Chemical Damage in Biological Material Under Laser Irradiation", IEEE Transactions on Bio-Medical Engineering, Vol. BME-17, No. 3, 220, July 1970.

57. Kach, E.A., and F.P. Incropera, "Induction Thermocoagulation: Thermal Response and Lesion Size", IEEE Transactions on Bio-Medical Engineering, Vol. BME-21, No. 1, 8, January 1974.

58. Vassiliadis, A., "Ocular Damage from Laser Radiation", Laser Applications in Medicine and Biology, Vol. 1, M.L. Wolbarsht, ed., Plenum Press, New York, 125, 1971.

59. Wood, T.H., "Lethal Effects of High and Low Temperature on Unicellular Organisms", Advances in Biological Medical Physics, Vol. 4, Academic Press, 119, 1956.

60. Priebe, L.A., C.P. Cain, and A.J. Welch, "Temperature Rise Required for Production of Minimal Lesions in the Macaca Mulatta Retina", American Journal of Ophthalmology, Vol. 79, No. 3, 405-413, 1975.

61. Martins, W.D., and E.A. Ripperger, "The Development of a Probe-Type Thin Film Microthermocouple for Biomedical Use", TR 120 Electronics Research Center, The University of Texas at Austin, 1972.

62. Cain, C.P. and A.J. Welch, "Thin Film Temperature Sensors for Biological Measurements", IEEE Transactions on Biomedical Engineering, Vol. 21, No. 4, 421-423, 1974.

63. Wolbarsht, M.L. and D.H. Sliney, "The Formulation of Protection Standa-rds for Lasers", Laser Applications in Medicine and Biology, Volume 2, 309-355, M.L. Wolbarsht, ed., Plenum Press, New York, 1974.

64. Kreith, F., Principles of Heat Transfer, Intext Educational Publishers, New York, 1973.

65. Blackwell, J.H., "Radial-Axial Heat Flow in Regions Bounded Internally by Circular Cylinders", Canadian Journal of Physics, Vol. 31, 472-479, 1953.

66. Blackwell, J.H. "The Axial-Flow Error in the Thermal Conductivity Probe", Canadian Journal of Physics, Vol. 34, 412-417, 1956.

67. Campbell, C.J., M.E. Rittler, K.S. Noyori, C.H. Swope, and C.J. Koester, "The Threshold of the Retina to Damage by Laser Energy", Archives of Ophthalmology Supplementum 76, 437, 1966.

68. Brindley, G.S., and E.N. Willmer, "The Reflection of Light from the Macular and Peripheral Fundus Oculi in Man", Journal of Physiology, Vol. 116, 350-356, 1952.

69. Wallow, I.H.L., and M.O.M. Tso, "Repair After Xenon Arc Photocoagulations", American Journal of Ophthalmology, Vol. 75, No. 4, 610-626, 1973.

70. Tso, M.O.M., I.H.L. Wallow and J.O. Powell, "Differential Susceptibility of Rod and Cone Cells to Argon Laser", Archives of Ophthalmology, Vol. 89, 228-233, March 1973.

71. Wallow, I.H.L., M.O.M. Tso, and B.S. Fine, "Retinal Repair After Experimental Xenon Arc Photocoagulation", American Journal of Ophthalmology, Vol. 75, No. 1, 1973.

72. Hayes, J.R. and M.L. Wobarsht, "Thermal Model for Retinal Damage Induced by Pulsed Lasers", Aerospace Medicine Vol. 39, 474-480, May 1968.

73. Bebie, H., F. Fankhauser, W. Lotmar and A. Roulier, "Theoretical Estimate of the Temperature Within Irradiated Retinal Vessels", Acta Ophthalmologica, Vol. 52, 13-36, 1974.

DISTRIBUTION LIST*

Current AFOSR Contract F44620-71-C-0091

Joint Services Electronics Program Distribution List Dated 30 March 1976

DEPARTMENT OF DEFENSE

Defense Documentation Center
ATTN: DDC-TCA (Mrs. V. Caponio)
Cameron Station
Alexandria, Virginia 22314

Asst. Dir, Electronics & Computer Sciences
Office of Director of Defense Research and Engineering
The Pentagon
Washington, DC 20315

Office of the Director of Defense
Research and Engineering
Information Office Library Branch
The Pentagon
Washington, DC 20301

ODDR&E Advisory Group on Electron Devices
201 Varick Street
New York, New York 10014

Chief, R & D Division (340)
Defense Communications Agency
Washington, DC 20301

Director, National Security Agency
Fort George G. Meade, Maryland 20755
ATTN: Dr. T. J. Beahn

Institute for Defense Analysis
Science and Technology Division
400 Army-Navy Drive
Arlington, Virginia 22202

Dr. Stickley
Defense Advanced Research Projects Agency
ATTN: Technical Library
1400 Wilson Boulevard
Arlington, Virginia 22209

Dr. R. Reynolds
Defense Advanced Research Projects Agency
ATTN: Technical Library
1400 Wilson Boulevard
Arlington, Virginia 22209

DEPARTMENT OF THE AIR FORCE

AF/RDPS
The Pentagon
Washington, DC 20330

AFSC (LI/Mr. Irving R. Mirman)
Andrews AFB
Washington, DC 20334

Directorate of Electronics and Weapons
HQ AFSC/DLC
Andrews AFB, Maryland 20334

Directorate of Science
HQ AFSC/DLS
Andrews AFB
Washington, DC 20334

LTC J. W. Gregory
AF Member, TAC
Air Force Office of Scientific Research
Bolling AFB
Washington, DC 20332

Mr. Carl Slotten
AFCRL/LZ
Hanscom AFB, MA 01731

Dr. Richard Picard
AFCRL/OPL
Hanscom AFB, MA 01731

Mr. Robert Barrett
AFCRL/LO
Hanscom AFB, MA 01731

Dr. John N. Howard
AFCRL (CA)
Hanscom AFB, MA 01731

Dr. Richard B. Mack
AFCRL/LZR
Hanscom AFB, MA 01731

Documents Library (TILD)
Rome Air Development Center
Griffiss AFB, New York 13441

Mr. H. E. Webb, Jr. (EMCP)
Rome Air Development Center
Griffiss AFB, New York 13441

Mr. Murray Kesselman (EMCN)
Rome Air Development Center
Griffiss AFB, New York 13441

Mr. W. Edwards
AFAL/TE
Wright-Patterson AFB, Ohio 45433

Mr. R. D. Larson
AFAL/DHR
Wright-Patterson AFB, Ohio 45433

Howard H. Steenbergen
AFAL/DHE
Wright-Patterson AFB, Ohio 45433

Chief Scientist
AFAL/CA
Wright-Patterson AFB, Ohio 45433

HQ ESD (DRI/Emp 22)
Hanscom AFB, MA 01731

Professor R. E. Fontana
Head, Dept. of Electrical Engineering
AFIT/ENE
Wright-Patterson AFB, Ohio 45433

Mr. John Mottsmith (MCET)
HQ ESD (AFSC)
Hanscom AFB, MA 01731

LTC Richard J. Gowen
Professor
Dept. of Electrical Engineering
USAF Academy, Colorado 80840

AUL/LSE-9063
Maxwell AFB, Alabama 36112

AFETR Technical Library
P. O. Box 4008, MU 8650
Patrick AFB, Florida 32542

ADTC (DLOSL)
Eglin AFB, Florida 32542

HQ AMD (RDA/Col. Godden)
Brooks AFB, Texas 78235

USAF European Office of Aerospace Research
Technical Information Office
Box 14, FPO, New York 09510

Dr. Carl E. Baum
AFWL (ES)
Kirtland AFB, New Mexico 87117

AGAFSAM/RAL
Brooks AFB, Texas 78235

DEPARTMENT OF THE ARMY

HQDA (DAMA-ARZ-A)
Washington, DC 20310

Commander
US Army Security Agency
ATTN: IARD-T
Arlington Hall Station
Arlington, VA 22212

Commander
US Army Materiel Development and
Readiness Command
ATTN: Technical Library Rm 7S 35
5001 Eisenhower Avenue
Alexandria, VA 22333

Commander
US Army Ballistics Research Laboratory
ATTN: DRXBR-BAD
Aberdeen Proving Ground
Aberdeen, MD 21005

Commander
Picatinny Arsenal
ATTN: SMUPA-TS-T-S
Dover, NJ 07801

US Army Research Office
ATTN: Dr. Hermann Robl
P. O. Box 12211
Research Triangle Park, NC 27709

US Army Research Office
ATTN: Mr. Richard O. Ulsh
P. O. Box 12211
Research Triangle Park, NC 27709

US Army Research Office
ATTN: Dr. Jimmie R. Suttle
P. O. Box 12211
Research Triangle Park, NJ 27709

US Army Research Office
ATTN: Dr. Horst Wittmann
P. O. Box 12211
Research Triangle Park, NC 27709

Commander
Frankford Arsenal
ATTN: Mr. George C. White, Jr.
Deputy Director, Pitman-Dunn Laboratory
Philadelphia, PA 19137

Commander
US Army Missile Command
ATTN: Chief, Document Section
Redstone Arsenal, AL 35809

Commander
US Army Materials and Mechanics
Research Center
ATTN: Chief, Materials Sciences Division
Watertown, MA 02172

Commander
Harry Diamond Laboratories
ATTN: Mr. John E. Rosenberg
2800 Powder Mill Road
Adelphi, MD 20783

Commandant
US Army Air Defense School
ATTN: ATSAD-T-CSM
Fort Bliss, TX 79916

Commandant
US Army Command and General Staff College
ATTN: Acquisitions, Lib Div
Fort Leavenworth, Kansas 66027

Dr. Hans K. Ziegler
Army Member, TAC/JSEP
US Army Electronics Command
(DRSEL-TL-D)
Fort Monmouth, NJ 07703

Mr. J. E. Tetl
Executive Secretary, TAC/JSEP
US Army Electronics Command
(DRSEL-TL-DT)
Fort Monmouth, NJ 07703

Director
Night Vision Laboratory, ECOM
ATTN: DRSEL-NV-D
Fort Belvoir, VA 22060

Commander/Director
Atmospheric Sciences Laboratory (ECOM)
ATTN: DRSEL-BL-DD
White Sands Missile Range, NM 88002

Director
Electronic Warfare Laboratory (ECOM)
ATTN: DRSEL-WL-MY
White Sands Missile Range, NM 88002

Commander
US Army Armament Command
ATTN: DRSAR-RD
Rock Island, IL 61201

Director, Division of Neuropsychiatry
Walter Reed Army Institute of Research
Washington, DC 20012

Commander
USASATCOM
Fort Monmouth, NJ 07703

*The Joint Services Technical Advisory Committee has established this list for the regular distribution of reports on the electronics research program of The University of Texas at Austin. Additional addresses may be included upon written request to:

Mr. J. E. Tetl (DRSEL-TL-DT)
Executive Secretary, TAC/JSEP
US Army Electronics Command
Fort Monmouth, New Jersey 07703

An appropriate endorsement by a Department of Defense sponsor is required, except on a request from a federal agency.

Commander
US Army R&D Group (Far East)
APO San Francisco, CA 96343

Commander
US Army Communications Command
ATTN: Director, Advanced Concepts Office
Fort Huachuca, AZ 85613

Project Manager
ARTADS
EAI Building
West Long Branch, NJ 07764

Commander
US Army White Sands Missile Range
ATTN: STEWS-ID-R
White Sands Missile Range, NM 88002

Director, TRI-TAC
ATTN: TT-AD (Mrs. Briller)
Fort Monmouth, NJ 07703

Commander
US Army Communication Command
ATTN: CC-OPS-PD
Fort Huachuca, AZ 85613

COL Robert Noce
Senior Standardization Representative
US Army Standardization Group, Canada
Canadian Force Headquarters
Ottawa, Ontario, Canada K1A 0K2

Commander
US Army Electronics Command
ATTN: DRSEL-RD-O (Dr. W. S. McAfee)
CT-L (Dr. R. Buser)
NL-O (Dr. H. S. Bennett)
TL-S (M. R. Kalinski)
VL-D
WL-D
TL-MM (M. N. Lipetz)
NL-H (Dr. F. Schwering)
TL-E (Dr. S. Kronenberg)
TL-E (Dr. J. Kohn)
TL-I (Dr. C. Thornton)
NL-S (Dr. S. Amoroso)
Fort Monmouth, NJ 07703

Project Manager
Ballistic Missile Defense Program Office
ATTN: DACS-BMP (Mr. A. Gold)
1300 Wilson Blvd.
Washington, DC 22209

DEPARTMENT OF THE NAVY

Office of Naval Research
Electronic and Solid State Sciences Program (Code 427)
800 N. Quincy
Arlington, Virginia 22217

Office of Naval Research
Code 200
Assistant Chief for Technology
800 N. Quincy
Arlington, Virginia 22217

Office of Naval Research
Information Sciences Program (Code 437)
800 N. Quincy
Arlington, Virginia 22217

Naval Research Laboratory
4555 Overlook Avenue, S. W.
Washington, DC 20375
ATTN: Codes 2627
4000
4105
5000
5200
5203
5210
5270
5300
5400
5460
5464
5500
5510
6400

Director Office of Naval Research Branch Office
536 South Clark Street
Chicago, Illinois 60605

San Francisco Area Office
Office of Naval Research
760 Market Street, Room 447
San Francisco, California 94102

Dr. A. Laufer
Chief Scientist
Office of Naval Research Branch Office
1030 East Green Street
Pasadena, California 91101

Director
Office of Naval Research Branch Office
715 Broadway, 5th Floor
New York, New York 10003

Mr. L. W. Sumney
Naval Electronics Systems Command
NC 01
2511 Jefferson Davis Highway
Arlington, Virginia 20360

Mr. R. Frettle
Naval Electronics Systems Command
NC 01
2511 Jefferson Davis Highway
Arlington, Virginia 20360

Mr. N. Butler
Naval Electronics Systems Command
NC 01
2511 Jefferson Davis Highway
Arlington, Virginia 20360

Dr. H. J. Mueller
Naval Air Systems Command
JP 01
1411 Jefferson Davis Highway
Arlington, Virginia 20360

U. S. Naval Oceanographic Office
Library L Code 1600
Washington, DC 20373

Commandant, Marine Corps
Scientific Advisor (Code AX)
Washington, DC 20380

Dr. Gernot M. R. Winkler
Director, Time Service
U. S. Naval Observatory
Massachusetts Avenue at 34th Street, N. W.
Washington, DC 20390

Naval Postgraduate School
Technical Library
Monterey, California 93940

Naval Electronics Laboratory Center
Technical Library
San Diego, California 92152

Naval Electronics Laboratory Center
ATTN: Code 2600
San Diego, California 92152

Naval Electronics Laboratory Center
San Diego, California 92152
ATTN: Codes 2000
2200
2300
3000
3200
3300
4000
5000
5300
5300

Naval Undersea Center
Technical Library
San Diego, California 92152

Naval Ship Research and Development Center
David W. Taylor
Code 522.1
Bethesda, Maryland 20084

Office of Chief of Naval Operations
NAICOM/MIS Planning Branch
NOP-916D, Pentagon
Washington, DC 20350

New York Area Office
Office of Naval Research
715 Broadway, 5th Floor
New York, New York 10003

Capt. R. B. Meeks
Naval Sea Systems Command
NC 03
2531 Jefferson Davis Highway
Arlington, Virginia 20362

Commander
Naval Surface Weapons Center
ATTN: Technical Library
Silver Spring, Maryland 29010

Naval Surface Weapons Center
ATTN: Code 212
Silver Spring, Maryland 29010

Officer-in-Charge
Naval Surface Weapons Center
Dahlgren Laboratory
Dahlgren, Virginia 22448

Naval Air Development Center
ATTN: Technical Library
Johnsville
Warminster, Penn. 18974

Commander
Naval Avionics Facility
Indianapolis, Indiana 46241
ATTN: D/035 Technical Library

Naval Missile Center
Technical Library
Code 0632.2
Point Mugu, California 93042

Naval Weapons Center
ATTN: Technical Library, Code 533
China Lake, California 93555

Naval Weapons Center
ATTN: Code 6010
China Lake, California 93555

Naval Weapons Center
Mathematics Division
China Lake, California 93555

Naval Training Equipment Center
Technical Library
Orlando, Florida 32813

Naval Research Laboratory
Underwater Sound Reference Division
Technical Library
P. O. Box 8337
Orlando, Florida 32806

Naval Underwater Sound Center
Technical Library
New London, Conn. 06320

OTHER GOVERNMENT AGENCIES

Mr. F. C. Schwenk, RD-T
National Aeronautics & Space Administration
Washington, DC 20546

Los Alamos Scientific Laboratory
ATTN: Reports Library
P. O. Box 1663
Los Alamos, New Mexico 87544

M. Zane Thornton, Deputy Director
Institute for Computer Sciences & Technology
National Bureau of Standards
Washington, DC 20234

Director, Office of Postal Technology (R&D)
US Postal Service
11711 Parklawn Drive
Rockville, Maryland 20852

NASA Lewis Research Center
ATTN: Library
21000 Brookpark Road
Cleveland, Ohio 44135

Library - R31
Bureau of Standards
Acquisition
Boulder, Colorado 80302

MIT Lincoln Laboratory
ATTN: Library A-082
P. O. Box 73
Lexington, Massachusetts 02173

Dr. Jay Harris
Program Director, Devices and Waves Program
NSF
1800 G Street
Washington, DC 20550

Dr. Howard W. Blanl
Deputy Director, Div of Materials Rech
NSF 1800 G Street
Washington, DC 20550

Dr. Dean Mitchell
Program Director, Solid-State Physics
Division of Materials Research
National Science Foundation
1800 G Street
Washington, DC 20550

NON-GOVERNMENT AGENCIES

Director
Research Laboratory of Electronics
Massachusetts Institute of Technology
Cambridge, Massachusetts 02139

Director
Microwave Research Institute
Polytechnic Institute of New York
Long Island Graduate Center, Route 110
Farmingdale, New York 11735

Asst. Dir, Microwave Research Institute
Polytechnic Institute of New York
333 Jay Street
Brooklyn, New York 11201

Director
Columbia Radiation Laboratory
Dept of Physics
Columbia University
538 West 120th Street
New York, New York 10027

Director
Coordinated Science Laboratory
University of Illinois
Urbana, Illinois 61801

Director
Stanford Electronics Laboratory
Stanford University
Stanford, California 94305

Director
Microwave Laboratory
Stanford University
Stanford, California 94305

Director
Electronics Research Laboratory
University of California
Berkeley, California 94720

Director
Electronics Sciences Laboratory
University of Southern California
Los Angeles, California 90007

Director
Electronics Research Center
The University of Texas at Austin
Engineering-Science Bldg 112
Austin, Texas 78712

Director of Laboratories
Division of Engineering & Applied Physics
Harvard University
Pierce Hall
Cambridge, Massachusetts 02138